

Temporal Processing by *Caenorhabditis elegans* Sensory  
Neurons

Saul Kato

Submitted in partial fulfillment of the  
requirements for the degree of  
Doctor of Philosophy  
under the Executive Committee  
of the Graduate School of Arts and Sciences

COLUMBIA UNIVERSITY

2013

© 2013

Saul Kato

All rights reserved

## ABSTRACT

Temporal Processing by *Caenorhabditis elegans* Sensory Neurons

Saul Kato

*Caenorhabditis elegans* is a promising organism for trying to understand how nervous systems generate real-time behavior. Its low neuron count suggests that we may be able to observe all of the constituents of the computation of sophisticated sensorimotor behavior. However, its appropriateness as a system for quantitative dynamical study has yet to be established. We show that *C. elegans* chemosensory neurons can operate in a highly deterministic and low-noise mode, and they act as reliable linear filters of their input. We then use dynamical systems analysis in combination with classical genetic perturbation to uncover cellular and circuit mechanisms of temporal processing. This work should firmly establish *C. elegans* as a viable platform for applying quantitative dynamical systems methods to understanding how a nervous system processes sensory information, integrates it with an evolving internal state, and produces goal-directed, coordinated behavior.

# Contents

<b>Acknowledgements</b>	<b>vii</b>
<b>Dedication</b>	<b>ix</b>
<b>1 Introduction</b>	<b>1</b>
1.1 Goals . . . . .	1
1.2 <i>C. elegans</i> as a model organism for neuroscience . . . . .	3
1.2.1 <i>C. elegans</i> practicalities . . . . .	3
1.2.2 <i>C. elegans</i> nervous system . . . . .	4
Chemosensation . . . . .	5
The AWC neuron . . . . .	6
The ASH neuron . . . . .	7
1.2.3 Worm behavior . . . . .	7
Undirected chemotaxis . . . . .	8
Directed chemotaxis . . . . .	9
Escape . . . . .	10
1.3 Dynamical Systems Modeling . . . . .	10
1.3.1 Definitions and Basic Properties . . . . .	11
1.3.2 Integral Models . . . . .	14
Linear Time-Invariant Models . . . . .	15
Nonlinear Time-Invariant Models: Wiener/Volterra Expansion . . . . .	17

	Nonlinear Time-Invariant Models: L-N Cascade . . . . .	17
	More complex cascade models . . . . .	18
1.3.3	Differential Models . . . . .	20
	Linear ODEs . . . . .	22
	First-order stable linear system (1FF) . . . . .	24
	Second-order linear systems . . . . .	24
	Second-order feedback (2FB) . . . . .	28
	Third-order linear systems and higher . . . . .	29
	Nonlinear ODEs . . . . .	30
1.3.4	Estimation of Integral Models . . . . .	30
	Model Performance Evaluation . . . . .	30
	Linear models . . . . .	31
	Wiener-Volterra models . . . . .	33
	L-N models . . . . .	33
1.3.5	Estimation of Differential Models . . . . .	34
1.3.6	Differential versus Integral Models . . . . .	35
<b>2</b>	<b>Fourier Analysis of Responses in AWC for Circuit Dissection</b>	<b>38</b>
2.1	Summary . . . . .	38
2.2	The neuropeptide gene <i>nlp-1</i> limits local search behavior . . . . .	39
2.3	NLP-1 acts through the G protein-coupled receptor NPR-11 . . . . .	40
2.4	AWC inhibits AIA interneurons through glutamate and NLP-1 . . . . .	42
2.5	AWC responses are modulated by NLP-1 . . . . .	45
2.6	<i>nlp-1</i> mutants are defective in AWC odor adaptation . . . . .	47
2.7	INS-1 is a candidate feedback signal from AIA . . . . .	49
2.8	Discussion . . . . .	51
2.9	Experimental Methods . . . . .	54
2.9.1	Calcium imaging . . . . .	54

2.9.2	Local search behavior . . . . .	55
2.9.3	Adaptation assays . . . . .	55
2.9.4	Discrete Fourier transform . . . . .	55
2.9.5	Cell culture and calcium imaging . . . . .	58
2.9.6	Laser ablations . . . . .	59
2.9.7	Molecular biology and transgenesis . . . . .	59
2.10	Supplementary Figures . . . . .	59
<b>3</b>	<b>Integral and Differential Modeling of AWC and ASH</b>	<b>64</b>
3.1	Summary . . . . .	64
3.2	Introduction . . . . .	65
3.3	Reliable responses to rapid stimulus fluctuations . . . . .	67
3.4	Linear temporal filters describing AWC and ASH sensory neurons . . . . .	70
3.5	An ODE model for sensory filters . . . . .	75
3.6	The static nonlinearity matches properties of GCaMP3 . . . . .	77
3.7	L-N models accurately predict neuronal responses . . . . .	77
3.8	The ODE models predict many features of AWC and ASH responses . . . . .	80
3.9	A calcium channel mutant provides mechanistic insight into the biphasic model	81
3.10	A general model for sensory neuron dynamics . . . . .	82
3.11	Discussion . . . . .	84
3.11.1	Properties of individual sensory neurons are matched to behaviors . . . . .	85
3.11.2	Monitoring fast neuronal signals with genetically-encoded indicators . . . . .	86
3.11.3	Signaling mutants affect specific features of the model . . . . .	87
3.12	Experimental Procedures . . . . .	90
3.12.1	Calcium Imaging . . . . .	90
3.12.2	Stimulus Delivery . . . . .	90
3.12.3	Analysis of Cell Activation . . . . .	91
3.12.4	Trace Pre-Processing and Bleach Correction . . . . .	92

3.12.5	Linear-Nonlinear Model Estimation . . . . .	93
3.12.6	Dynamical Model Estimation and Correction for GCaMP Response Dynamics . . . . .	93
3.12.7	Worm Cultivation and Strains . . . . .	94
3.13	Supplementary Figures . . . . .	95
<b>4</b>	<b>Conclusion</b>	<b>102</b>
4.1	Future work: locating and modeling sensory integration . . . . .	102
4.2	Future work: inference of nonlinear differential models . . . . .	103
4.3	What might a total circuit model look like? . . . . .	105
4.4	Final thoughts . . . . .	107
	<b>Bibliography</b>	<b>107</b>
	<b>Appendix: L-N Estimation Flowchart</b>	<b>117</b>

# List of Figures

1.1	Signal transduction cascade in AWC sensory cilia . . . . .	7
1.2	Signal transduction in ASH sensory cilia . . . . .	8
1.3	A system. . . . .	11
1.4	L-N model . . . . .	18
1.5	Two equivalent serial L-N cascades . . . . .	19
1.6	Parallel L-N cascade. . . . .	20
1.7	First-order ODE system . . . . .	24
1.8	Filter of a first-order system . . . . .	25
1.9	Second order feed-forward system . . . . .	25
1.10	Envelopes of a difference of exponentials. . . . .	26
1.11	The relationship of time constants producing a particular filter peak time . . . . .	27
1.12	How a 2FF filter changes as we vary one time constant . . . . .	28
1.13	Second-order feedback ODE model. . . . .	29
1.14	Filters of underdamped second-order systems . . . . .	29
1.15	Our approach to differential model identification . . . . .	35
2.1	AWC releases NLP-1, which acts on NPR-11 in AIA . . . . .	41
2.2	Calcium responses in AIA interneurons require AWC glutamate and NLP-1 . . . . .	44
2.3	Altered AWC calcium responses in <i>nlp-1</i> and <i>npr-11</i> mutants . . . . .	46
2.4	Worms with mutations in <i>nlp-1</i> and <i>npr-11</i> are defective in olfactory adaptation. . . . .	48
2.5	<i>ins-1</i> is a component of the <i>nlp-1-npr-11</i> pathway. . . . .	50

2.6	AWC calcium responses . . . . .	60
2.7	AWC calcium responses in neurotransmitter mutants . . . . .	61
2.8	Adaptation defects in neuropeptide mutants . . . . .	62
2.9	<i>ins-1</i> mutant AWC responses and band-limited signal reconstructions . . . .	63
3.1	AWC and ASH track flickering odor stimuli. . . . .	69
3.2	AWC and ASH respond reliably to complex odor patterns . . . . .	71
3.3	Linear filters capture the dynamics of AWC and ASH responses . . . . .	73
3.4	A three-variable ODE model produces a biphasic filter with two timescales .	76
3.5	Performance and prediction of the L-N models. . . . .	79
3.6	Filter analysis reveals a role for <i>egl-19</i> in ASH and generality of biphasic model	83
3.7	Precise control of stimulus delivery . . . . .	96
3.8	The static nonlinearity of AWC and ASH responses approximates the nonlin- earity of GCaMP3 . . . . .	97
3.9	Robustness of ASH wild type filters to concentration and m-sequence struc- ture, and effects of signal transduction mutants. . . . .	98
3.10	ASH signal transduction mutant responses to 10 s glycerol pulses . . . . .	99
3.11	A biphasic filter with distinct phase widths underlies a general response of sensory neurons . . . . .	100
3.12	Response features of biphasic filters are determined by the balance of phase area and phase width . . . . .	101
4.1	A wild guess at a general architecture for worm behavior . . . . .	106
4.2	Flowchart for iterative L-N estimation . . . . .	118

# Acknowledgements

I thank my co-advisors Larry Abbott and Cori Bargmann for countless hours and patience in mentoring me, teaching me how to do science, and as indispensable collaborators. I thank my collaborators Yifan Xu and Christine Cho for countless hours, commitment, and incredible thoughtfulness given to this project. I thank the other members of my thesis committee, Liam Paninski, Stefano Fusi, and Shawn Lockery for being so accommodating and for providing valuable research advice and critical thinking about this work. I thank Ken Miller, Larry, and Stefano for career advice and valuable perspective. Without Ken, this collaboration would not have been born. I thank Carol Mason and Darcy Kelley, along with Ken, for being fabulous, kind, supportive, and no-nonsense program directors. I thank the members of the Theory Center for many morsels of mathematical wisdom, collegial warmth, a willingness for heady, if procrastinatory, debates, and the members of the Bargmann Lab who have taught me both remedial and cutting-edge molecular biology without any condescension and kept me generally in line, and to both groups for a willingness to help with just about anything. I thank my parents Hiroki and Joan for enthusiastic support in all of my endeavors, fostering in me a love of exploration and creation, and showing me the pleasure and importance of looking at things critically and the satisfaction of completion. I thank my brother Isaac for being a role model, protector, and showing me many of the cool things in life. Finally, I thank my wife Mariana and son Noam for moral support, counsel, sanity maintenance, and good cheer.

## Chapter 3 Acknowledgements

We thank the *C. elegans* knockout consortium and the Caenorhabditis Genetic Center (CGC) for strains, Y.H. Wang for the  $\alpha 16Z$  chimera, L. Looger for GCaMP2.2b, Y. Iino for discussions about *ins-1*, and L. Vosshall, G. Lee, E. Feinberg, M. Tsunozaki, J. Gray, J. Garrison, P. McGrath and members of the Bargmann laboratory for critical help, advice and insights. Peptide synthesis was performed by the Proteomics Resource Center of the Rockefeller University. This work was funded by the Mathers Foundation and by the Howard Hughes Medical Institute (C.I.B.). D.R.A. holds a Career Award at the Scientific Interface from the Burroughs Wellcome Fund.

## Chapter 4 Acknowledgements

We thank L. Looger for GCaMP3.0, M. Zimmer and H. Jang for sharing imaging data, and B. Bamber, C. Niell, G. Wayne, M. Vidne, D. Rubin, and P. McGrath for their insights and their comments on the manuscript.

This work was supported by the Gatsby, Swartz, and Kavli Foundations (L.F.A.), and the Howard Hughes Medical Institute (C.I.B.). S.K. was supported by NIH training grant T32NS064929 and NIMH grant R01MH93338, which also provided support for L.F.A. C.C. was supported by the Department of Defense (DoD) through the National Defense Science & Engineering Graduate Fellowship (NDSEG) Program, and Y.X. was supported by MSTP grant GM07739 and a Paul and Daisy Soros Fellowship.

This thesis is dedicated to Mr. Horton, Dr. Ngoi, and Mr. Benson, who have inspired and taught many.

# Chapter 1

## Introduction

### 1.1 Goals

How does an organism produce real-time behavior as a function of ongoing streams of stimuli and an evolving internal state? This on-line, or dynamic, computation, is circumscribed by time and space constraints, in stark contrast to the abstract computation defined by Alan Turing and his contemporaries.<sup>1</sup> The study of unicellular bacterial chemotaxis has yielded an exquisite understanding of what bacteria compute<sup>2</sup> and the mechanism by which they compute it (Barkai and Leibler, 1997; Yi et al., 2000) and has provided a solid footing for quantitative exploration of the principles shaping these functions over generational and evolutionary timescales (Clark and Grant, 2005; Celani and Vergassola, 2010). The emergence of nervous systems, our objects of study here, endowed multi-cellular organisms with the ability to perform more complex dynamic computations; at the least, they enabled the integration of more sensory variables and the flexible control of a physical plant with many more degrees of freedom, and their further evolution led to all of our cherished cognitive abilities.

---

<sup>1</sup>The latter definition, privy to infinitudes, surely defines a larger set of possible computations than the former, as surely as our human brains are descended from nervous systems honed over the millennia to perform the former kind of computation. How did a space-time limited, quick-and-dirty brain acquire the Platonic ability to imagine and reason about the theory of computation, much less perform abstract computations like simple arithmetic at will? We will set aside this conundrum.

<sup>2</sup>Among other things, they compute a *chemotactic response function* (Segall et al., 1986).

Among the animals commonly studied by neuroscientists, *C. elegans* sits at the low end of the scale of numerical complexity with precisely 302 neurons in the predominant hermaphroditic form. Taking the approach of starting with “easy” exercises before working up to the difficult ones, we choose *C. elegans* to try to understand what and how a nervous system, as a whole, computes. We follow a reductionist approach to studying a system by starting with an investigation of its constituents and their interactions. While much is known about the molecules and specific connectivity of the worm’s nervous system, the *dynamics* – their behavior in time – of the neurons and their connections (synapses, gap junctions, and diffuse messengers<sup>3</sup>) are relatively uncharacterized. Without a description of these dynamics and how they are affected by interaction with other components, any model or simulation of the nervous system is fatally unconstrained. Trying to understand how and what a neural circuit does from a connectivity map without dynamics is akin to trying to deduce the function of an electrical circuit by covering up the identities of each circuit element and looking at only the wires.

Calcium imaging by wide-field optical microscopy of neurons expressing fluorescent calcium sensors has become the predominant method for monitoring the activity of single *C. elegans* neurons, and work by several groups is underway to extend the calcium imaging methodology to image the activity of multiple neurons simultaneously. The process of calcium measurement by a fluorescent sensor imparts its own signal transformation on the system we seek to measure – an observer effect – and must be accounted for if we are to use calcium imaging to say something about the dynamics of the neurons themselves.

This thesis represents the beginning of an effort to map out the dynamics of the *C. elegans* nervous system, starting at the sensory neurons that receive input from the outside world. The goal of this work is to:

1. Establish *C. elegans* as a viable model organism for applying quantitative dynamical systems methods, in particular, to calcium imaging data.

---

<sup>3</sup>And while we’re at it, let’s not forget the action-perception loop (Sperry, 1962) as another “neuronal connection” from the motor neurons back to the sensory neurons.

2. Characterize the dynamics of *C. elegans* sensory neurons under the influence of various time-varying stimuli.
3. Combine dynamical systems analysis with genetic methods to uncover mechanisms of temporal processing.

## 1.2 *C. elegans* as a model organism for neuroscience

### 1.2.1 *C. elegans* practicalities

The one millimeter long free-living nematode *Caenorhabditis elegans* (the “worm”) was the first organism to have its cell lineage fully mapped (Sulston et al., 1983), its connectome fully mapped by electron microscopy (White et al., 1986), its genome fully sequenced (Consortium, 1998), and it continues to be a wonderfully fertile sandbox and proving ground for genetically engineered probes and perturbative constructs. It is easily maintained on an agar surface in a petri dish or in liquid, it has a 3.5 day generation time at room temperature, strains are easily stored over long periods by freezing, and populations of genetically identical individuals can be easily maintained by virtue of self-fertilization, its primary mode of reproduction (Stiernagle, 2006). While the behavior exhibited by *C. elegans* in the lab on an agar surface is assuredly a limited and biased version of the full behavioral repertoire in natural environments, it is an apparently quite satisfactory environment for the worm to exhibit a search for food by chemotaxis, produce viable eggs when well fed, mate when a rare male makes its appearance (roughly 1 in 700 eggs in lab conditions hatch into a male (Hodgkin and Doniach, 1997)), and communicate with each other via a large repertoire of pheromones (Srinivasan et al., 2012). *C. elegans* can also successfully generate goal-directed behavior in more structured artificial micro-environments (Albrecht and Bargmann, 2011) and pure liquid environments, where serpentine crawling becomes swimming.

### 1.2.2 *C. elegans* nervous system

The adult hermaphrodite has exactly 302 neurons out of a total of 959 somatic cells. Approximately 7000 synapses and 900 gap junctions link these neurons. 20 of the 302 neurons comprise the nervous system of the pharynx, responsible for alimentary pumping, and connected to the rest of the network by a single gap junction (though demonstrably affected by neuromodulators not associated with particular anatomical connections) (Avery and Thomas, 1997). Of the 282 somatic neurons, approximately one third are classifiable as sensory neurons and one third as motor neurons by morphology or functional demonstration. The remaining third of the neurons have no obvious direct sensory function or direct output to muscles or secretory glands and are thus called interneurons. By process of elimination, we guess that their function is purely computational – that is, they interpret a set of signals carrying abstract information (i.e. with no extrinsic meaning outside of the nervous system) from other neurons and produce a set of signals carrying abstract information that direct other neurons to ultimately generate observable behavior. The majority of these interneurons lie in the nerve ring, a ganglion near the head. The role of most interneurons is not well understood, although five sets of “command” interneurons are required for transitions between forward or backward movement states and may encode volitional state (Chalfie et al., 1985; Gray et al., 2005). Perhaps not surprisingly, some non-trivial single-input processing of sensory information is already performed by the sensory neurons themselves<sup>4</sup>; characterizing this first layer of processing is the primary focus of this work.

Each neuron is a member of a class defined by rough morphological symmetry (White et al., 1986). There are 103 somatic neuron classes: 18 singlets, 63 pairs, 1 triplet, 10 quadruplets, 5 hextuplets, and 1 7-fold, 1 9-fold, 2 11-fold, 1 12-fold and 1 13-fold class. The large symmetry classes are comprised of motor neurons with highly regular distribution along the body. Some neurons in pair classes are connected by a gap junction lying on the

---

<sup>4</sup>This neglects the many connections from other sensory neurons and interneurons onto sensory neurons and the multiple-input processing function they suggest.

axis of symmetry. Each neuron class has a three letter name such as AWC, and each neuron has a name that consists of two or three letters or digits appended to its class name (e.g. AWCL).

By several measures, neural connectivity is highly redundant: the mean in-degree (number of neurons that a neuron receives connections from) and the mean out-degree (number of neurons that a neuron sends connections to) are both 7.86, the mean path length between neurons is only 2.87 hops (Varshney et al., 2011), and there are multiple one-hop routes between most neighboring neurons in addition to their direct connection. This lack of obvious network segmentation (with the exception of the pharynx) makes the task of inferring localization of function from structure challenging. The number of hops from a sensory neuron to its closest motor neuron is at the least 2 and at the most 3, suggesting the network is shallow with respect to feed-forward information flow.

Electrophysiological recordings are challenging due the pressurized cuticle of the worm, but those that have been performed in *C. elegans* neurons and the neuromuscular junctions of the parasitic nematode *Ascaris suum* have found that neurons are isopotential and lack action potentials (Liu et al., 2009; Davis and Stretton, 1989). Consistent **with** this absence, the *C. elegans* genome lacks classical voltage-gated sodium channels, although these were likely to have been lost by nematodes as voltage-gated sodium channels were present in the last common ancestor of bilaterians (Liebeskind et al., 2011; Bargmann, 1998). The lack of sodium-based classical action potentials does not rule out other features of nonlinear excitability used for neural coding such as plateau potentials or spikelets generated by other voltage-gated ion channels (Lockery and Goodman, 2009; Faumont et al., 2012).

## Chemosensation

*C. elegans* relies on its ability to sense a diverse set of chemicals to collect data about its environment. Worms will move toward attractive chemicals and away from repulsive chemicals, and over the course of minutes can locate themselves close to an attractant source on a plate. Chemical stimuli regulate the worm’s behavior on a wide range of time scales

from subsecond locomotory responses to lifecycle decisions based on environmental quality assessed over hours (Golden and Riddle, 1982). At least 13 pairs of chemosensory neurons provide the worm with sensory information that drives its behavior (Bargmann and Mori, 1997) and its genome codes at least several hundred chemoreceptors (Bargmann, 2006b). We study two chemosensory neurons that subserve different behaviors.

### **The AWC neuron**

The AWC neuron class consists of a pair of bilaterally symmetric neurons AWCL and AWCR. It is one of three wing neurons, so named for the wing-like appearance of its non-motile sensory cilia. The predominant behavior subserved by these neurons is attractive chemotaxis. AWC can detect at least five different volatile odors, including isoamyl alcohol (IAA) and butanone (BUT) (Bargmann et al., 1993), and we focus on detection of these two odorants in this work. IAA is also sensed by AWA neurons, but chemotaxis assays suggest that for the dominant behavioral response to IAA and BUT, sensation by AWC is necessary and sufficient (Bargmann et al., 1993). During development, functional symmetry is stochastically broken and the specificity for particular odorants between the two neurons partially diverges based on differential receptor expression (Wes and Bargmann, 2001). While the identities of specific odorant receptors are still unknown, transduction is known to be G protein and cGMP mediated. Differential odor detection within a single AWC neuron may depend on different receptors, but genetic analysis suggests they share a common final path (L'Etoile and Bargmann, 2000). Odorants exhibit different adaptation curves leading to odor discrimination over several minutes, but it is not known if odorant identity is somehow encoded in signal dynamics on shorter time scales or if that identity is lost. The major components of the forward path of the AWC signal transduction cascade have been identified based on genetic, behavioral, and activity imaging evidence (Figure 1.1).

AWC has no direct connections to the command interneurons, which suggests that chemotaxis involves some degree of circuit-level computation.

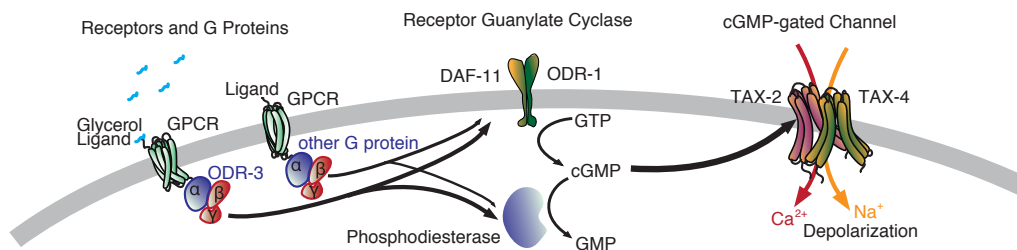


Figure 1.1: Signal transduction cascade in AWC sensory cilia  
Odorant receptors signal through G proteins including ODR-3, which in turn regulates cGMP-gated transduction channels (adapted from Bargmann, 2006a)

## The ASH neuron

The bilateral pair of ASH neurons are polymodal nociceptors that are required for the avoidance response to noxious chemicals, hyper or hypo-osmolarity, and harsh nose touch (Bargmann, 2006a). Ablation of ASH does not modulate regular turning behavior during foraging modes absent of noxious stimuli, supporting its primary role as a detector of noxious stimuli and not a driver of chemotaxis (Gray et al., 2005). Similar to human nociceptors, ASH depends on TRPV channels for transduction (Figure 1.2) although primary transduction to glycerol (GLY), the stimulus we use in this work to probe this neuron, is performed by an unidentified G protein-coupled receptor.

ASH synapses onto the command interneurons AVA and AVD, which in turn connect to motor neurons responsible for driving forward and backward movement, suggesting a more reflexive pathway as compared to AWC-driven chemotaxis. Activating either ASH or AVA and AVD causes an immediate reversal.

### 1.2.3 Worm behavior

We focus on chemotaxis and escape behaviors since they have are subserved by AWC and ASH respectively.

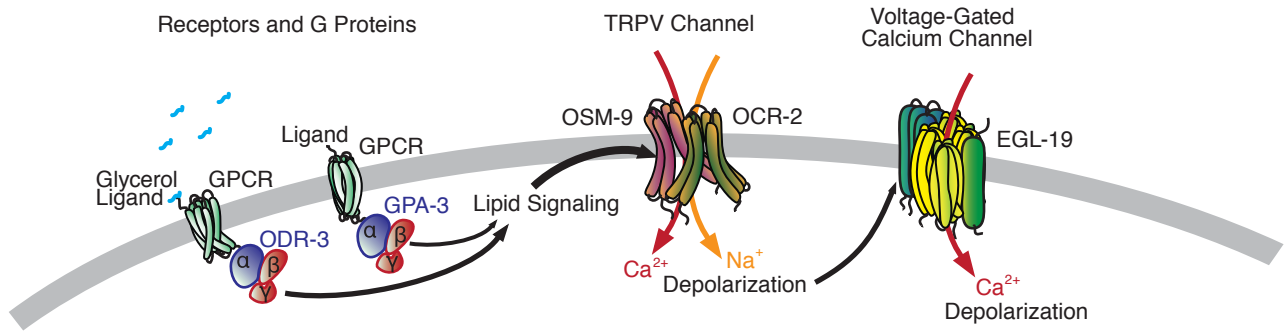


Figure 1.2: Signal transduction in ASH sensory cilia

The glycerol receptor signals through the ODR-3 G protein, which in turn regulates TRPV family transduction channels. (adapted from Bargmann, 2006)

### Undirected chemotaxis

In the presence of a shallow concentration gradient of chemoattractant, such as the gradient that results from spotting the center of an agar plate with liquid chemoattractant, worms will eventually accumulate at the location of maximum concentration. The paths followed by the worms have been described as a biased random walk consisting of bouts of forward serpentine movement (a “run”) interrupted by bouts of stereotyped in-place turn sequences (“pirouettes”) resulting in abrupt reorientation with low correlation to the worm’s prior direction (Pierce-Shimomura et al., 1999). This resembles the well-characterized chemotaxis strategy of *E. coli* (Berg, 2004). In this undirected mode of chemotaxis, only the probability of turning *in some unspecified direction* is modulated by the concentration gradient. Since this form of chemotaxis can be accomplished by single-cell organisms lacking nervous systems, one may question if this mode of locomotion is a hallmark of sophisticated computation (putting aside the complexities of coordinated control of a 95-cell musculature). However, this mode of stochastic search is modulatable by the worm’s state and constitutes a part of a larger set of chemotactic strategies (Iino and Yoshida, 2009).

## Directed chemotaxis

Given sharper sensory cues, such as a steep gradient resulting from two adjacent streams of different odorant concentration under laminar fluid flow through a micofabricated silicone hexagonal post array, the worm can exhibit directionally preferential turning relative to the gradient location, enabling the worm to surf along the border of an attractant area (Albrecht and Bargmann, 2011) and to use a “weathervane” strategy to maintain a specific orientation relative to the gradient field or gradually steer up a strong circularly symmetric gradient (Iino and Yoshida, 2009). Deterministic locomotion along gently curving thermoclines has also been observed and modeled (Hedgecock and Russell, 1975; Luo et al., 2008). All of these chemotactic strategies indicate an ability for klinotaxis, or directed steering in response to spatial distribution of stimuli, suggesting that worms must be able to detect the spatial character of an odor stimulus. It is unlikely that worms smell “in stereo”, despite having bilaterally symmetric chemosensory neurons, since the distance between the openings of the two amphid sensory organs is only 8  $\mu\text{m}$ . Furthermore, on a surface, worms crawl on their side, causing these amphid openings to be vertically aligned and unable to sample distinct x-y locations on the surface. Thus, the acquisition of spatial information is likely the result of integration over time or by head bending rather than by sensing a difference in simultaneous concentration (Ward et al., 1975). In addition to serpentine body turns, the worm displays frequent, faster non-locomotory articulated head movements on a sub-second timescale enabled by the hexagonally symmetric neck muscles, suggestive of a spatial sampling procedure. Integration of proprioceptive and chemosensory information could account for this spatial odor tracking ability. Alternatively, the detection of increased odor during one portion of a head bend could simply increase the amount of time spent in that conformation or increase the strength of the bend, obviating the need for a distinct proprioceptive neural signal.

## Escape

When confronted with a strong noxious stimulus, worms will reliably reverse within a fraction of a second, but they will integrate weak noxious stimuli over  $\sim 10$  seconds before reversing (Chao et al., 2004). A long reversal is often followed by an omega turn, causing a reorientation of direction, followed by a forward run, suggesting a stereotyped sequence of moves.

## 1.3 Dynamical Systems Modeling

In this work we adopt the perspective that we are detectives or reverse engineers – that there is an underlying “real” system for which we are trying to discover the hidden rules of operation. As a first step to discovering these rules, we try to imitate the system by creating a model that acts like the system we are studying, according to criteria that we choose. We hope that the functionally important aspects of the system under study are stable in time, or at least changing slowly enough, so that we may repeat experiments and look for consistent behavior<sup>5</sup>, then create a model that is capable of exhibiting nearly the same behavior, and then zero in on a particular instantiation of the model, as defined by its free parameters, by trying to minimize some error criterion that compares the output of our model to the output we measure experimentally. This is not the only way of looking at things: one may dispense entirely with the notion of a real system and discuss models purely in the context of their fits to empirical data – a philosophy typically adopted by the engineering discipline of *system identification*, from which most of the analytical techniques employed here are borrowed. However, we find that it facilitates intuition and communication to imagine a “ground-truth” system that we are seeking to model. By imagining a well-behaved ground truth, we also feel more justified in studying the subtler qualities of how our models miss the mark – qualities that are not captured in a scalar error criterion.

Once models are on the table, we may step back and ask meta-questions about our models

---

<sup>5</sup>this doesn’t obviate the use of non-deterministic models when appropriate – we just have to relax our definition of consistent to include, for example, consistent probability distributions

– how do we select the models out of many possible choices? what other models would work just as well? how generalizable is our model? How many parameters and hidden variables should we allow? A purely empirical modeler might suggest that we bake all of these meta-questions into our error criterion and model family and bring us back down to earth from meta-land. There are indeed principled ways to answer some of these questions, such as the various proposed “information criteria” for determining the number of parameters to include in a model, but justified use of them relies on simplifying assumptions about the character of experimental noise or system variability, which we often do not know in advance. It is likely that there is no good way to cast all models into a single megaclass, and model selection will continue to be guided by human judgment.

### 1.3.1 Definitions and Basic Properties

A *dynamical system* receives an *input signal*  $u(t)$  and produces an *output signal*  $y(t)$ . A signal is a scalar-valued or vector-valued function of time. For most of this thesis we will deal only with single-input/single-output (SISO) systems – they receive a scalar input signal and produce a scalar output signal. We write the system equation, where  $\mathbf{S}$  is an operator, as:

$$y(t) = \mathbf{S}(u(t))$$

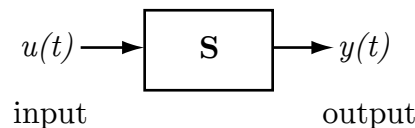


Figure 1.3: A system.

Experimentally measured signals are composed of a finite, discrete set of measurements in time, typically at a fixed interval  $\Delta t$  (although variation in this interval may occur and can be treated, as we do later).

The *time history* of a signal, or informally a *trace*, is a vector composed of *samples*, the value of the signal at successive measurement times, starting from an initial time index  $i = 1$  (corresponding to time  $t = 0$ ) and ending at  $i = T$  samples (corresponding to  $t = (T - 1)\Delta t$ ). In the limit of  $\Delta t \rightarrow 0$ , we can think of the time history as a continuous infinite-dimensional vector. We use the convention that a time history vector is always a column vector which we can write horizontally in a line of text by using the transpose operator:  $[x_1 \ x_2 \ x_3 \ \dots \ x_T]^T$ . For an integral representation of a system (to be described below),  $u(t)$  and  $y(t)$  are replaced by time history vectors  $\mathbf{u}$  and  $\mathbf{v}$ , and  $\mathbf{S}$  can be thought of as a vector-valued function of a vector input. For brevity, we will use  $\mathbf{u}$  for both the continuous function and the time history vector representation of a signal when either can be substituted.

A property of signals important for our needs in this work is *stationarity*. The classical definition is not with respect to a single arbitrary signal but to ensembles of random processes. We use the term here with respect to individual traces as shorthand for the property of *weak self-stationarity*, defined as a trace having mean and autocorrelation functions, obtained by time averaging over a short interval of  $\Delta T$  samples:

$$\mu(i) = \frac{1}{\Delta T} \sum_{j=i}^{i+\Delta T} \mathbf{x}_j$$

$$\phi(i, i + \tau) = \frac{1}{\Delta T} \sum_{j=i}^{i+\Delta T} \mathbf{x}_j \mathbf{x}_{j+\tau}$$

that do not vary significantly over time (Bendat and Piersol, 1966). We will need this property for the model estimation techniques described later.

A *model* of a dynamical system is denoted by an operator  $\mathbf{M}$  with an associated vector  $\boldsymbol{\theta}$  of parameters, which produces a simulated output  $\hat{\mathbf{y}}$  when fed an input signal:

$$\hat{\mathbf{y}} = \mathbf{M}(\mathbf{u}; \boldsymbol{\theta})$$

In general, the approach of *system identification* is to probe a system  $\mathbf{S}$  by driving it with a test ensemble of  $D$  input traces  $\mathbf{u}^1, \mathbf{u}^2, \dots, \mathbf{u}^D$  and recording corresponding output traces  $\mathbf{y}^1, \mathbf{y}^2, \dots, \mathbf{y}^D$ , in the presence of noise, then select a model  $\mathbf{M}$  and estimate its parameters  $\boldsymbol{\theta}$  such that some measure of dissimilarity  $C(\hat{\mathbf{y}}^1, \mathbf{y}^1; \hat{\mathbf{y}}^2, \mathbf{y}^2; \dots; \hat{\mathbf{y}}^D, \mathbf{y}^D)$  is minimized. A typical dissimilarity measure appropriate<sup>6</sup> for comparing fluctuating, stationary signals is *mean squared error* (MSE), which we will see has properties amenable to mathematical analysis. For a single trace,

$$\text{MSE}(\mathbf{y}, \hat{\mathbf{y}}) = \frac{1}{T} \sum_{i=1}^T (\mathbf{y}_i - \hat{\mathbf{y}}_i)^2$$

Prior to computing MSE, we typically subtract the time-mean of each signal, since it is required for certain estimation procedures and since a difference in the mean of two signals that otherwise appear highly similar will dominate the MSE.

A system that is *linear on its inputs*<sup>7</sup> obeys the additivity and homogeneity properties:

$$\text{if } \mathbf{u} = \mathbf{v} + \mathbf{w} \quad \text{then} \quad \mathbf{S}(\mathbf{u}) = \mathbf{S}(\mathbf{v}) + \mathbf{S}(\mathbf{w}) \quad (1.3.1)$$

$$\text{iff } \mathbf{u} = a\mathbf{v} \quad \text{then} \quad \mathbf{S}(\mathbf{u}) = a\mathbf{S}(\mathbf{v}) \quad (1.3.2)$$

A *time invariant* system has the property that its output does not depend explicitly on time, or formally:

---

<sup>6</sup>that is to say, one that jibes with what we consider intuitive about how two signals in this class seem similar or different.

<sup>7</sup>for brevity, a system that is linear on its inputs is referred to as simply a *linear system*. A system may also be linear in other ways, such as linear on a set of parameters, but we will make this distinction when necessary.

$$\text{if } y(t) = \mathbf{S}(u(t)) \text{ then } y(t + \tau) = \mathbf{S}(u(t + \tau)) \quad (1.3.3)$$

for any choice of  $\tau$ . We may think of a time invariant system as being defined by rules that are immutable throughout time.

Linear time-invariant systems, described below, are of particular importance as they are analytically tractable and therefore provide a foothold for analysis of nonlinear, but “near-linear” systems. Furthermore, there is reason to suspect that the validity of the linear systems approximation to many systems found in nature is not a fluke.<sup>8</sup> By the linearization theorem, the behavior of a nonlinear system undergoing small perturbations in the neighborhood of a hyperbolic fixed point (one that has no eigenvalues with real part zero), which commonly arise in dissipative systems, is qualitatively the same as the linearized version. Furthermore, it can be shown that for input ensembles with stationary statistics, adapting systems with the functional goal of maximizing coding efficiency given physical constraints will adapt themselves to operate in a linear coding regime<sup>9</sup> (Laughlin, 1981).

We divide dynamical systems models into two categories: integral and differential models, described below. We start with integral systems since we will refer to them when discussing properties of differential models.

### 1.3.2 Integral Models

Integral models generate the time history of the output of a system as a transformation of the time history of the input. We call them “integral” models because the input-output transformation consists of a composition of functions of the time history of the input, that will typically involve integrals over time. In the context of biology, these models are typically considered to be phenomenological, or black-box, in the sense that they are not intended to mirror specific mechanisms of the system, but are meant to be useful constructs to describe

---

<sup>8</sup>although even more universal is the nonlinear property that all natural systems have – a limited dynamic range, something nicely capturable by the near-linear systems we study here.

<sup>9</sup>this is analogous to the well-established technique of histogram equalization in image processing

operation of the system on its input, and are constructed purely from input-output records with minimal prior assumptions. That being said, the empirical success of certain integral models such as L-N model has bolstered many to suggest a mapping of the specific cascade elements to physiological mechanisms. A point of this work is to show that the application of these phenomenological models can be used as a stepping stone to mechanistic models that make claims about the inner workings of the system, provided some assumptions about the space of possible mechanisms are made.

### Linear Time-Invariant Models

A continuous input signal can be decomposed into an infinite sum of shifted and scaled Dirac delta functions:

$$u(t) = \int_{-\infty}^{\infty} u(\tau)\delta(t - \tau)d\tau$$

If  $\mathbf{S}$  is a linear operator, then by superposition and proportionality,

$$y(t) = \mathbf{S}(u(t)) = \int_{-\infty}^{\infty} u(\tau)\mathbf{S}(\delta(t - \tau))d\tau$$

Defining the *impulse response function*  $h(t) = \mathbf{S}(\delta(t))$ , we have

$$y(t) = \int_{-\infty}^{\infty} u(\tau)h(t - \tau)d\tau$$

which is called the *convolution* of  $u(t)$  and  $h(t)$ , also written as  $(u * h)(t)$ . With a substitution of variables we can also write

$$y(t) = \int_{-\infty}^{\infty} u(t - \tau)h(\tau)d\tau$$

which shows that convolution is commutative:  $a * b = b * a$ . It is also associative:  $a * (b * c) = (a * b) * c$  which we will make use of later.

The impulse response function  $h(t)$  constitutes a complete description of a linear system;

it completely determines the behavior of the system for any given input signal, via the convolution operation. If the impulse response is zero for some  $t > t_{max}$ , then we call the system a finite impulse response (FIR) system with memory  $t_{max}$ .

If  $h(t)$  is zero for all  $t < 0$ , the upper limit of the convolution can be limited to  $t$ :

$$y(t) = \int_{-\infty}^t u(\tau)h(t - \tau)d\tau$$

which implies that the current value of the output only depends on current or past values of the input, and not future values. A linear system with this property is called *causal*. We will be mostly concerned with causal FIR systems, as they define linear systems that are physically realizable and do not show persistent activity (activity that does not eventually die out when there is no stimulus).<sup>10</sup>

For discrete signals, we have an analogous impulse response  $\mathbf{h}$ , based a decomposition of a discrete signal into a sum of scaled and shifted Kronecker delta functions ( $\delta_1 = 1$ , and  $\delta_n = 0$  for all other integers  $n$ ), and we use *discrete convolution* to compute output from input. For a causal FIR system with memory of  $T_{max}$  samples:

$$\mathbf{y}_i = \Delta t \sum_{j=1}^{T_{max}} \mathbf{u}_{i-j} \mathbf{h}_i$$

Notice that for values of  $j$  less than  $T_{max}$ , the above expression includes non-positive indices of  $\mathbf{u}$ . This is because the current output at these early times will depend on values before our the start of our experiment designated as  $t = 0$ . Therefore, we if we wish to have our model produce output values earlier than  $T_{max}$ , we must pad the input – make a guess at what the system input was before we started recording. For simplicity we often drop the  $\Delta t$  scaling factor, by redefining the discrete impulse response function as the system response to a scaled Kronecker delta function, ( $\delta_1 = 1/\Delta t$ ).

---

<sup>10</sup>There are practical issues with a finite memory filter model. We will address the limitation of the FIR assumption in section 1.3.4

## Nonlinear Time-Invariant Models: Wiener/Volterra Expansion

As early as 1883 Volterra (Marmarelis, 2004) observed that, in analogy to the Taylor series as way to approximate a scalar function, a time-invariant transformation of one function  $u(t)$  into another function  $y(t)$  can always be expressed as a series, possibly infinite:

$$y(t) = K_o + \int_{-\infty}^{\infty} K_1(\tau)u(t - \tau)d\tau + \iint_{-\infty}^{\infty} K_2(\tau_1, \tau_2)u(t - \tau_1)u(t - \tau_2)d\tau_1d\tau_2 + \dots$$

Each  $K_n$  term is called a *kernel* and describes the responsiveness of the current output to values ( $K_1$ ), pairwise correlations ( $K_2$ ), or higher-order correlations ( $K_{>2}$ ) at specific time points of the time history of the input. If the zeroth-order kernel (the constant term  $K_0$ ) and first-order kernel  $K_1$  are the only nonzero kernels, this expansion describes a linear system.

Wiener (1958) observed that these kernels are not orthogonal (i.e. zero cross-covariance), therefore causing problems in estimating higher-order kernels, and determined a procedure for deriving orthogonalized kernels. Wiener also prescribed the use of spectrally flat random signals for interrogating nonlinear systems to sample the space of all possible inputs in an unbiased way, giving birth to the field of white-noise methods.

Kernel-based expansions can be unwieldy and do not necessarily lend themselves to an intuitive interpretation of system function. Nevertheless, they can be useful as diagnostic probes of a system, as certain characteristics of higher-order kernels may provide hints as to which cascade models will do a good job of explaining the data.

## Nonlinear Time-Invariant Models: L-N Cascade

A perhaps conceptually simpler departure from linearity is to admit an instantaneous function applied to the output of a linear transformation. This model neatly separates the dynamical, memory aspects of the system transformation from the nonlinear aspects into two sequential operations:

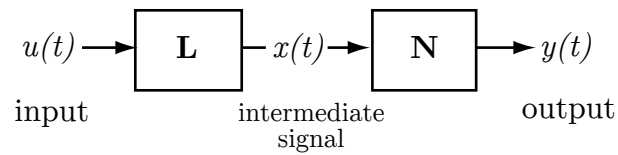


Figure 1.4: L-N model

The system equation

$$\mathbf{y} = \mathbf{N}(\mathbf{L}(\mathbf{u}))$$

can be written

$$y(t) = F\left(\int K(t - \tau)u(\tau)d\tau\right)$$

where  $F$  is a static function and  $K$  is a first-order kernel, or for brevity, *filter*. In practice, we must choose a maximum length, in number of samples, for the filter  $K$ , and a suitable parameterized curve family for  $F$ , typically polynomials up to a certain order or other function bases.

The Volterra kernels of a system can provide a hint that a system is L-N-like; axis-parallel slices of the second-order Volterra kernel of an L-N system will be proportional to the first-order kernel.

### More complex cascade models

It is possible to compose more complex transformations by adding L and N stages at the front or end of a cascade model. Since two adjacent L stages can be unambiguously collapsed into one L stage by convolution, as convolution is associative, and since two adjacent N stages can be collapsed into one N stage by sequential application, without loss of generality we can consider single-chain cascades of alternating L and N stages - L-N, N-L, L-N-L, N-L-N, L-N-L-N, and so on. These longer cascade models gain more expressive power than an L-N model and they may be suggestive of an underlying sequence of physical processes.

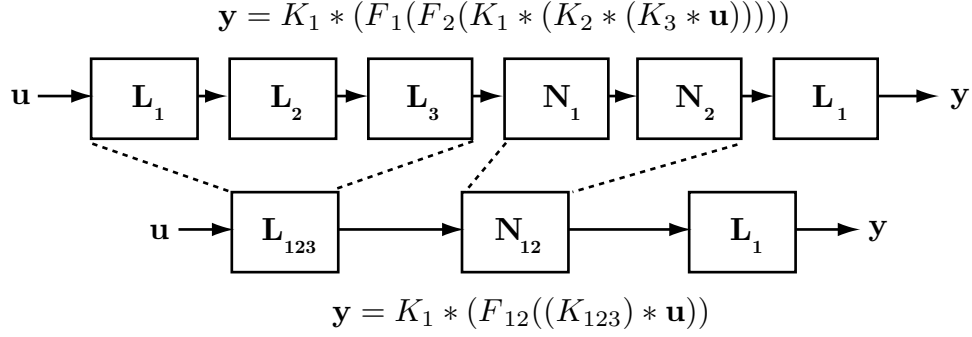


Figure 1.5: Two equivalent serial L-N cascades

Another way to generalize cascade models is to allow the input signal to fan out and follow separate paths through cascade models, then sum them together for output. Korenberg showed, using a constructive procedure, that a finite set of parallel L-N cascades can be constructed to represent any finite-dimensional nonlinear system representable by a Volterra series (Korenberg, 1991).

The system equation for a parallel L-N cascade is:

$$y = \sum_{i=1}^n N_i(L_i(u))$$

Recently there has been much interest in a related parallel cascade model for analyzing spiking systems under the moniker of *spike-triggered covariance* (Brenner et al., 2000), particularly for systems with spatiotemporal input (a MISO system), such as complex cells in visual cortex. This model prescribes a similar model of parallel L cascades, but differs in that a strict procedure for generating L stages is specified (eigenvector decomposition of the response covariance matrix, i.e. the second order Wiener kernel) the N stages and final summation are replaced with a global nonlinear aggregation function  $F$ :

$$y = F(L_1(u), L_2(u), \dots, L_n(u))$$

These models have a great deal of expressiveness, but like Wiener/Volterra series they do

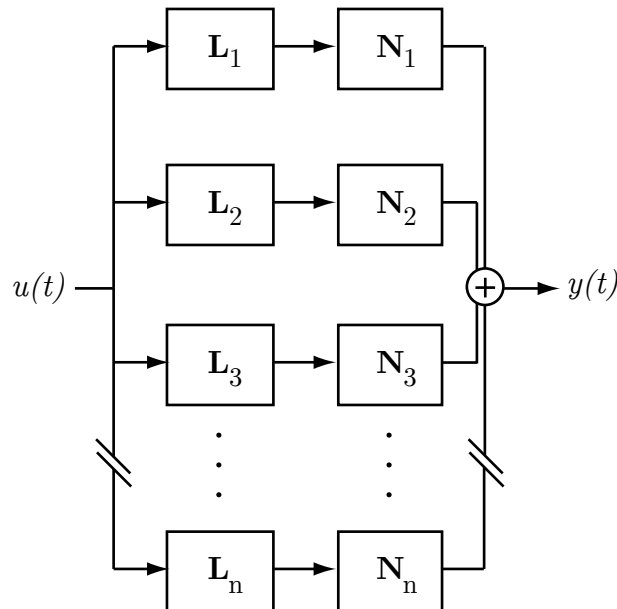


Figure 1.6: Parallel L-N cascade.

not always lend themselves to easy interpretation, especially for purely temporal input data.

### 1.3.3 Differential Models

Differential equation models are the prevalent approach to modeling physical processes evolving in time, particularly autonomous systems, i.e. ones with no input. They describe the way each of a system's primitive objects change as a function of the instantaneous state of all of the system's primitive objects<sup>11</sup>. A subset of these models, ordinary differential equation (ODE) models, limits these primitive objects to be scalar *state variables*, representing concrete qualities such as particle position and velocity, concrete quantities such as chemical concentration, or abstract quantities, such as an internal decision variable in a high-level cognitive model. State variables are often hidden, inaccessible to direct measurement. One way to express systems of ODEs is in the *state-space* representation – a list of equations,

---

<sup>11</sup>we do not address delay differential equations since they seem to fall outside the scope of easily realizable biological mechanisms and can produce fundamentally different behavior.

one equation for each state variable, specifying the rate of change of the state variable as a function of some or all of the other state variables, possibly the state variable itself, possibly the system input, and possibly time itself:

$$\begin{aligned}\frac{dA}{dt} &= f_A(A, B, C, ..Z, u, t) \\ \frac{dB}{dt} &= f_B(A, B, C, ..Z, u, t) \\ &\vdots \\ \frac{dZ}{dt} &= f_Z(A, B, C, ..Z, u, t)\end{aligned}$$

Since we are modeling input/output systems, we need to define an output, so we also allow a final *non*-differential equation to define the output as an instantaneous function of the state variables and possibly the input:

$$y(t) = f_y(A, B, C, ..Z, u, t)$$

Alternatively, we could set the output to be one of the state variables, and thus be specified by a differential equation, but permitting the output to depend instantaneously on state variables gives us the flexibility to treat any composition of the state variables as a system output, and, as it turns out, does not undermine any mathematical results about systems of differential equations that we will need.

In time-invariant systems, none of the state or output equations can have an explicit dependence on time, so the right-hand functions'  $t$  argument is disallowed.

It is also possible to write explicit<sup>12</sup> ODEs involving higher-order derivatives of each state variable, but a such a representation can always be converted into a state-space form, simply by relabeling each higher-order derivative as a new state variable. Here we use only

---

<sup>12</sup>we do not address implicit ODEs since the physical notion of separable state variables can be lost, and if the equations are separable, they can be cast into an explicit form

the state-space representation of ODEs, and we define the *order* of an ODE system as the number of state variables.

To fully specify the behavior of an ODE system in a particular instance, *initial conditions* must also be provided, specifying the state of the system at  $t = 0$ . With these in hand, ODEs can be numerically simulated with little difficulty, using Euler’s method which simulates in discrete, fixed-length time steps and requires only a memory of system state at the last time step.<sup>13</sup> More sophisticated algorithms such as those of the Runge-Kutta family which include memories of system state over several time steps and adaptive time steps can be employed to accurately model systems with large magnitude differences in rates (i.e. a “stiff” system) without having to discretize time more finely through the entire simulation.

ODEs may be considered as a way to compress a description of the behavior of a system, since even low-order ODEs are capable of generating very complicated output; in this sense they are like the source code of a program.

## Linear ODEs

If an SISO system of ODEs obeys linearity and time invariance, the  $f_n$  functions must necessarily be simple linear combinations of their arguments and we can consolidate it into standard matrix form:

$$\frac{d\mathbf{x}(t)}{dt} = \mathbf{M}\mathbf{x} + \mathbf{b}u(t)$$

$$y(t) = \mathbf{c}^T \mathbf{x} + \mathbf{d}u(t)$$

---

<sup>13</sup>difference equations, a subset of recurrence relations, are the discrete analog of differential equations formed by replacing the differential operator with a fixed time-step difference operator, and the equations are only evaluated at discrete time steps. They form the basis of simulating differential equations and generally display analogous behavior to differential equations, so we do not treat them here. However, the nature of discrete jumps can admit some behavior unique to difference equations, such as alternation between two values in a first-order system.

where  $\mathbf{x}(\mathbf{t})$  is a column vector of state variables  $[A \ B \ \dots \ Z]^T$  (not to be confused with a signal's column time vector),  $\mathbf{M}$  is a static matrix holding the coefficients of the right-hand side interaction terms in our state-space equations and  $\mathbf{b}, \mathbf{c}, \mathbf{d}$  are static column vectors<sup>14</sup>.  $\mathbf{b}$  describes the weights of the fan-out of the input to all of the state variables.  $\mathbf{c}$  describes the how the state variables are weighted before being summed to produce the output. If there is no direct dependence of the output on the input (i.e. “pass-through” connections that bypass the state variables of the system altogether),  $\mathbf{d}$  is zero, which we assume here for simplicity, although it is not required for the analysis.

The solution to the time evolution of the state variables, and consequently the output, of a linear system with ongoing input can be computed using matrix exponentials, where  $\mathbf{x}(0)$  is a vector of initial conditions of the state variables:

$$\mathbf{x}(t) = e^{t\mathbf{M}}\mathbf{b} \int_0^t e^{-t'\mathbf{M}}u(t') dt' + e^{t\mathbf{M}}\mathbf{x}(0)$$

The impulse response of a differential linear system can be computed via the inverse Laplace transform of the transfer function:

$$h(t) = \frac{1}{2\pi i} \int_{\gamma-i\infty}^{\gamma+i\infty} H(s)e^{st}ds$$

where the transfer function is computed by

$$H(s) = \mathbf{c}(s\mathbf{I} - \mathbf{M})^{-1}\mathbf{b} + \mathbf{d}$$

where  $\gamma$  is a real number chosen to be to the right of all of the singularities of  $H(s)$ .

Equivalently, the impulse response can be computed by solving for the time evolution of the system with zero input  $u(t) = 0$  given initial conditions of  $\mathbf{x}(0) = \mathbf{b}$ .

In the next sections, we catalog the impulse responses and their parameter dependencies

---

<sup>14</sup>For multiple-input multiple-out (MIMO) systems,  $\mathbf{b}, \mathbf{c}$ , and  $\mathbf{d}$  become matrices and  $u$  and  $y$  become vectors but the analysis is similar.

of certain low-order causal SISO LTI systems. Knowledge of these general behaviors will guide our model selection. We restrict ourselves to stable systems – in the sense of systems whose state variables will stay bounded given a bounded input – since this appears to be a ubiquitous quality of the cellular systems we are studying here. For the same reason we limit ourselves to systems with no input pass-through. For simplicity, we ignore gain terms on the input or output, since for linear systems these will simply scale the output.

### First-order stable linear system (1FF)

The simplest system within our restricted set of study is given by

$$\frac{dA}{dt} = -\tau_a^{-1}A + u$$

$$y = A$$

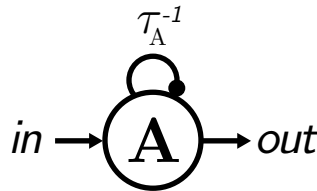


Figure 1.7: First-order ODE system

The filter for this system is a decaying exponential with time constant  $\tau_A$  so the system functions as a low-pass filter. The filter has a jump discontinuity at  $t = 0$ .

### Second-order linear systems

Two-variable linear systems are the classic example in the study of linear dynamical systems, since they are simply analyzable but show some diversity of behavior.

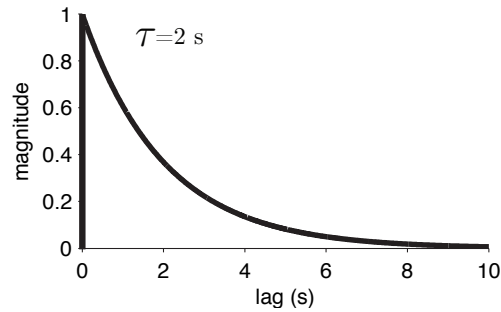


Figure 1.8: Filter of a first-order system

### Second-order feedforward (2FF)

Neglecting gain factors on the input or output, a two-state variable feedforward system (aside from self-feedback) is given by

$$\frac{dA}{dt} = -\tau_a^{-1}A + u$$

$$\frac{dB}{dt} = k_{AB}A - \tau_b^{-1}B$$

$$y = B$$

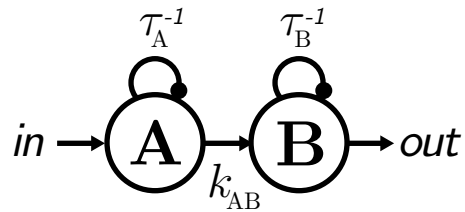


Figure 1.9: Second order feed-forward system

The system filter is a difference of exponentials:

$$h(t) = k_{AB} \frac{\tau_A \tau_B}{\tau_A - \tau_B} (e^{-t/\tau_A} - e^{-t/\tau_B})$$

Notice the symmetry of the system: there is no change in the value of the expression if the values of  $\tau_B$  and  $\tau_A$  are swapped. This implies that we cannot deduce which state variable is faster and which is slower in this system just by looking at the filter. Also notice that the interaction constant  $k_{AB}$  does not affect the time course of the filter; it acts only as an overall gain term.

We can rewrite the filter as a product of a rising exponential and a falling exponential (and a constant positive gain term):

$$h(t) = k_{AB} \frac{\tau_A \tau_B}{|\tau_A - \tau_B|} (1 - e^{-t/\tau_{RISE}}) e^{-t/\tau_{FALL}}$$

where  $\tau_{FALL}$  is equal to the larger of  $\tau_A$  and  $\tau_B$  and  $\tau_{RISE} = \tau_A \tau_B / (\tau_A - \tau_B)$ . The latter expression is equivalent to saying that the effective rise rate  $k_{RISE} = k_A + k_B$ , the sum of the self-feedback rate constants. A plot of this filter, along with the rising and falling single exponential terms, shows the single exponentials enveloping the filter:

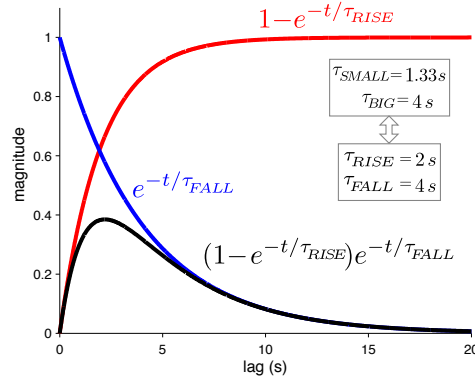


Figure 1.10: Envelopes of a difference of exponentials.

This demonstrates that the larger time constant mostly determines the decay of the filter, and the ratio of the product to the sum of the self-feedback time constants mostly determines the rise of the filter. If  $\tau_{LARGE} \gg \tau_{SMALL}$  (a “separation of timescales” assumption), then  $\tau_{RISE} \approx \tau_{SMALL}$ .

The peak time of the filter is exactly

$$t_{peak} = \frac{\tau_A \tau_B \log(\tau_A / \tau_B)}{\tau_A - \tau_B}$$

which of course has the same  $\tau_A, \tau_B$  symmetry as the filter. Here is an isocline showing pairs of  $\tau_A$  and  $\tau_B$  that produce a  $t_{peak} = 2s$ :

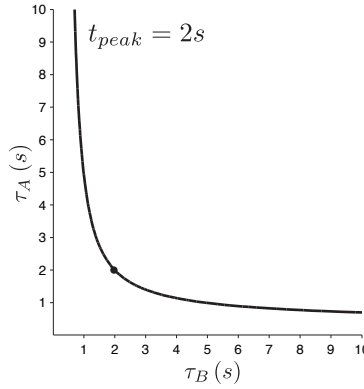


Figure 1.11: The relationship of time constants producing a particular filter peak time

If we assume the separation of timescales, we have

$$t_{peak} \approx \tau_{FAST}(\log \tau_{SLOW} - \log \tau_{FAST})$$

To reiterate: we can't pin down which state variable A or B has which time constant (the slower or the faster, and consequently the rise or the fall) without further information or prior assumptions. We can, however, potentially extract two process time constants by fitting an analytical filter curve to a filter we have measured.

### Second-order feedforward degenerate (2FFd)

If  $\tau_A = \tau_B$ , we obtain an alpha function for the filter:

$$h(t) = k_{AB} t e^{-t/\tau_A}$$

This result is not immediately obvious by substituting the same variable for  $\tau_1$  and  $\tau_2$  into the 2FF filter expression, since the denominator of the fraction term would be zero. However, the exponentials also cancel so nothing explodes and the filter remains well behaved regardless of the choice of  $\tau$ 's.

We can plot the filters for the 2FF (in black) and 2FFd systems (in red) as we vary one of the  $\tau$ 's:

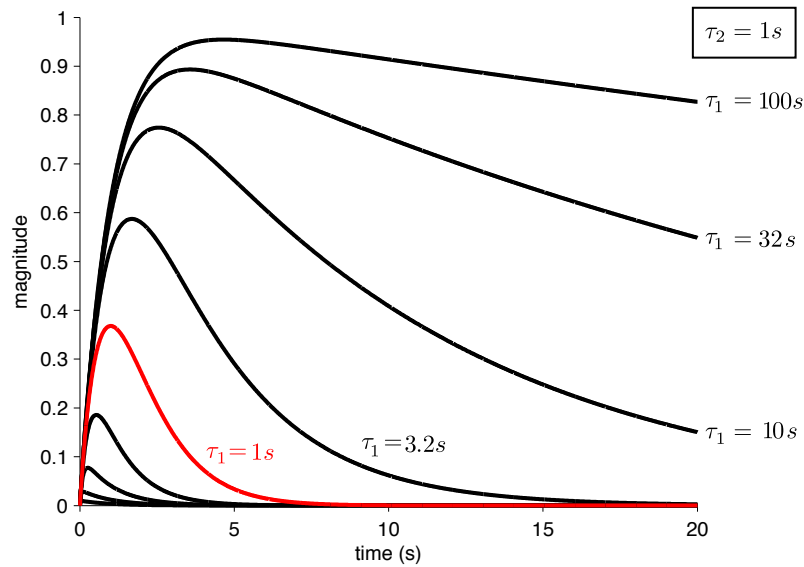


Figure 1.12: How a 2FF filter changes as we vary one time constant

This system has the same filter as a critically damped harmonic oscillator (see next section). A final property: the 2FF and 2FFd filters, along with all feed-forward chains (nFF), must be monophasic, and therefore, they function as low-pass filters.

### Second-order feedback (2FB)

If we allow feedback from the second state variable to the first, we can produce a system with oscillatory or decaying oscillatory behavior. The lobes of the filter will be close to constant width.

The stable second order models are equivalent to a damped harmonic oscillator, a model of a mass-on-a-spring with velocity-proportional friction. This model can exhibit three qual-

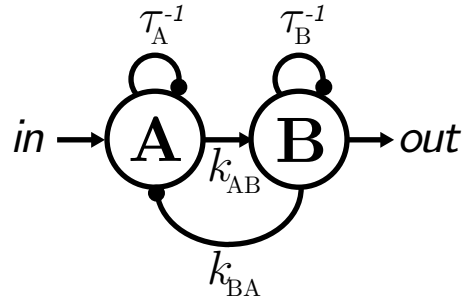


Figure 1.13: Second-order feedback ODE model.

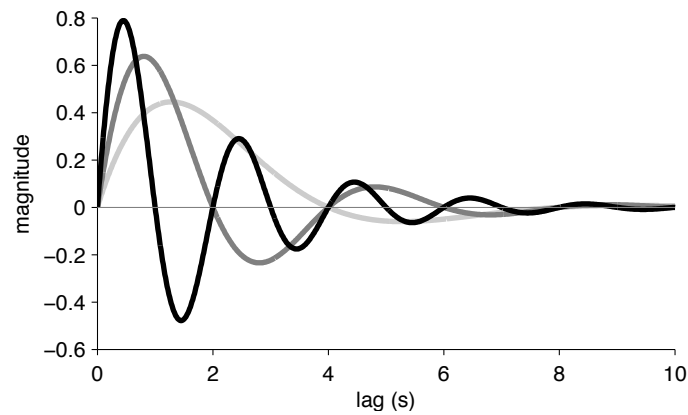


Figure 1.14: Filters of underdamped second-order systems

itative behaviors: underdamped (leading to a filter with decaying oscillations), overdamped (leading to a difference of exponentials as seen before), and critically damped (filter with an alpha function). Designers of passive control or sensor systems try to adjust the physical parameters of their system (by strengthening or weakening a frictional element, for example) to be as close to critically damped as possible, since a critically damped system will react to a transient perturbation by decaying to equilibrium as fast as possible without overshoot.

### Third-order linear systems and higher

The space of models expands wildly from here. We cover one tractable example and its application in chapter 3. With the addition of a third state variable, more flexibility is gained in the phasic structure of the filter of a stable system. For example, third order models can produce biphasic filters that are continuous at zero but have different lobe widths, as we

shall see.

## Nonlinear ODEs

The expressions on the right-hand side of ODEs do not need to be significantly more complicated than linear combinations for a wide variety of complex behavior to arise. Systems only need to have three state-space variables to have the potential to display chaotic behavior.<sup>15</sup> A single fixed nonlinear form can switch between a wide variety of behaviors depending on the choice of parameters.

### 1.3.4 Estimation of Integral Models

Once we have selected a model, we need a procedure to determine what choice of model parameters generate a model that best fits input/output data, a problem of estimation. All of the estimation procedures here require that both input and output signals be stationary.

#### Model Performance Evaluation

To evaluate the performance of a model with respect to a particular input-output record, in this work we use variance-accounted-for, a measure which scales relative to the variance of the output signal:

$$\text{VAF} = 100\% * \left( 1 - \frac{\text{var}(\mathbf{y} - \hat{\mathbf{y}})}{\text{var}(\mathbf{y})} \right)$$

A 100% VAF indicates that a model has perfect predictive power, whereas a 0% VAF indicates that a model has no more predictive power than a constant trace set equal to the mean response, and values can be unboundedly negative.

We want our model to have generality, at least across trials within one class of stimulus pattern (but hopefully to other stimulus ensembles as well). Since a non-parametric integral model typically has many degrees of freedom, it has the flexibility to overfit, or capture noise fluctuations that vary from trial to trial. To prevent overfitting we can use cross-validation,

---

<sup>15</sup>The Poincaré-Bendixson theorem eliminates the possibility of chaotic dynamics in continuous second-order systems.

by measuring the performance of a choice of model parameters against a set of hold-out test data not used in the estimation process. For iterative learning processes beyond linear regression, using probe set error, as opposed to estimation dataset error, at each iteration becomes important for high degrees of freedom models.

## Linear models

Robust estimation of dynamical systems using white noise methods and correlational techniques were developed before the advent of fast digital computers. Ingenious methods were devised for performing this process in an on-line fashion – in real-time during the process of data collection – by analog electrical circuits capable of computing a running estimate of the autocorrelation of an output signal and the cross-correlation of the input and the output. For a Gaussian white-noise signal run through a linear process with an additive Gaussian noise process,  $\mathbf{h}$  is correctly estimated by<sup>16</sup>

$$\hat{\mathbf{h}} = \phi_{uy} / \phi_{uu}$$

The explosion of modern computing resources allows large datasets to be recorded and computations done off-line after the experiment, allowing a more direct and flexible approach. We consider the free parameters of our model to be the sample values of our impulse response vector  $\mathbf{h}$ , then cast it as a minimization problem:

$$\hat{\boldsymbol{\theta}} = \underset{\boldsymbol{\theta}}{\operatorname{argmin}}(MSE(y, \hat{y}))$$

We solve this problem for our linear integral model. We typically allow our model filters to have some acausal portion as consistency check. If the estimation procedure produces a filter with a substantial acausal element, it suggests that we have misapprehended something about our experimental setup, about the relative timing of our input and output, about a

---

<sup>16</sup>In spiking systems, *spike-triggered averaging* (de Boer and Kuyper, 1968) is equivalent to this calculation, under the assumption of the output spikes being generated by a Poisson process whose rate is determined by the output of a linear, or as we shall see, a linear-nonlinear process.

feedback process that affects our measurement of the *input* signal, or about the randomness of our input (a smart enough system could learn to anticipate a test signal with predictable temporal structure and therefore give the appearance of seeing into the future). So we allow  $\mathbf{h}$  to have non-positive indices ( $\mathbf{h}_0, \mathbf{h}_{-1}, \mathbf{h}_{-2}$ ), and we write the discrete convolution as

$$\mathbf{y}_i = \sum_{j=-M}^{N-1} h_j u_{i-j}$$

where  $M$  is the number of acausal samples and  $N$  is the number of causal samples. Thus  $\mathbf{h}$  is an  $N + M$  component vector.

Then copies of the discrete convolution equation for each time index  $i$  can be rewritten as a matrix equation

$$\mathbf{y} = \mathbf{U}\mathbf{h}$$

where  $\mathbf{U}$  is a matrix formed by taking each row to be a time-shifted copy of the input:

$$\begin{bmatrix} u(M) & \cdots & u(2) & u(1) & 0 & \cdots & 0 \\ u(M+1) & \cdots & u(3) & u(2) & u(1) & \cdots & 0 \\ \vdots & \ddots & \vdots & \vdots & \vdots & \ddots & \vdots \\ 0 & \cdots & u(T) & u(T-1) & u(T-2) & \cdots & u(T-N) \\ 0 & \cdots & 0 & u(T) & u(T-1) & \cdots & u(T-N+1) \end{bmatrix}$$

This matrix equation illustrates that our model output is linear with respect to our filter samples (which we already knew by the commutativity of convolution), and it has the general form of a linear regression problem. Taking the gradient of the MSE with respect to  $\mathbf{h}$  and setting it to zero solves for the minimum MSE and gives our procedure for calculating  $\hat{\mathbf{h}}$ :

$$\hat{\mathbf{h}} = (\mathbf{U}^T \mathbf{U})^{-1} \mathbf{U}^T \mathbf{y}$$

The solution of this matrix equation, easily implementable in any mathematical calcula-

tion package, depends on a matrix inversion and takes  $O(TH^3)$  calculations (Golub and Van Loan, 1996) where  $H$  is the number of samples in  $\mathbf{h}$  and  $T$  is the number of samples in the traces. This formulation allows us to use different stationary input test ensembles, provided the inversion of the observation matrix is well-conditioned. As long as the probability distribution of input values is symmetric about zero, the solution will be unbiased for a linear model. Note that the input and output must be zero-centered before estimation or our filter estimate will be biased.

### Wiener-Volterra models

The reverse correlation method has been extended to estimate higher-order Wiener kernels (Lee and Schetzen, 1965) and since a Volterra expansion is linear on kernel samples, even for higher kernels, it can be treated as a linear regression problem. However, each successive kernel typically requires exponentially more data to accurately estimate (Marmarelis, 2004), making them difficult to measure. In practice, it is rare to see an attempt at an expansion beyond the second or third kernel.

### L-N models

The cross-correlation of two Gaussian signals is simply proportional to the cross-correlation of the two signals after one of the signals is passed through an instantaneous nonlinearity, provided the nonlinearity is not a perfectly even function (such as  $x^2$ ) (Bussgang, 1952). Excluding systems with perfectly even nonlinearities, this implies that the same estimation approach can be used to estimate the L stage of an L-N model *as if the N function weren't there*.<sup>17</sup>

After estimating the L stage and obtaining an estimated  $\hat{K}(\tau)$  function, the input can be convolved with the kernel to compute an estimate of an intermediate function  $\hat{x}(t)$ . A linear regression between  $\hat{x}(t)$  and  $y(t)$  is then performed to estimate the parameters of the

---

<sup>17</sup>Bussgang's theorem does not guarantee that the best possible fit will be discovered by this approach for any system; it only guarantees that *if* the underlying system is an L-N model and the test input is Gaussian, the procedure will converge to it.

nonlinear function  $\hat{F}(x)$ . If the L-N model is a good qualitative fit to the data, a scatter plot of  $y(t)$  versus  $\hat{x}(t)$  should lie close to a single line. In practice, effects due to the finite size of our experiments may introduce bias in this one-shot estimation procedure; we can use an iterative procedure to try and correct for this, although convergence properties have not been proven Hunter and Korenberg (1986). L-N models fall under the statistical framework of generalized linear models (GLM's), for which maximum likelihood methods of estimation have been developed.

Since L-N model estimation is the approach we take for most of our main results, we provide a flowchart for estimating an L-N model from experimental data in the Appendix.

### 1.3.5 Estimation of Differential Models

The inference of a low-order<sup>18</sup> continuous differential model (i.e. the selection of a model and estimation of its parameters) directly from input-output data in a system with hidden state variables is a less straightforward problem, for several reasons. First, the problem of model selection is under-determined; for a given observed input-output behavior, though it may be unambiguously characterized, for example, by a linear filter (integral model), there are infinitely many differential models that will produce the behavior. Thus, to be well posed, we need to constrain our question by, for example, asking what minimal order model satisfies a given error criterion given the test data at hand or by restricting our models to a specific state-variable interaction topology (e.g. ARMAX difference-equation models). Second, once a putative model is selected, estimating the parameters (in this case, interaction constants) cannot always be cast as a linear regression; in general, differential model output has a nonlinear, and often non-monotonic and non-continuous dependence on its parameters (even for a differential system that is linear *on its inputs*). Third, in this class of operators, there is not an obvious expansion basis for successively more accurate approximation, such as Wiener/Volterra kernel series or parallel L-N models.

---

<sup>18</sup>low-order is the key – for example, we can readily construct a high-order difference equation model to exactly implement the procedure of convolution with a finite length filter – it is called a *tapped delay line* and is a general scheme for the implementation of electronic FIR filters.

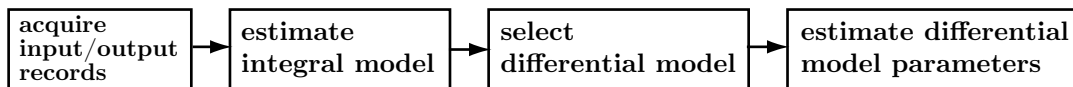


Figure 1.15: Our approach to differential model identification

If the state variables are not entirely hidden but partially observable, even indirectly as noisy mixtures, there are principled procedures for estimating parameters of differential models given exponential-family noise models, such as those based on expectation-maximization, although their performance properties are difficult to analyze aside from special cases (Ghahramani and Hinton, 1996; Ghahramani and Roweis, 1999). Subspace methods based on matrix factorization (Van Overshee and De Moor, 1996) have emerged as an effective technique for direct estimation of unconstrained discrete (difference-equation) linear state space models, provided enough input-output data is available. The inference of differential models is an active area of machine learning research.

The simple heuristic we follow in this work for estimation of differential models is to first estimate a (non-parametric) integral model, and then on the basis of qualitative considerations of the results of the integral model, select a (parametric) differential model, then fit the differential model to the data to determine parameters (Figure 1.15).

### 1.3.6 Differential versus Integral Models

Integral models have mechanical, often one-shot, methods for estimation, but do not in and of themselves imply mechanism. We do not imagine a biological mechanism that performs convolution by operating on a sample by sample basis. Integral models are typically non-parametric models, in that they are not defined by a chosen parameterization. This can be beneficial for avoiding prior bias in model selection. When cast into a contemporary probabilistic framework, these models force us to be very clear about delineating what our prior assumptions are. In actual implementation, integral models can be considered to

be very high-parameter models, with parameters being the samples of the kernels and the coefficients of the nonlinear function expansions. Therefore, overfitting must be carefully treated and mechanistic interpretations are necessarily limited.

One issue with integral models is that we must set the maximum limit for the memory of components or the lengths of kernels. There will necessarily be finite-size effects and the introduction of some estimation bias. Furthermore, we cannot possibly model long-memory components with a finite-memory system, and the existence of processes with ranges of timescales across many orders of magnitude seems to be a ubiquitous feature of biological systems. Research into multi-timescale or scale-free nonparametric dynamical models seems warranted.

Finally, the integral models described here are incapable of ongoing intrinsic behavior such as that of a frictionless harmonic oscillator. Treating an oscillation as being caused by an external input is one way to address the shortcoming analytically, but it does nothing to explain the phenomenon we presumably seek to understand.

Therefore, there is benefit to attempting to fit a differential model to the results we obtain from an integral model analysis, that do not suffer from the above issues but in general are difficult to find effective, robust procedures for estimating.

There are also hybrid models consisting of a mixture of differential and integral elements motivated by the ease of conceptualization in some cases. For example, a sum over time history or integral may appear as a right-hand term in a system of differential equations, or a derivative operator may appear in a block model. However, to analyze them, the components of the model typically need to be converted into all of one type or another.

With respect to modeling neural activity, we think of integral models as descriptions of *what* neurons compute – their signal processing function, and we equate differential models with putative mechanism, as descriptions of *how* neural systems compute. Due to the under-determined nature of the inference of differential models, we cannot necessarily argue that a particular topology of state variable interactions is correct, even though it provides an

excellent fit to input/output data with a low number of parameters. However, the existence of a low-order model can provide a framework for understanding perturbations to the system that may help uncover underlying simple mechanisms.

# Chapter 2

## Fourier Analysis of Responses in AWC for Circuit Dissection<sup>1</sup>

Before proceeding to dynamical systems modeling, we demonstrate another method of non-parametric analysis of time series data: the Fourier decomposition of a signal into a sum of sinusoidal components of different frequencies. This method is useful for revealing oscillatory behavior in signals without the need for an explicit dynamical model. Here we use it to analyze the subtle differences in wild type and mutant responses for the purposes of dissecting a surprising circuit interaction between a sensory neuron and one of its downstream neighbor interneurons.

### 2.1 Summary

Many neurons release classical transmitters together with neuropeptide co-transmitters whose functions are incompletely understood. Here we define the relationship between two transmitters in the olfactory system of *C. elegans*, showing that a neuropeptide-to-neuropeptide

---

<sup>1</sup>Portions of this chapter were previously published as *Neuropeptide feedback modifies odor-evoked dynamics in *Caenorhabditis elegans* olfactory neurons*, (2010) Nature Neuroscience, co-authored by Sreekanth Chalasani<sup>†</sup>, Saul Kato, Dirk Albrecht<sup>†</sup>, Takao Nakagawa<sup>†</sup>, L. F. Abbott<sup>‡</sup> and Cornelia I. Bargmann<sup>†</sup>, and have been reproduced with permission. S. Kato performed signal processing analysis of neural activity data. <sup>†</sup>Howard Hughes Medical Institute, The Rockefeller University, New York, New York, USA. <sup>‡</sup>Department of Neuroscience and Department of Physiology and Cellular Biophysics, Columbia University College of Physicians and Surgeons, New York, New York, USA. Copyright is held by Nature Publishing Group.

feedback loop alters sensory dynamics in primary olfactory neurons. The AWC olfactory neuron is glutamatergic and also expresses the peptide NLP-1. Worms with *nlp-1* mutations show increased AWC-dependent behaviors, suggesting that NLP-1 limits the normal response. The receptor for NLP-1 is the G protein-coupled receptor NPR-11, which acts in postsynaptic AIA interneurons. Feedback from AIA interneurons modulates odor-evoked calcium dynamics in AWC olfactory neurons and requires INS-1, a neuropeptide released from AIA. The neuropeptide feedback loop dampens behavioral responses to odors on short and long timescales. Our results point to neuronal dynamics as a site of behavioral regulation and reveal the ability of neuropeptide feedback to remodel sensory networks on multiple timescales.

## 2.2 The neuropeptide gene *nlp-1* limits local search behavior

The AWC neuron releases the neurotransmitter glutamate, which activates AIB interneurons via the glutamate-gated cation channel GLR-1 and inhibits AIY interneurons via the glutamate-gated chloride channel GLC-3 (Chalasani et al., 2007) (Figure 2.1A). AWC also expresses genes that encode predicted neuropeptides, including the buccalin-related peptide NLP-1 (Nathoo et al., 2001). We characterized the function of NLP-1 by examining local search behavior, in which worms increase their turning rates during the initial 15 min after they are removed from food. Local search depends on AWC activity, and the rate of turning provides a quantitative measurement of AWC signaling (Gray et al., 2005). A null mutant for *nlp-1*, generously provided by the *C. elegans* knockout consortium, had a higher turning rate than wild-type worms during local search (Figure 2.1B). Like wild type worms, *nlp-1* mutants stopped turning after 15 min off food (data not shown). This behavioral profile suggests that *nlp-1* inhibits AWC-induced turning behavior. NLP-1 reporter genes are expressed in AWC, ASI, PHB and BDU neurons and in the intestine (Nathoo et al., 2001). The enhanced turning defect in *nlp-1* mutants was rescued by transgenic expression

of *nlp-1* in AWC neurons, but not by expression in ASI neurons (Figure 2.1B and data not shown). Overexpression of *nlp-1* in AWC neurons of wild-type worms reduced the turning rate during local search (Figure 2.1B). The opposite effects of *nlp-1* null mutants and gain-of-function transgenes suggest that this neuropeptide can be an instructive determinant of turning rates. AWC-dependent turning behavior is reduced in worms with mutations in the vesicular glutamate transporter gene *eat-4* or in the glutamate receptors *glr-1* or *glc-3*; these defects are the opposite of those in *nlp-1* mutants (Chalasani et al., 2007). Double mutants between *nlp-1* and *eat-4*, *glr-1* or *glc-3* had reduced turning rates, resembling the worms in which mutations affected glutamate signaling (Figure 2.1B). This result suggests that NLP-1 functions as a co-transmitter whose effects are apparent only when the classical transmitter glutamate is also released: glutamate from AWC stimulates turning, and NLP-1 from AWC decreases the magnitude of this effect.

## 2.3 NLP-1 acts through the G protein-coupled receptor NPR-11

The *C. elegans* genome encodes  $\sim 100$  G protein-coupled receptors (GPCRs) related to characterized neuropeptide receptors (<http://www.wormbase.org/>). To identify the receptor for NLP-1, we examined GPCRs that lack known ligands, focusing on those that are expressed in neurons connected to AWC (Wenick and Hobert, 2004; Etchberger et al., 2007). The orphan GPCR NPR-11, whose closest characterized homolog is the *Drosophila* neuropeptide F receptor 1, was one candidate. We found that *npr-11* null mutants, like *nlp-1* mutants, had increased turning during AWC-dependent local search behavior (Figure 2.1C and data not shown).

Worms with double *nlp-1 npr-11* mutations resembled the single mutants in turning behavior, as expected for a ligand-receptor pair that acts together and not additively (Figure 2.1C). In addition, the *npr-11* mutation fully suppressed the effects of *nlp-1* overexpression on turning behavior (Figure 2.1C). This result indicates that *npr-11* is necessary for the

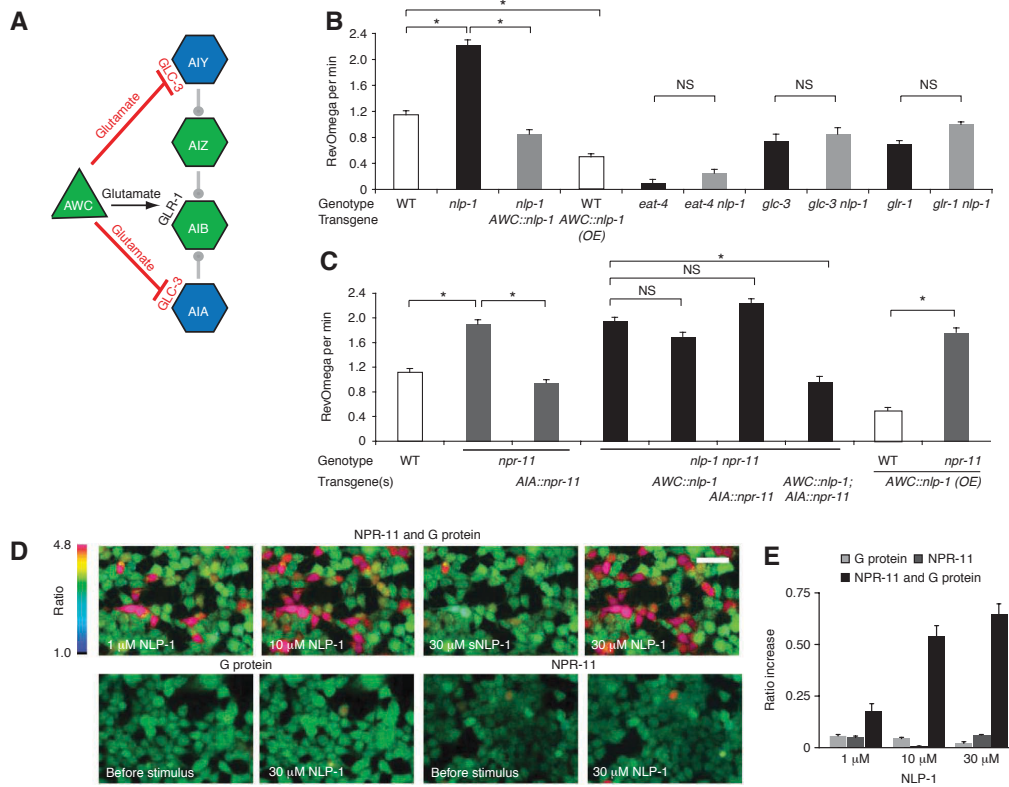


Figure 2.1: AWC releases NLP-1, which acts on NPR-11 in AIA

(A) AWC sensory neurons, downstream interneurons, and relevant glutamate receptors (from this work (AIA) and ref. 9). (B, C) Local search behavior 7–12 min after removal from food. RevOmega, coupled reversal-omega behaviors characteristic of local search. Analysis of *nlp-1* mutants (B) and *npr-11* mutants (C). In all figures, WT indicates control N2 strain, *AWC::nlp-1* indicates *nlp-1* cDNA under AWC-selective *odr-3* promoter, *AWC::nlp-1*(OE) indicates the same plasmid injected at high concentrations, *AIA::npr-11* indicates *npr-11* cDNA under AIA-selective *gcy-28.d* promoter. Error bars, s.e.m.; \* $P < 0.05$  by t-test or t-test with Bonferroni correction, as appropriate; NS, not significant. Complete behavioral data with all genotypes and time points are in Supplementary Table 1. (D, E) Response of *npr-11*- and  $G\alpha 16Z$ -, *npr-11* or  $G\alpha 16Z$ - transfected HEK 293 cells to an NLP-1 peptide and a scrambled NLP-1 peptide (sNLP-1). (D) Pseudocolor images of fura2-labeled cells indicating fluorescent ratio intensities. Scale bar, 100  $\mu$ m. (e) Average calcium response of all cells in the window ( $n = 10$  fields for *npr-11* and  $G\alpha 16Z$ ,  $n = 8$  for *npr-11* and  $n = 7$  for  $G\alpha 16Z$ ). Means and s.e.m. are shown.

biological activity of *nlp-1*, as predicted if *npr-11* encodes an *nlp-1* receptor.

Reporter genes for *npr-11* are expressed in two postsynaptic targets of AWC, the AIA and AIY interneurons, and in other neurons (Wenick and Hobert, 2004) and data not shown). The *npr-11* behavioral defect in local search behavior resembled the defect after AIA interneurons are killed with a laser (Chalasani et al., 2007), and the *npr-11* defect was fully rescued by transgenic *npr-11* expression in AIA interneurons under the *gcy-28.d* promoter (Figure 2.1C). These results suggest that release of NLP-1 from AWC neurons activates the NPR-11 GPCR on AIA neurons. In agreement with this hypothesis, the turning behavior of *nlp-1 npr-11* double mutants was rescued only when *nlp-1* was expressed in AWC and *npr-11* was expressed in AIA together in the same strain (Figure 2.1C). We obtained a biochemical confirmation of the genetically inferred ligand-receptor relationship for NLP-1 and NPR-11 by expressing NPR-11 in HEK 293 cells together with the promiscuous G protein  $\alpha 16Z$  (Mody et al., 2000), and exposing the cells to synthesized MDANAFRMSFamide, an amidated peptide corresponding to one of four predicted peptides encoded by *nlp-1*, MDANAFRMSFamide. NPR-11-expressing cells responded to micromolar concentrations of the peptide with calcium transients typical for GPCR activation (Figure 2.1D). We observed no responses to scrambled NLP-1 peptide in untransfected cells or in cells expressing the receptor or G protein alone (Figure 2.1D, E).

## 2.4 AWC inhibits AIA interneurons through glutamate and NLP-1

We investigated the relationship between AWC and AIA interneurons using genetically encoded calcium indicators of the GCaMP family, which emit increased fluorescence upon calcium binding (Tallini et al., 2006; Tian et al., 2009). *C. elegans* neurons are thought to lack sodium-based action potentials, but express voltage-gated calcium channels (Lockery and Goodman, 2009), and calcium signals in these neurons correlate with neuronal depolarization (Suzuki et al., 2003; Clark et al., 2006; Ramot et al., 2008; Mellem et al., 2002; Chronis

et al., 2007). Previous results suggest that AWC neurons have basal activity at rest, are hyperpolarized by addition of odors and are strongly activated by odor removal (Chalasani et al., 2007). We found that AIA interneurons had the opposite response, showing large transient calcium increases upon odor addition (Figure 2.2A,B). Odor responses in AIA required sensory input from AWC, as they were strongly attenuated when AWC neurons were killed using a laser microbeam (Figure 2.2C,D). These results suggest that AWC forms inhibitory synapses onto AIA, as suggested for the synapses between AWC and AIY (Figure 2.1A and (Chalasani et al., 2007)). In the simplest model, basal AWC activity at rest tonically inhibits AIA; when odor is added, AWC is hyperpolarized, tonic inhibition of AIA is reduced, and AIA becomes active.

Both glutamate and NLP-1 contributed to odor-evoked calcium responses in AIA. AIA responses to odor were diminished in *eat-4* mutants that lack the vesicular glutamate transporter and in *glc-3* mutants that lack a glutamate-gated chloride channel (Figure 2.2E,F). The involvement of *glc-3* is consistent with its known expression in AIA, its molecular identity as an inhibitory glutamate-gated channel, and the prediction that the AWC-to-AIA synapse is inhibitory (Wenick and Hobert, 2004; Horoszok et al., 2001). Worms with mutations in *nlp-1* also had a diminished response in AIA interneurons, which was partly rescued by expression of *nlp-1* in AWC neurons (Figure 2.2G). The partial rescue of *nlp-1* may be due to variable expression of transgenes or to a combined action of *nlp-1* in AWC and additional neurons.

Although a dual action of glutamate and NLP-1 on AIA calcium signals was consistent with the behavioral analysis, the relationship between the transmitters was unexpected. In turning behavior, glutamate and NLP-1 had opposite effects, but in AIA calcium imaging experiments, the effects of *nlp-1* and *glc-3* were congruent. This distinction suggests that the behavioral effect of NLP-1 cannot be entirely explained by its observed effect on AIA activity, and prompted further examination of neurons in the AWC circuit.

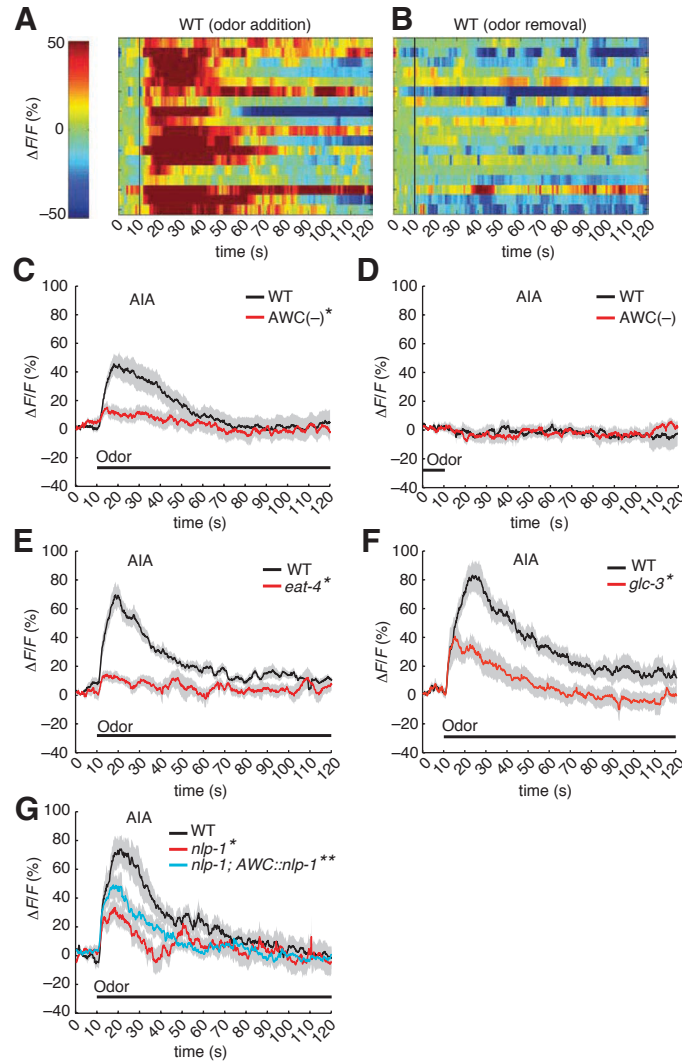


Figure 2.2: Calcium responses in AIA interneurons require AWC glutamate and NLP-1

(A, B) Heat maps showing the ratio of change in fluorescence to total fluorescence in AIA neurons expressing GCaMP2.2b15; addition (A) and removal (B) of odor stimulus at  $t = 10$  s in each recording ( $n = 18$ ). (C, D) Average GCaMP fluorescence change in AIA neurons in wild-type (WT;  $n = 18$ ) and wild-type AWC-ablated worms ( $n = 12$ ) on addition (C) and removal (D) of odor. (E–G) Mutant AIA responses. (E) *eat-4* ( $n = 18$ , WT  $n = 18$ ). (F) *glc-3* ( $n = 16$ , WT  $n = 16$ ). (G) *nlp-1* ( $n = 18$ , WT  $n = 18$ ) and AWC::*nlp-1* cell-selective rescue ( $n = 18$ ). In all imaging figures, odor is a 10–4 dilution of isoamyl alcohol. Light gray shading indicates s.e.m. \*Significantly different from wild type; \*\*significantly different from *nlp-1* mutant ( $P < 0.05$ , t-test with Bonferroni correction).

## 2.5 AWC responses are modulated by NLP-1

The activity of sensory neurons such as AWC is thought to be defined primarily by sensory input and not by network interactions. Unexpectedly, calcium imaging of the odor-evoked response in AWC neurons revealed alterations in *nlp-1* mutants. In both wild type and *nlp-1* worms, initial calcium responses to odor removal peaked within 10 s of odor removal (Figure 2.3A–C and Supplementary Figures 2.6 and 2.7). However, in *nlp-1* mutants, the first peak was frequently followed by large secondary calcium transients that continued for at least 2 min after odor removal, the longest duration that was practical for calcium imaging (Figure 2.3B,C). Thus, NLP-1 signaling suppressed AWC calcium transients for a long period after odor removal. To quantitatively describe the altered activity in *nlp-1* mutants, we used a discrete Fourier transform to analyze the temporal character of the AWC calcium response to odor removal. Fourier analysis is well suited to reveal oscillatory or repeating signals, which appeared by inspection to be present in traces from *nlp-1* mutants. Indeed, spectral analysis showed increased power in a mid-frequency domain in *nlp-1* mutants, with a significantly greater contribution than in the wild type from periodic components between 0.033 Hz and 1 Hz (period 1–30 s) (Figure 2.3D). The effects were statistically detectable at all time points and suggest the presence of irregular slow oscillations with a preferred period near 20 s. Cell-selective transgenic expression of *nlp-1* in AWC resulted in partial but significant rescue of the defect (Figures 2.3C, D and Supplementary Figure 2.6). The irregular oscillating signal was not observed in the absence of odor, excluding trivial optical or mechanical artifacts (Supplementary Figure 2.6), but it was observed to some degree in wild-type traces as well as *nlp-1* traces, indicating that it is a component of the normal AWC response.

We also observed enhanced secondary AWC calcium signals in *npr-11* mutants after odor removal (Figure 2.3E–G and Supplementary Figures 2.6 and 2.7). Normal AWC calcium signals were restored by transgenic expression of *npr-11* in AIA neurons (Figure 2.3G, H and Supplementary Figure 2.6). The functional effect of a receptor in AIA on odor responses

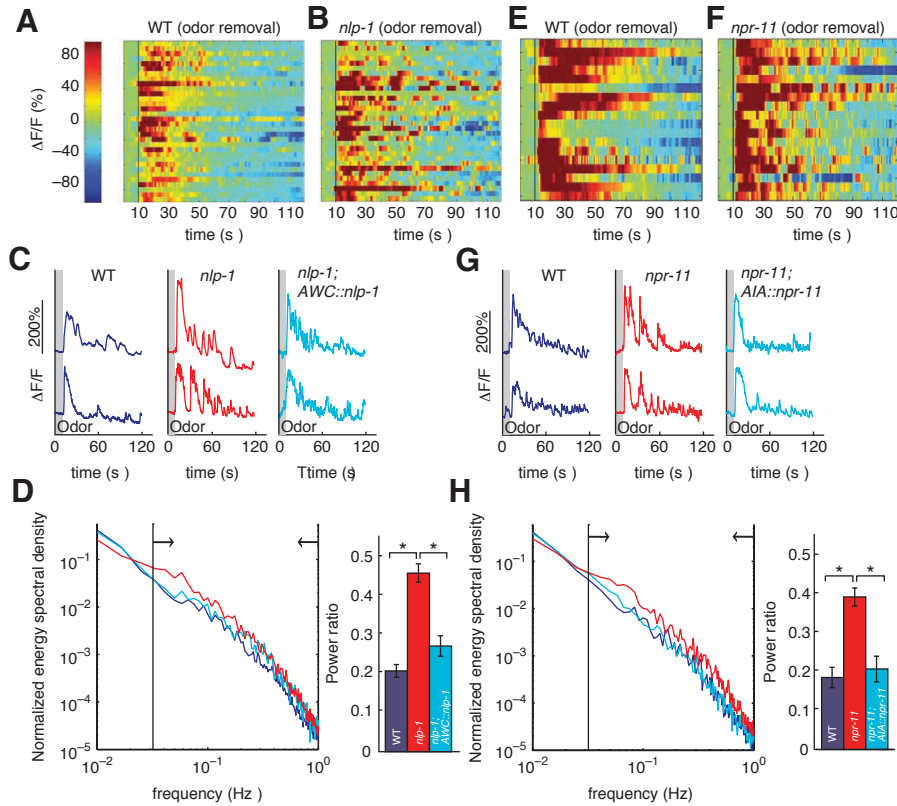


Figure 2.3: Altered AWC calcium responses in *nlp-1* and *npr-11* mutants

(A,B,E,F) Heat maps showing ratio change in fluorescence to total fluorescence in AWC neurons expressing G-CaMP1.0. Odor was removed at 10 s in each recording. (A) Wild type ( $n = 32$ ); (B) *nlp-1* ( $n = 32$ ); (E) wild type ( $n = 18$ ); (F) *npr-11* ( $n = 18$ ). (C,G) Representative AWC calcium responses from individual wild-type worms, *nlp-1* (C) and *npr-11* mutants (G), and rescued strains. (D,H) Fourier power analysis of AWC calcium responses in *nlp-1* (D) and *npr-11* mutants (H). Left, normalized energy density spectrum averaged across all calcium traces of each genotype; arrows indicate range of the middle frequency band (color code on right). Right, the average power ratio of the middle frequency band (0.033–1 Hz) across all calcium traces of each genotype; error bars, s.e.m. \* $P < 0.05$  (t-test with Bonferroni correction).

in AWC supports the existence of feedback from AIA to AWC. In summary, these results suggest that release of NLP-1 from AWC, sensed by NPR-11 in AIA, results in feedback onto AWC that suppresses secondary calcium transients after odor removal. If modulatory feedback from the circuit contributes to normal AWC activity, other synaptic mutants could also affect AWC odor responses. Indeed, AWC responses to odor removal were reduced in *eat-4* mutants, which lack glutamatergic transmission from AWC and other neurons, and prolonged in *unc-31* mutants, which have reduced neuropeptide release from all neurons (Lee et al., 1999; Sieburth et al., 2007) (Supplementary Figure 2.7C,D). These results suggest that the long-lasting AWC responses to odor removal are affected by synaptic inputs, with positive inputs from glutamatergic neurons and negative inputs from peptidergic neurons.

## 2.6 *nlp-1* mutants are defective in AWC odor adaptation

The results described above suggest that neuropeptide signaling and feedback influence long-lasting dynamics in AWC neurons. The 15-min local search behavior is one example of a sustained AWC-dependent behavior; a second sustained AWC-dependent behavior is olfactory adaptation, a behavioral change in which prolonged exposure to an odor leads to reduced chemotaxis to that odor (Colbert and Bargmann, 1995) (Figure 2.4A,B). Worms with mutations in *nlp-1* or *npr-11* failed to adapt to odors after a 60-min exposure (Figure 2.4B), although they did adapt after a 90-min exposure (Supplementary Figure 2.8A). Like the defects in local search behavior, the olfactory adaptation defects were rescued by transgenic expression of *nlp-1* in AWC and transgenic expression of *npr-11* in AIA, respectively (Figure 2.4B). Signaling components that are required cell-autonomously for olfactory adaptation in AWC include GPCR regulators, TRPV channels and a cyclic GMP-dependent protein kinase (Colbert et al., 1997; L'Etoile et al., 2002; Palmitessa et al., 2005; Matsuki et al., 2006; Yamada et al., 2009; Kaye et al., 2009). However, the effects of adaptation on AWC activity have not been described. We found that wild-type worms that had been adapted to odor

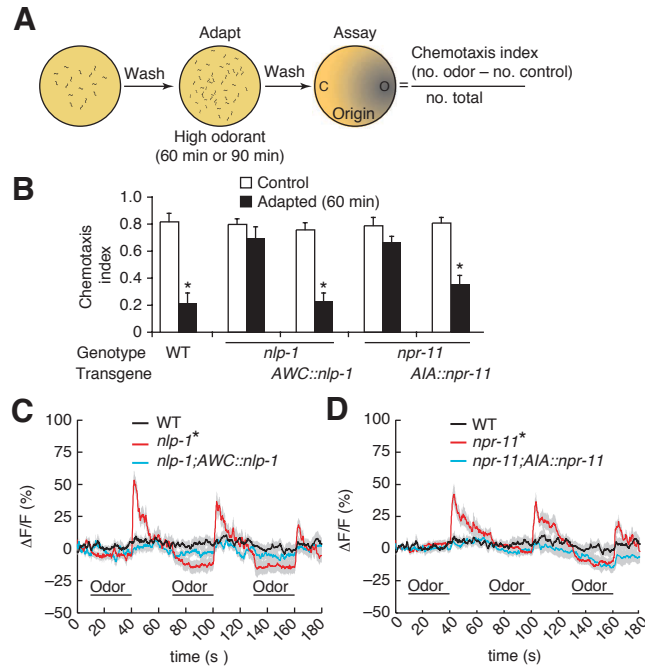


Figure 2.4: Worms with mutations in *nlp-1* and *npr-11* are defective in olfactory adaptation. (A) Schematic diagram of adaptation assay. (B) Adaptation in *nlp-1* and *npr-11* mutants, and cell-selective rescue. Error bars, s.e.m. \* $P < 0.05$  (t-test with Bonferroni correction). (C,D) AWC calcium responses in wild-type, *nlp-1* and *AWC::nlp-1* transgenic rescued worms (C) and wild-type, *npr-11* and *AIA::npr-11* transgenic rescued worms (D) adapted for 60 min ( $n = 12$  each). Odor pulses are marked. Light gray shading indicates s.e.m. \*Significantly different from wild type ( $P < 0.05$ , t-test with Bonferroni correction).

for 60 min failed to respond to odor removal with AWC calcium transients, suggesting that adaptation blocked an early step of AWC signaling (Figure 2.4C). By contrast, both *nlp-1* and *npr-11* mutants that had been exposed to odor for 60 min responded with AWC calcium transients after odor removal (Figure 2.4C,D). Transgenic expression of *nlp-1* in AWC and *npr-11* in AIA neurons restored the wild-type AWC calcium response (Figure 2.4C,D). These results indicate that NLP-1 release from AWC, acting on the NPR-11 receptor in AIA, generates feedback that reduces the primary AWC response to odor removal after adaptation.

## 2.7 INS-1 is a candidate feedback signal from AIA

The results described above suggest that AIA releases a signal that suppresses odor-evoked calcium responses in AWC. The insulin-related neuropeptide INS-1, which is expressed in AIA, modulates the function of the ASE gustatory neurons in a salt conditioning assay (Tomioka et al., 2006), suggesting that INS-1 is a candidate signal from AIA to sensory neurons. Therefore, we investigated the effects of *ins-1* mutations on AWC-regulated behaviors. Like *nlp-1* and *npr-11* mutants, *ins-1* mutants showed increased turning in AWC-dependent local search behavior (Figure 2.5A). Double *ins-1 nlp-1* mutants resembled each single mutant, suggesting that these genes act in a common process (Figure 2.5A). An *ins-1* mutation fully suppressed the effects of NLP-1 overexpression on turning behavior, indicating that *ins-1* activity is necessary for the biological effects of *nlp-1* (Figure 2.5A). Expression of *ins-1* is found in multiple neurons including AIA, RIC, ASI and AWC (Tomioka et al., 2006). Transgenic expression of *ins-1* from an AIA-selective promoter rescued turning behavior in the *ins-1* mutant, but expression from AWC-, ASI- or RIC-selective promoters did not (Figure 2.5A and data not shown). These results suggest that *ins-1* is required in AIA neurons. In double mutant studies, *nlp-1 ins-1* mutants were restored to normal turning behavior only when *nlp-1* was expressed in AWC and *ins-1* was also expressed in AIA (Figure 2.5A). Double *nlp-1* (overexpressor) *ins-1* mutants were restored to the behavior of *nlp-1* (overexpressor) strains when *ins-1* was expressed in AIA (Figure 2.5A). These experiments support the idea that *ins-1* acts in AIA neurons.

In calcium imaging experiments, *ins-1* mutants had secondary AWC transients after odor removal, with temporal properties similar to *nlp-1* and *npr-11* mutants (Figure 2.5B and Supplementary Figure 2.9). AIA-specific expression of *ins-1* significantly rescued the altered odor response in AWC neurons, suggesting that AIA neuropeptides influence AWC activity (Figure 2.5B and Supplementary Figure 2.9).

AWC-dependent olfactory adaptation also required *ins-1*. Like *nlp-1* and *npr-11* mutants,

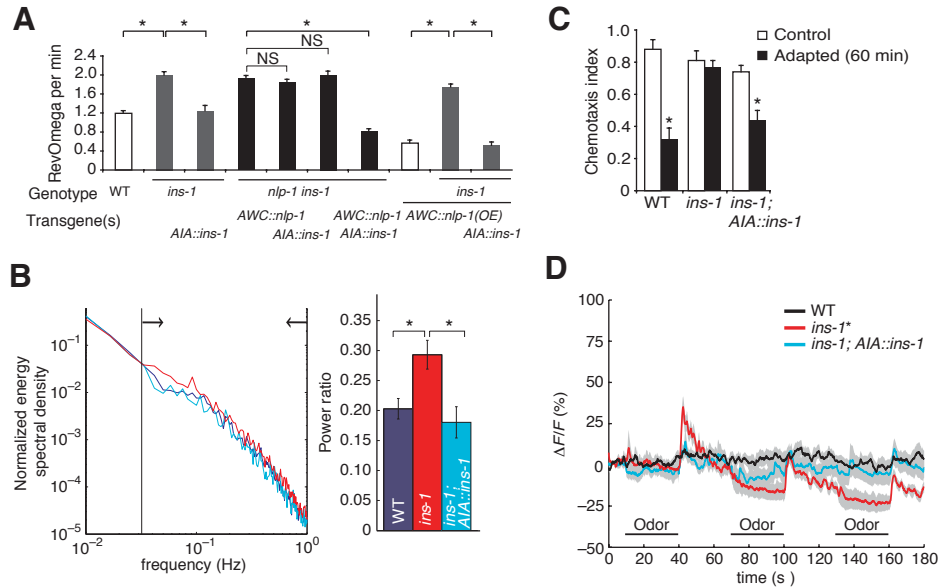


Figure 2.5: *ins-1* is a component of the *nlp-1-npr-11* pathway.

(A) Local search behavior 7–12 min after removal from food. RevOmega, coupled reversal-omega behaviors characteristic of local search. *AIA::ins-1*, *ins-1* cDNA expressed under *AIA*-selective *gcy-28.d* promoter. Error bars, s.e.m. \* $P < 0.05$ , t-test with Bonferroni correction. (B) Fourier power analysis of AWC calcium responses in *ins-1* mutants. Left, the normalized energy density spectrum averaged across all calcium traces of each genotype; arrows indicate range of the middle frequency band (color code on right). Right, the average power ratio of the middle frequency band (0.033–1 Hz) across all calcium traces of each genotype; error bars, s.e.m. \* $P < 0.05$  (t-test with Bonferroni correction). (C) Adaptation in *ins-1* mutants, and cell-selective rescue. \*Different from unadapted control ( $P < 0.05$ , t-test). Error bars, s.e.m. (D) AWC calcium responses in wild type, *ins-1* and *AIA::ins-1* rescued transgenic worms adapted for 60 min ( $n = 12$  each). Odor pulses are marked. Light gray shading indicates s.e.m. \*Different from wild type at  $P < 0.05$ , t-test with Bonferroni correction.

*ins-1* mutants did not adapt after a 60-min exposure to odor but did adapt partially after 90-min (Figure 2.5C and Supplementary Figure 2.8). Adaptation in *nlp-1 ins-1* double mutants was similar to adaptation in each single mutant, suggesting that these two genes affect a common pathway (Supplementary Figure 2.8C). Moreover, AWC neurons in *ins-1* mutants exposed to odors for 60 min showed a calcium response after odor removal, unlike wild-type worms in the same conditions (Figure 2.5D). Both the behavioral adaptation and the neuronal correlate of adaptation observed in calcium imaging were rescued by transgenic expression of *ins-1* in AIA (Figure 2.5C,D and Supplementary Figure 2.8). These results suggest that INS-1 released from AIA acts directly or indirectly on AWC sensory neurons to limit their activity.

## 2.8 Discussion

Many neurons release both classical neurotransmitters and neuropeptides (Marder and Bucher, 2007; Nassel and Homberg, 2006; Burnstock, 2004). Our results suggest that AWC releases both the classical neurotransmitter glutamate and the neuropeptide NLP-1 to modulate behavior (Supplementary Figure 2.9E). The glutamate signaling pathway promotes local search and odor chemotaxis, whereas the neuropeptide pathway limits local search and promotes odor adaptation. Glutamate signals are interpreted by multiple glutamate receptors on interneurons (Chalasani et al., 2007), and NLP-1 is sensed by NPR-11 on AIA interneurons. These interneurons then release INS-1, which directly or indirectly limits AWC activity and behavior. In one straightforward model, INS-1 is released from active AIA neurons when odor is present; the INS-1 released during a short odor exposure inhibits repetitive calcium transients from AWC neurons when odor is removed, and the prolonged INS-1 release during a long odor exposure has a stronger effect, completely suppressing AWC calcium transients upon subsequent odor removal. This feedback loop may act as a gain control circuit to dampen the responses of AWC neurons to strong stimuli, like negative feedback in other neuronal systems (Demb, 2008). In this interpretation, the increased oscillations in *nlp-1*

and other mutants result from ungoverned high-gain signaling in AWC.

A number of inhibitory pathways involving a single neuropeptide are known; this pathway is unusual in its apparent requirement for two neuropeptides from two neurons, working in a feedback loop. Several properties of this feedback loop remain to be determined. For example, we do not know when NLP-1 and INS-1 are released with respect to food or odor cues, and with respect to AWC and AIA activity. If the peptides are released when the neurons are active, NLP-1 would be released in alternation with INS-1 and not simultaneously; the slow biochemical timescale of G protein signaling may permit temporal integration across asynchronous activity of AWC and AIA(Stein et al., 2007). Another missing component of the feedback model is the receptor for INS-1, as mutation of the one characterized *C. elegans* insulin receptor gene, *daf-2*, did not mimic or suppress *ins-1* mutations as predicted for an *ins-1* receptor (data not shown). INS-1 antagonizes DAF-2 in the developmental dauer larva pathway(Pierce et al., 2001), and can act either as an agonist or an antagonist of DAF-2 in food-regulated thermal learning and salt learning paradigms(Tomioka et al., 2006; Kodama et al., 2006), but *C. elegans* has more than 30 insulin-regulated peptides, and DAF-2 may not be the only receptor for this peptide family. Precedent for alternative insulin receptors exists in mammals, where GPCRs are receptors for the insulin-related relaxin peptides(Ivell and Einspanier, 2002).

The behavioral functions of INS-1 in AWC olfactory adaptation are related to its functions during ASE salt chemotaxis learning, where INS-1 from AIA suppresses chemotaxis after salt is paired with starvation(Tomioka et al., 2006)<sup>33</sup>. It will be interesting to investigate whether NLP-1 or another sensory peptide initiates ASE salt chemotaxis learning, and whether INS-1 signaling alters ASE sensory dynamics. Although we specifically examined the relationship between AWC and AIA, the AIA interneurons also receive synaptic input from neurons that sense food, tastants, pheromones and repellents<sup>1,33,42</sup>. This connectivity might enable AIA to act as a local integrator of sensory information.

There is increasing evidence that peripheral olfactory signaling in many species is mod-

ulated by top-down signals, internal states and neuromodulators. State-dependent inputs affect olfactory signaling in rodents, acting as early as the synapses of the olfactory sensory neurons (Wachowiak et al., 2009; Gomez et al., 2005). In *Drosophila*, tachykinin peptides expressed by local interneurons mediate presynaptic inhibition of olfactory receptor neurons (Ignell et al., 2009). The modulation of primary sensory neurons (Stein et al., 2009) is a prominent feature of pain-sensing pathways; we suggest that it will also be prominent in olfactory systems. In *C. elegans*, the use of specific mutants allows these feedback mechanisms to be directly linked to olfactory responses and behaviors, and also reveals their functional diversity. The neuropeptide feedback loop described here damps AWC output, whereas a different modulatory pathway involving the receptor guanylate cyclase GCY-28 can regulate an AWC switch from behavioral attraction to repulsion (Tsunozaki et al., 2008). The *C. elegans* genome contains about 113 genes that encode more than 250 predicted neuropeptides, a rich potential source of behavioral variability<sup>10,47,48</sup>. Our experiments reveal neuropeptide-regulated dynamic properties of *C. elegans* neurons that correlate with the dynamics of behavior. The prolonged AWC calcium signals in *nlp-1*, *npr-11* and *ins-1* mutants correlate with their increased turning during local search behavior. The reduced AWC calcium signals after prolonged odor exposure correlate with olfactory adaptation, which is reduced in *nlp-1*, *npr-11* and *ins-1* mutants. Further studies of the AWC circuit should generate a better understanding of the relationship between behavior and the time-varying acute responses of AIA, sustained responses of AIB, and repetitive responses of AWC and AIY (Chalasani et al., 2007). Together with previous findings in *C. elegans* mechanosensory neurons (Kindt et al., 2007), these results suggest that circuit input tunes sensory responses to external stimuli based on sensory history and internal states, generating a rudimentary form of decision making.

## 2.9 Experimental Methods

### 2.9.1 Calcium imaging

To generate an AIA imaging line, GCaMP2.2b (Tian et al., 2009) was expressed under the *gcy-28.d* promoter (Tsunozaki et al., 2008), which is expressed strongly in AIA neurons and weakly in RIA, ASK, AVJ and other cells. The AWC GCaMP1 imaging line has been described (Chalasani et al., 2007). The lines were scored quantitatively for AWC local search behaviors, and those with normal responses were used for calcium imaging. Worms were trapped in a custom-designed microfluidic device made of the transparent polymer PDMS in which animals are restrained in a small chamber matching their dimensions, exposed to odors in liquid streams under laminar flow, and monitored using wide-field fluorescence microscopy (Chalasani et al., 2007; Chronis et al., 2007). Fluorescence from the cell of interest was captured after the presentation of isoamyl alcohol ( $9.2 \times 10^{-4} \text{M}$ ) and after odor removal 5 min later.

We used MetaMorph and a Coolsnap HQ (Photometrics) camera to capture stacks of TIFF images at  $10 \text{ frames s}^{-1}$  during the addition and removal of odor stimulus. A region of interest encompassing the cell was identified in all frames and the average fluorescence intensity recorded. A Matlab (7.0R14, MathWorks) script used the data generated by MetaMorph to plot the imaging responses. The average fluorescence of the region of interest was generated by subtracting the recorded value from the average intensity of the background region of a similar area. The average fluorescence in a 3 s window ( $t = 1\text{--}4 \text{ s}$ ) was set as  $F_0$ . The percent change in the fluorescence intensity for the region of interest relative to  $F_0$  was plotted for all stacks, and these data were used for further analysis. Raw traces were corrected for fluorescence bleaching by subtracting a fixed correction function obtained by fitting an exponential curve to wild-type control traces using the equation  $y(t) = 100\% * (e^{-t/\tau} - 1)$  where  $t$  is time and  $\tau$  is the time constant. As bleaching rates varied among neurons, separate time constants were obtained for AWC ( $\tau = 330.7 \text{ s}$ ; 95% confidence interval, 327.1–334.4 s;

$R^2 = 0.91$ ) and AIA ( $\tau = 615.5$  s; 95% confidence interval, 607.2–623.8 s;  $R^2 = 0.86$ ).

Because the irregular secondary calcium transients in AWC were not visible in averaged traces, we plotted the ratio of change in fluorescence to total fluorescence for individual traces in heat maps in Figure 2.3 and Supplementary Figures 2.6 and 2.9. The wild-type controls for each figure were interleaved with mutants tested over the same time period.

## 2.9.2 Local search behavior

Individual worms were scored for exploratory behavior in the presence of food (5 min), immediately after removal from food (1–12 min) and after long times off food (35–40 min)<sup>6, 9</sup>. All turns and reversals were scored by eye, by an investigator blind to the genotype of the worm. Reversals and turns were identified as described<sup>6</sup>. Results in Figures 2.1 and 2.5 show turning rates scored 7–12 min after removal from food, and are reported as RevOmega values, which represent reversals coupled to omegas. Qualitatively similar results were obtained when large reversals or omega turns were scored individually (data not shown). Data were analyzed using Perl scripts to calculate reversal and omega frequencies.

## 2.9.3 Adaptation assays

Adaptation assays were performed as described<sup>26</sup>. Worms were washed and plated on 3% assay agar plates. We placed 16  $\mu$ l of isoamyl alcohol on agar plugs on the plate lid and sealed the plates with Parafilm to create the conditioning plate. After 60 min or 90 min, worms were washed and tested for chemotaxis on fresh plates. Controls were treated identically except that isoamyl alcohol was omitted from the conditioning plate. For imaging experiments, worms were conditioned for 60 min with or without isoamyl alcohol and then loaded into the device for calcium imaging.

## 2.9.4 Discrete Fourier transform

The plots in Figures 2.3D,H and 2.5B and Supplementary Figures 2.6 and 2.9D were generated by transforming data in the time domain (the raw fluorescence trace  $y(t)$ ) into the

frequency domain ( $Y(f)$ ), using the Matlab function `fft` (discrete Fourier transform), which computes

$$Y(f_k) = \sum_{j=0}^{N-1} y(t_j) e^{\frac{-2\pi i}{N} k j}$$

where  $k = 0 \dots N - 1$ ,  $N = 1,200$  and  $i = \sqrt{-1}$

at 1,200 equally spaced frequencies from  $f_0 = 0$  to  $f_{1199} = 10$  Hz, the sampling rate. Aliasing, or contribution from oscillatory components at higher than the Nyquist frequency (5 Hz), is negligible based on the rapid drop-off of the Fourier transform with increasing frequency because the dynamics of calcium fluorescent indicators is slower than the sampling rate. The normalized energy spectral density was then calculated for each trace and averaged across each group of traces at each  $f_k$  sample point to give  $\left\langle |Y(f_k)|^2 / \sum_{f_1 \leq f_k \leq f_{N/2}} |Y(f_k)|^2 \right\rangle_{\text{trials}}$  versus  $f_k$  (Figures 2.3D,H and 2.5B). The value  $|Y(f_0)|$  represents the mean of the entire time-domain vector  $y(t)$  and was excluded from the calculation of energy spectral density normalization and band power ratio (described below), although including the value in the calculations did not significantly affect results. Values of  $f > f_{N/2}$  were also excluded from calculations owing to the redundancy of the magnitude of the second half of the discrete Fourier spectrum when performed on real-valued signals. For simplicity, no smoothing or windowing was applied to the energy spectral density. Applying various windowing schemes did not significantly affect quantifications (data not shown).

This representation of calcium signal data was chosen for two reasons. First, because calcium events were not registered in time, transients after the initial peak response were typically lost when averaging traces from multiple worms (Supplementary Figure 2.7A,B). By contrast, the frequency-domain representation separates magnitude and phase information and secondary transients are preserved when averaging over many experiments. Second, this representation allows the identification and separation of signal components in various frequency bands. Low frequencies capture the magnitude of the primary response, high

frequencies capture signal measurement noise, and middle frequencies capture secondary transients.

As an estimate of the portion of the total signal contributed by oscillatory components in a band bounded by two frequencies  $f_{min}$  and  $f_{max}$ , we compute the band power ratio as

$$BPR(f_{min}, f_{max}) = \frac{\sum_{f_{min} \leq f_k \leq f_{max}} |Y(f_k)|^2}{\sum_{f_1 \leq f_k \leq f_{N/2}} |Y(f_k)|^2}$$

The complete time domain trace  $y(t)$  can be exactly reconstructed from its complex Fourier spectrum using the inverse discrete Fourier transform (Matlab function `ifft`), which computes:

$$y(t_j) = \frac{1}{N} \sum_{k=0}^{N-1} Y(f_k) e^{\frac{2\pi i}{N} k j}$$

where  $j = 0 \dots N - 1$ ,  $N = 1,200$ .

To visualize signal contributions from each frequency band, we divided Fourier spectra into three frequency bands, and reconstructed time-domain signals represented by the contributions from a single frequency band using the inverse discrete Fourier transform (equation (3)) of the complex Fourier spectrum clipped to zero everywhere outside of the particular frequency band. Middle band reconstructions are shown in Supplementary Figures 2.61 and 2.9D. By mathematical identity, the sum of the low, middle and high-frequency trace reconstructions equals the full time-domain fluorescence trace. As reconstructions based on sharply clipped samples can result in ringing effects (continued oscillations during a time period when the original trace is not oscillating), we also performed reconstructions using sloped frequency windows. No important changes in the appearance of trace reconstructions during the 30–120-s period were observed (not shown).

The choice of middle frequency band range was made by separating the Fourier spectra into many bands (10 cutoffs, at 0.001, 0.01, 0.02, 0.033, 0.1, 0.2, 0.5, 1, 2 and 5 Hz) and selecting the bands that significantly distinguished wild type from *nlp-1* responses (data not

shown). We found that most *nlp-1* secondary transients are captured in a narrower,  $f = 0.033\text{--}0.2$  Hz band, but *nlp-1* traces also show increased oscillation in the  $f = 0.2\text{--}1$  Hz range; hence, we selected the combination of these bands ( $f = 0.033\text{--}1$  Hz) as the region of interest for Supplementary Figures 2.6 and 2.9D. This frequency range corresponds to periodic oscillations with periods between 1 and 30 s. The different genotypes did not show significant differences in the frequency domains  $<0.033$  Hz or  $>1$  Hz, suggesting little effect on the primary response or signal noise.

Three of the genotypes (*nlp-1*, *npr-11* and *ins-1*) showed strong secondary calcium transients. The *nlp-1* energy spectral density shows a broad peak in frequency-domain amplitude at  $f = 0.0583$  Hz (Figure 2.3D), corresponding to a period of 17 s; this period is similar to the time period between large calcium transients determined by a manual measurement of *nlp-1* traces ( $19.5 \pm 2.2$  s (mean  $\pm$  s.d.); Figure 2.3B). Similarly, *npr-11* and *ins-1* worms show increased amplitude at frequencies corresponding to a period between 10 and 20 s (Figure 2.3F,H and Supplementary Figure 2.9B,D). These transients were not observed during imaging of wild type or *nlp-1* worms during buffer exchange protocols (Supplementary Figure 2.6). All calculations were performed with Matlab.

### 2.9.5 Cell culture and calcium imaging

Two peptides, one corresponding to the NLP-1 sequence (MDANAFRMSFamide) and the second with a scrambled sequence (MSMRFANADFamide), were synthesized by the Proteomics resource center at The Rockefeller University. Human embryonic kidney 293 cells (HEK293) were cultured in DMEM supplemented with 10% FBS at 37 °C in a humidified atmosphere containing 5% CO<sub>2</sub>. Cells 50–60% confluent were transfected with a 1:1 ratio of pME18s-npr-11 and pcDNA3- $\alpha$ 16Z (encoding a promiscuous G protein<sup>13</sup>, a gift from Y.H. Wang) using Lipofectamine 2000 and incubated for at least 24 h; the transient transfection efficiency was  $\sim 70\%$ , estimated by cotransfecting  $\beta$ 2-adrenergic receptor and G $\alpha$ 15 plasmids and counting the fraction of cells responsive to isoproterenol. In control experiments, the

receptor or G protein was transfected alone. Experiments were conducted on three plates for each condition on three different days. The transfected cells were loaded with 2.5  $\mu$ M fura-2/AM for 20 min at 37 °C, peptide solution was applied sequentially to the cells for 15 s with a peristaltic pump, and fluorescence at 510 nm by excitation at 340/380 nm was monitored using a MetaFluor calcium imaging system. The calcium response trace was calculated using all cells in randomly chosen fields. For receptor and G protein transfections, ten fields were analyzed, for G protein alone, seven fields, and for receptor alone, eight fields.

### 2.9.6 Laser ablations

In transgenic worms expressing GCaMP2.2b under an AIA-specific promoter, AWC neurons were identified based on their position and morphology using Nomarski optics, and killed with a Micropoint laser system. Operated worms were tested in parallel with controls from the same strain on the same day.

### 2.9.7 Molecular biology and transgenesis

cDNA or genomic regions corresponding to the entire coding sequences of *nlp-1*, *npr-11* and *ins-1* were amplified by PCR from mRNA or genomic DNA and expressed under cell-specific promoters as indicated. For behavioral experiments in transgenic lines, a splice leader (SL2) fused to a *gfp* transgene was used to confirm cell-specific expression of the gene of interest, and only worms expressing GFP were scored. Selective expression in AWC, ASI, AIA or AIY was achieved using the promoters *odr-3* (AWC>AWB), *str-3* (ASI alone), *gcy-28.d* (AIA) and *ttx-3* (AIY alone). Germline transformations were carried out by microinjection of plasmids at concentrations between 10 and 50 ng  $\mu$ l<sup>-1</sup>. Strains were grown and maintained under standard conditions<sup>50</sup>.

## 2.10 Supplementary Figures

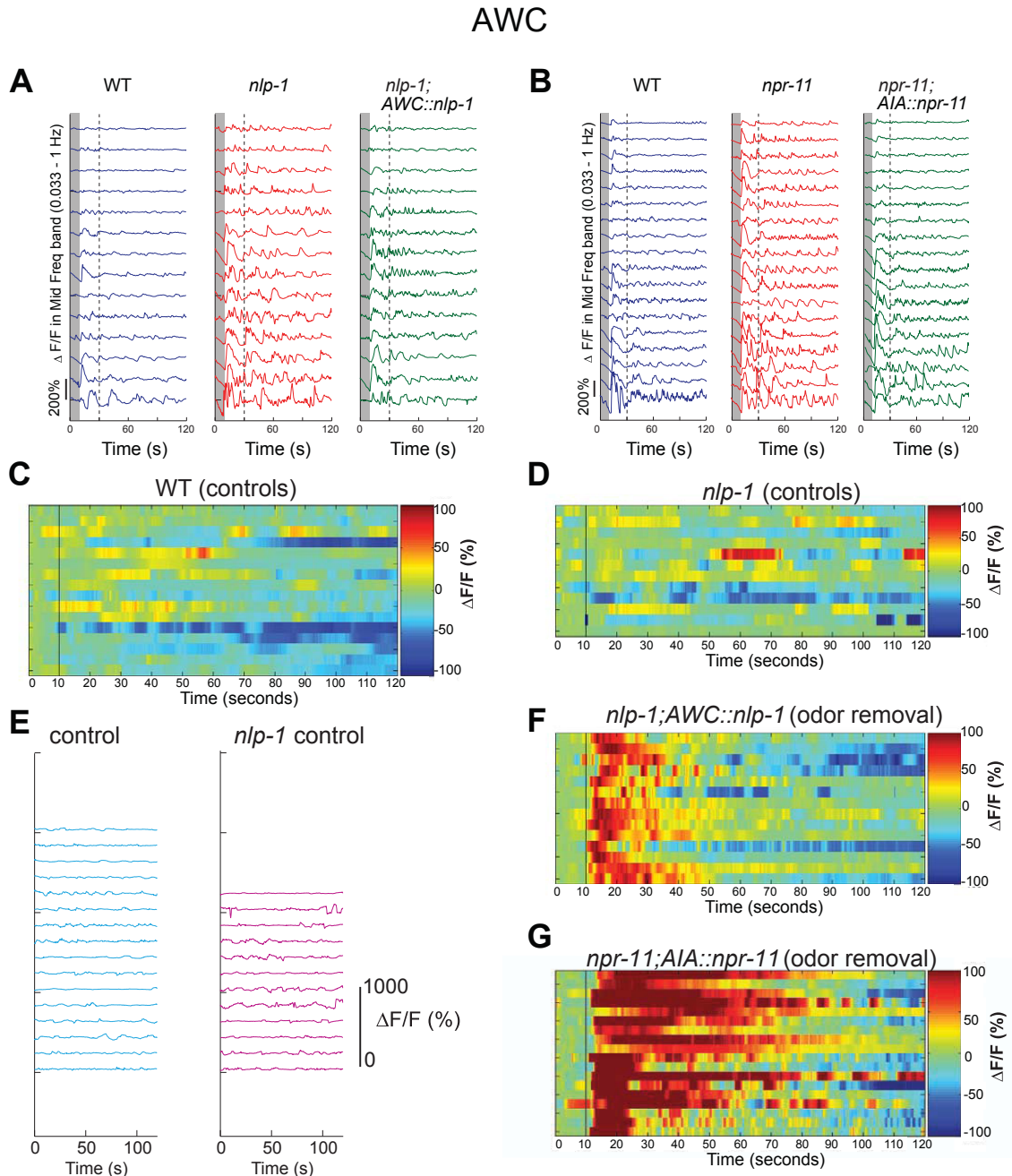


Figure 2.6: AWC calcium responses

(A, B) Individual band reconstructions from the middle frequency band (0.033 Hz -1 Hz) for AWC responses in different genotypes, arranged in order of increasing signaling magnitude. (C, D) Heat maps showing the ratio of change in fluorescence to total fluorescence in AWC neurons expressing GCaMP 1.0, as buffer was exchanged around the nose, (C) wild type ( $n=16$ ) and (D) *nlp-1* ( $n=12$ ). (E) Individual signal reconstructions from the middle frequency band for traces in (C) and (D). Heat maps showing the ratio change in fluorescence to total fluorescence in GCaMP 1.0 expressing AWC neurons when odor was removed from the nose at 10 s in each recording in (F) *nlp-1; AWC::nlp-1* ( $n=14$ ) and (G) *npr-11; AIA::npr-11* ( $n=18$ ).

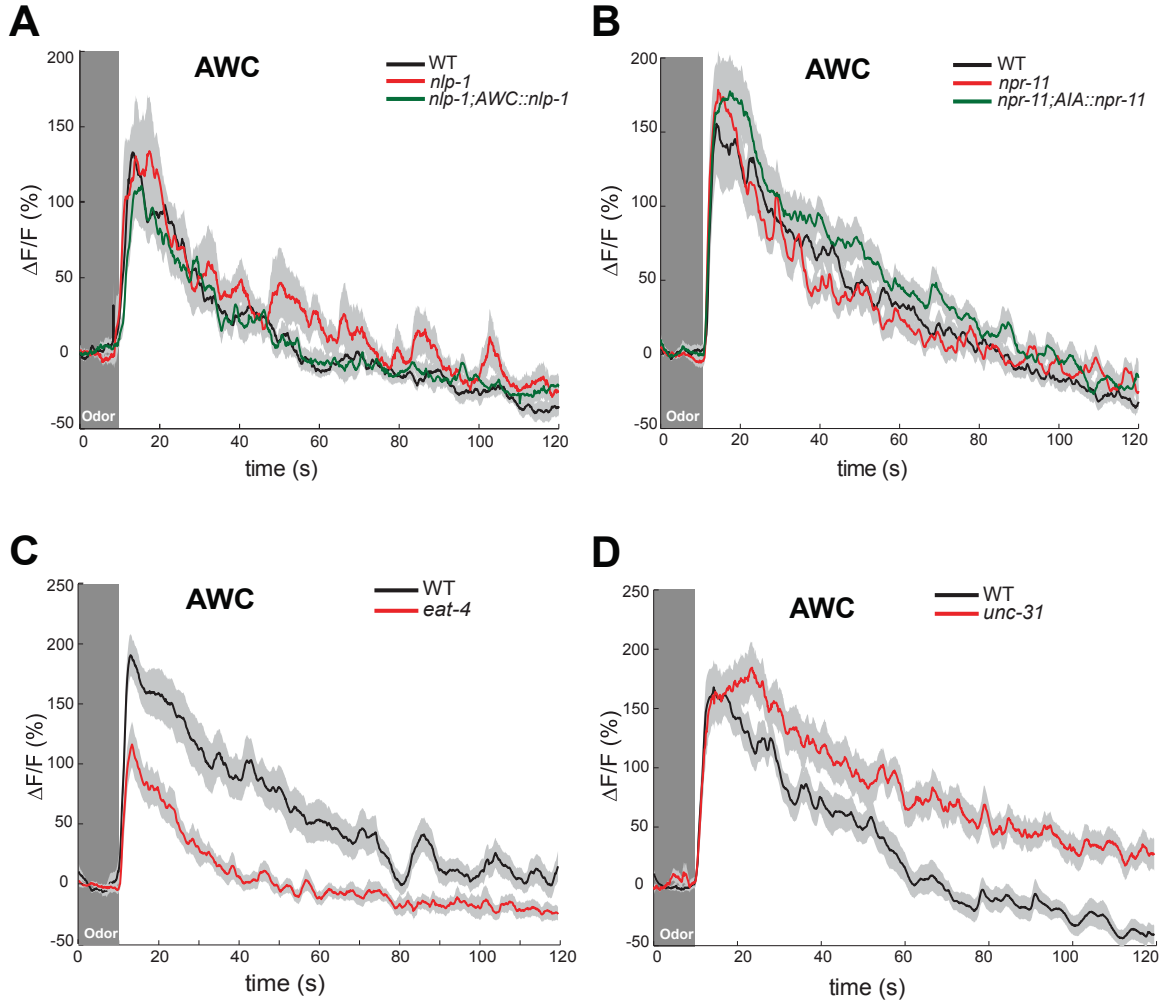


Figure 2.7: AWC calcium responses in neurotransmitter mutants

(A) Average AWC responses to odor removal at  $t = 10$  s in wild-type ( $n=14$ ), *nlp-1* ( $n=14$ ) and *nlp-1;AWC::nlp-1* ( $n=14$ ). (B) Average responses to odor removal at  $t = 10$  s in wild-type ( $n=18$ ), *npr-11* ( $n=18$ ) and *npr-11;AIA::npr-11* ( $n=18$ ). (C) Average responses to odor at  $t = 10$  s in wild-type ( $n=18$ ) and *eat-4* ( $n=18$ ). (D) Average responses to odor removal at  $t = 10$  s in wild-type ( $n=18$ ) and *unc-31* ( $n=18$ ). Dark shade indicates the presence of odor. Light grey shading around each trace is s.e.m.

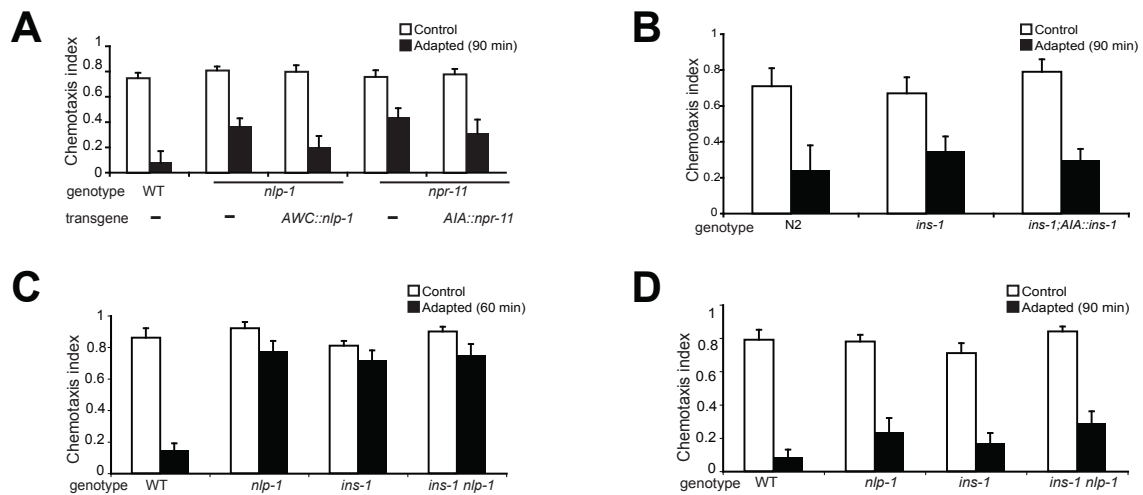


Figure 2.8: Adaptation defects in neuropeptide mutants

Chemotaxis to isoamyl alcohol, with and without prior odor adaptation. (A) *nlp-1*, *npr-11*, and rescued strains (B) *ins-1* and rescued strain (C, D) *ins-1 nlp-1* double mutants. Animals in (A), (B) and (D) were pre-exposed to isoamyl alcohol for 90 min; animals in (C) were pre-exposed for 60 min. Averages and s.e.m. are shown.

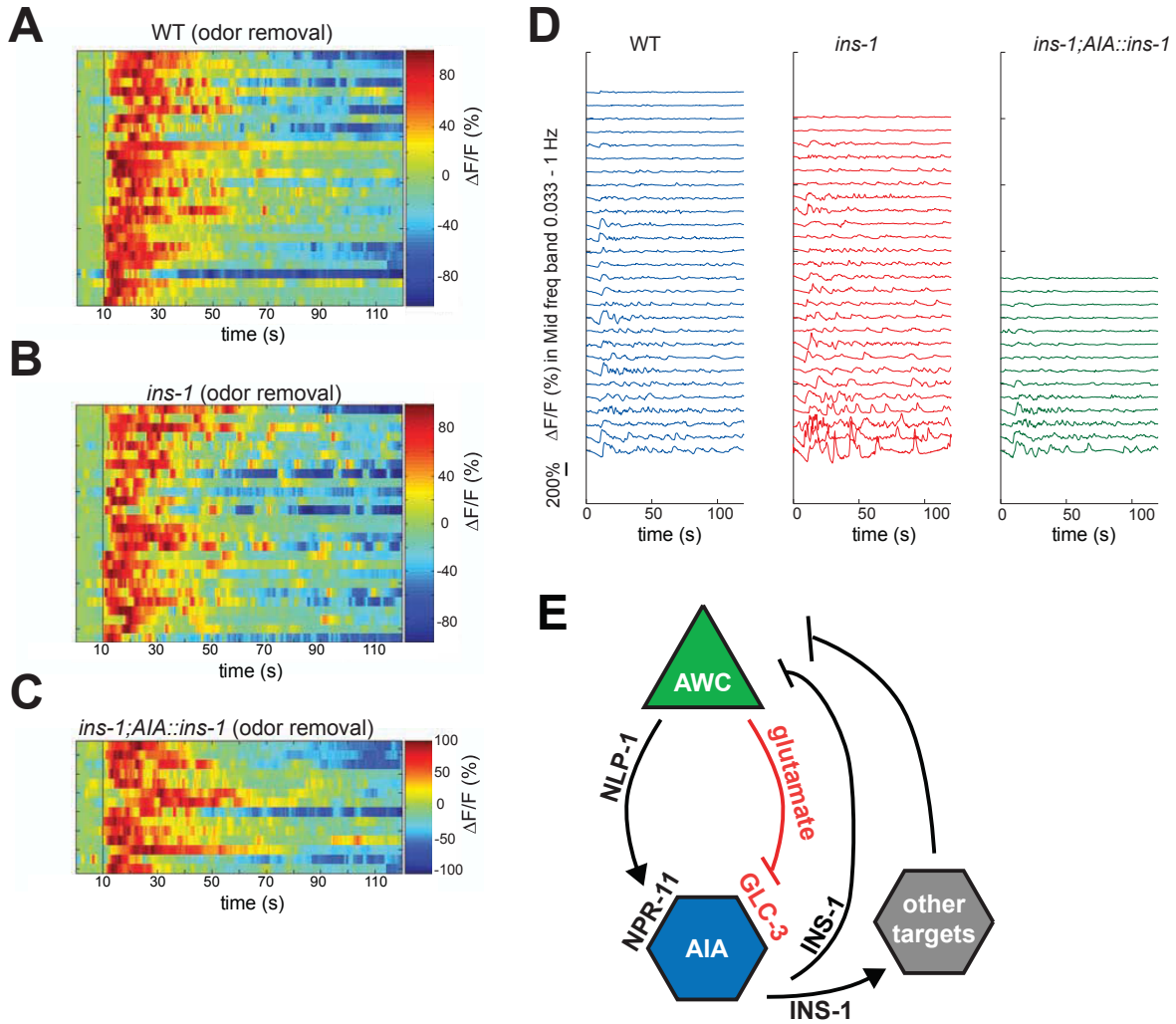


Figure 2.9: *ins-1* mutant AWC responses and band-limited signal reconstructions

Calcium signal heat maps of AWC responses for (A) wild type (B) *ins-1* and (C) *ins-1; AIA::ins-1* genotypes. (D) Individual bandlimited signal reconstructions from the middle frequency band (0.033 Hz – 1 Hz) for AWC responses from wild type (n=28), *ins-1* (n=26) and *ins-1; AIA::ins-1* (n=14) genotypes. The data are plotted with a separation of a 200% change in  $\Delta F/F$  for better visualization. (E) Model of feedback signaling between AWC sensory and AIA interneurons.

# Chapter 3

## Integral and Differential Modeling of AWC and ASH<sup>1</sup>

We now take the plunge into full-blown dynamical systems modeling, using a combination of integral modeling (specifically, L-N models) and differential modeling (low-order ODE systems). One noticeable change from the experiments in the last chapter is the cleanliness of the traces; much of the signal noise in the wild type has been eliminated, primarily due to the use of a paralytic and a newer, higher signal-to-noise indicator, GCaMP3. We also make the move from administering simple step stimuli to more complex, rapidly fluctuating temporal stimuli, allowing us to accurately characterize the response properties of the system on short timescales and build more general system models of temporal processing.

### 3.1 Summary

Natural olfactory behaviors require animals to track fluctuating stimuli over times ranging from milliseconds to hours. To define neural mechanisms that support these computations, we characterized neuronal calcium responses to rapidly fluctuating odor sequences. We found

---

<sup>1</sup>This chapter consists of extracts from a preliminary version of the paper *Temporal multiplexing by biphasic filters in C. elegans chemosensory neurons*, co-authored by Saul Kato, Yifan Xu<sup>†</sup>, Christine E. Cho<sup>†</sup>, L. F. Abbott<sup>‡</sup> and Cornelia I. Bargmann<sup>†</sup>. <sup>†</sup>Howard Hughes Medical Institute, The Rockefeller University, New York, New York, USA. <sup>‡</sup>Department of Neuroscience and Department of Physiology and Cellular Biophysics, Columbia University College of Physicians and Surgeons, New York, New York, USA.

that individual sensory neurons reliably track stimulus fluctuations at timescales relevant to behavior: the AWC olfactory neuron responds to odors with the sub-second precision required for directed chemotaxis, whereas the ASH nociceptive neuron integrates noxious cues over several seconds to reach a threshold for escape behavior. Each neuron’s response to fluctuating stimuli is largely linear, and can be described by a biphasic temporal filter and dynamical model. The model predicts neuronal responses to novel stimuli, describes long-lasting responses to changes in mean stimulus strength, and explains effects of sensory signal transduction mutants. With modified parameters, the model captures the different calcium response properties of additional *C. elegans* sensory neurons. Biphasic filters of this form represent a general strategy for encoding sensory information on multiple timescales.

## 3.2 Introduction

Olfactory, gustatory, and pheromone cues provide essential information about an animal’s environment. Because these cues are chemically diverse, most studies of the chemical senses ask how animals detect and distinguish the chemical quality of a stimulus. However, the temporal properties of stimuli are also important in guiding behavior. The time history of a stimulus as an animal monitors and moves through its environment can convey information about the distribution of food, mates, competitors, and predators. Accordingly, the olfactory system should detect temporal features of chemical stimuli, just as neurons in the visual and auditory systems are tuned to temporal features of stimuli (DeAngelis et al., 1995; Calabrese et al., 2011).

In the worm, chemosensation and chemosensory behaviors can be functionally mapped to individual neurons, a unique advantage for dissecting the coding of odor quality and dynamics. A few dozen chemosensory neurons regulate virtually every aspect of the behavior and life history of *C. elegans* (Bargmann, 2006a). Each sensory neuron detects particular environmental chemicals through its cell type-specific repertoire of G protein-coupled receptors and signaling molecules. Each sensory neuron then controls characteristic behav-

iors such as chemotaxis, avoidance, aggregation, or exploration. These behaviors require the integration of chemical cues over a range of timescales. For example, during gradient climbing animals track odor concentration changes within 2 seconds to regulate their head orientation, but they also track concentration changes over 20-90 seconds to regulate turning frequency (Pierce-Shimomura et al., 1999; Iino and Yoshida, 2009; Izquierdo and Lockery, 2010; Albrecht and Bargmann, 2011). In avoidance behaviors, animals reverse immediately to a strong noxious stimulus, but integrate weak noxious stimuli over  $\sim 10$  seconds (Chao et al., 2004). For foraging, animals evaluate environmental quality over tens of minutes (Gray et al., 2005).

Sensory neurons are tuned to chemical quality by their receptor gene expression, but little is known about how they are tuned to temporal information. Direct examination of chemosensory signaling using genetically-encoded calcium indicators has shown that *C. elegans* sensory neurons respond to relevant chemical stimuli with a slow calcium transient that rises for several seconds and decays partially or completely over  $\sim 60$ s of stimulus presentation (Hilliard et al., 2005; Chalasani et al., 2007; Suzuki et al., 2008; Zimmer et al., 2009; Busch et al., 2012). The stronger initial activity and weaker tonic activity of sensory neurons correlates with these neurons' ability to trigger both immediate and prolonged behavioral responses (Chalasani et al., 2007; Zimmer et al., 2009; Busch et al., 2012), but beyond that, the nature of temporal encoding is a mystery.

Here, we develop methods to present rapidly fluctuating chemical stimuli to *C. elegans*, and use them to characterize temporal coding in two classes of *C. elegans* chemosensory neurons: AWC neurons that sense attractive odorants and ASH neurons that sense noxious chemical and mechanical stimuli. We show that these neurons respond reliably and robustly to rapidly fluctuating stimuli at speeds that are well-matched to the behavioral functions they support. Applying system identification methods that have been employed in other sensory systems (Dayan and Abbott, 2001; Westwick and Kearney, 2003), we analyze fluorescence signals to define linear temporal filters that describe the calcium responses of each neuron.

To determine the intrinsic neuronal filters, we use analytical methods to correct for the effects of the genetically encoded calcium indicator. The filters of both neurons can be modeled by a system of three first-order differential equations, and predict responses to patterns of stimuli not used in their construction. Sensory signal transduction mutations affect specific components of the filters. With simple parameter changes, the model can fit the responses of other sensory neurons, suggesting that neurons with diverse response properties may share general strategies for encoding stimulus dynamics and history.

### 3.3 Reliable responses to rapid stimulus fluctuations

We developed and validated a system for rapid odor delivery by adapting a microfluidic imaging chip previously used to deliver step stimuli (Chronis et al., 2007). In this chip, sensory cues are delivered in a liquid environment, which increases the speed and reliability of odor delivery and removal; *C. elegans* responds normally to chemical stimuli in all-liquid environments (Luo et al., 2008; Albrecht and Bargmann, 2011). Chemical stimuli were delivered by switching between two laminar fluid streams that flowed across the nose of an adult hermaphrodite confined in the microfluidic chip (Figure 3.7A,B). Control experiments with fluorescein dye in the stimulus stream showed that the system could reliably deliver sequences of ON/OFF pulses at frequencies of up to 5 Hz (Figure S3.7C). To accurately model the input-output transformation given the  $\sim 30$  ms variability in switching time of the delivery system, fluorescein dye was included in the stimulus stream, and its intensity near the animal’s nose was used as a surrogate for odor concentration during recordings (Figure 3.7D).

The activity of *C. elegans* sensory neurons was monitored using the genetically encoded calcium indicator GCaMP3 (Tian et al., 2009), which has high sensitivity (660 nM apparent affinity), a  $\sim 10$ -fold dynamic range, and rapid dynamics (52 ms  $t_{1/2}$  rise time, 384 ms  $t_{1/2}$  decay time). Calcium imaging misses the fastest elements of the neuronal response (Geffeney et al., 2011), but in other respects it is well-suited to *C. elegans* neurons, which typically

have graded responses, lack sodium-based action potentials, and use voltage-gated calcium channels to amplify neuronal inputs and regulate neurotransmitter release (Goodman et al., 1998; Liu et al., 2009). We observed similar GCaMP3 signals in cell bodies and axons of AWC and ASH, suggesting that the observed response correlates with the presynaptic calcium that regulates neurotransmission.

AWC olfactory neurons are inhibited by attractive odors and activated by their removal (Chalasani et al., 2007). Removing the attractive odor isoamyl alcohol after a five-minute exposure results in a calcium increase in AWC, the OFF response, that peaks within 5 s and decays to a steady-state level over 30-60 s (Figure 3.1A). To ask whether AWC could track rapid odor fluctuations, we began with the same five-minute odor pulse, but alternated between 1 s pulses of odor and buffer instead of removing the odor entirely. AWC responded to this flickering stimulus with regular, sustained calcium oscillations at 1 Hz superimposed on the slowly decaying OFF response (Figure 3.1B). The oscillating response continued after the OFF response reached a steady state (Figure 3.1B, inset), but stopped immediately when stimulus oscillations ceased.

ASH nociceptive neurons respond to noxious chemicals and touch with an increase in calcium, the ON response (Hilliard et al., 2005). The ASH calcium response to a high-osmolarity 1 M glycerol step stimulus peaks within 10 s and decays to a steady-state level in 60 s (Figure 3.1C). Replacing the glycerol step stimulus with a flickering 1 s stimulus resulted in regular oscillations of the calcium signal at 1 Hz superimposed on the ON response (Figure 3.1D). The oscillating responses persisted after the decay of the initial ON response (Figure 3.1D, inset). These results reveal a new property of the AWC and ASH neurons: the ability to track flickering stimuli at a sub-second resolution.

To characterize the temporal features of the AWC and ASH responses more precisely, we used a system identification approach that constructs phenomenological models from neuronal responses to randomly fluctuating stimuli. To approximate a spectrally unbiased stimulus pattern, transitions between full and zero odor concentration were controlled by

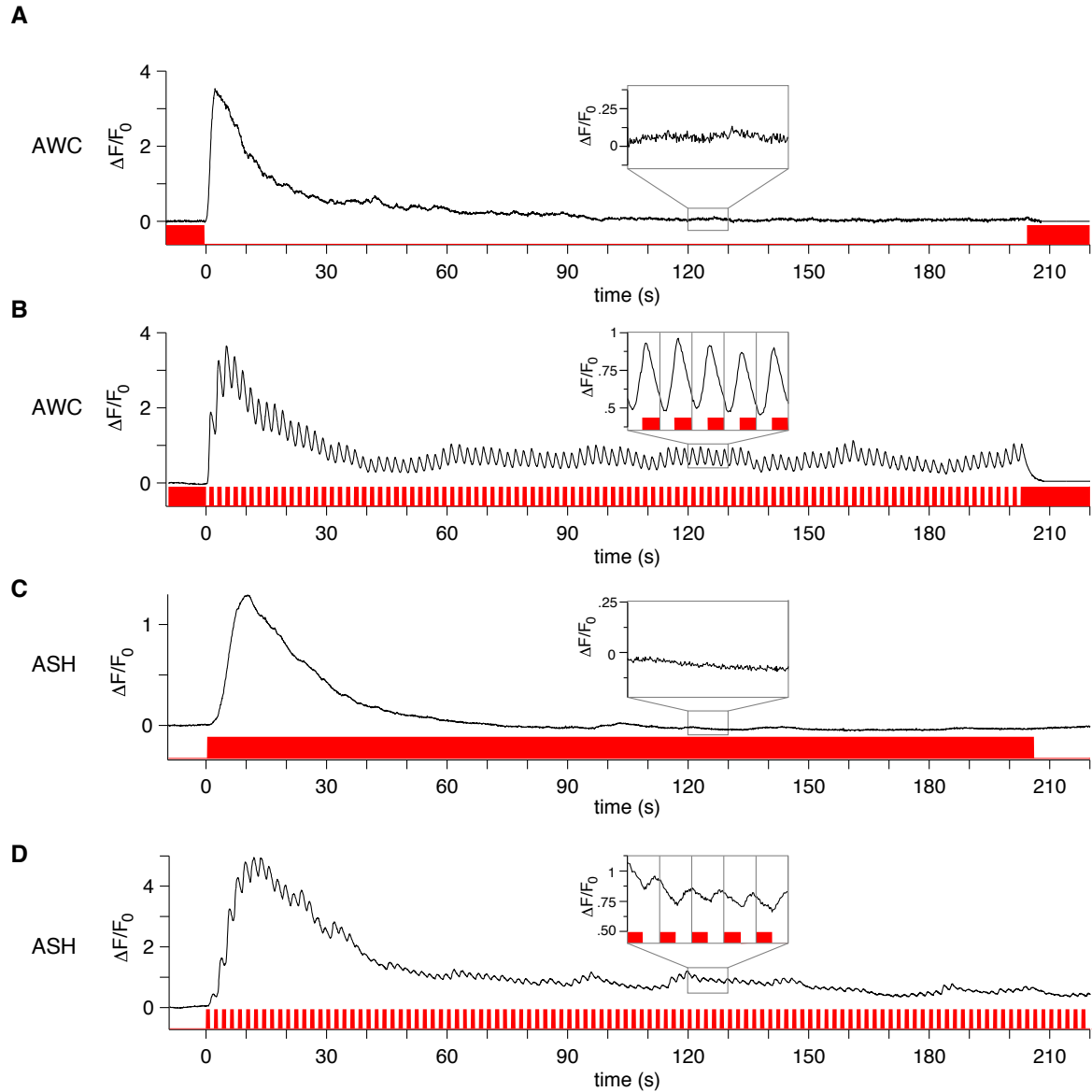


Figure 3.1: AWC and ASH track flickering odor stimuli.

Representative GCaMP3 responses (black) to stimulus input sequences (red). (A and B) AWC responses after a five minute pre-exposure to  $9.2 \times 10^{-4}$  M isoamyl alcohol, followed by (A) odor removal, and (B) a flickering on/off isoamyl alcohol stimulus with a 1 s pulse length, fluctuating between the original concentration and zero. (C and D) ASH responses. (C) 1 M glycerol stimulus and (D) A flickering on/off 1 M glycerol stimulus with a 1 s pulse length. Insets, zoomed views of 10s intervals after the response reaches steady-state, stimulus in red. Gray vertical lines divide the inset graphs into 2 s epochs aligned to stimulus transitions.

a fixed pseudo-random m-sequence (Figure 3.2A,B, 3.7D, Experimental Procedures), which has a sharply peaked autocorrelation similar to that of an infinite-length random sequence. Both AWC and ASH responded to the m-sequence stimuli with a fluctuating calcium signal superimposed on the slowly decaying response to stimulus onset or offset (Figure 3.2A,B). These rapid responses continued for several minutes after the initial ON or OFF response reached steady state.

AWC and ASH calcium responses to a fixed m-sequence stimulus were strikingly stereotyped across different animals and across trials for a given animal (Figure 3.2C,D, Experimental Procedures, and data not shown). The use of the same particular temporal sequence for both neurons permitted a direct comparison between them. Their overall peaks of activity were similar, but AWC responses had a finer temporal resolution than ASH (Figure 3.2). Thus, in addition to their known ON and OFF responses to step stimuli, both AWC and ASH neurons can reliably track more rapid, complex stimulus fluctuations, but with slightly different properties.

### 3.4 Linear temporal filters describing AWC and ASH sensory neurons

The steady-state responses to m-sequence stimuli provided a basis for modeling the input-output transformations of AWC and ASH neurons as linear-nonlinear (L-N) cascades, a standard procedure for describing sensory-driven responses (Dayan and Abbott, 2001; Westwick and Kearney, 2003). In this approach, the input-output transformation is broken down into two operations on the input stream: convolution with a linear temporal filter followed by the application of a static nonlinearity (Figure 3.8A). The linear filter  $K(\tau)$  accounts for the contribution of the stimulus at time  $t - \tau$  to the fluorescence response at time  $t$ , with  $\tau$  defined as the lag. The static nonlinearity  $F(x)$  describes how this filtered response,  $x$ , is converted into the measured fluorescence change. Both  $K$  and  $F$  were extracted from the data by standard techniques (Experimental Procedures). Contributions of GCaMP3 calcium

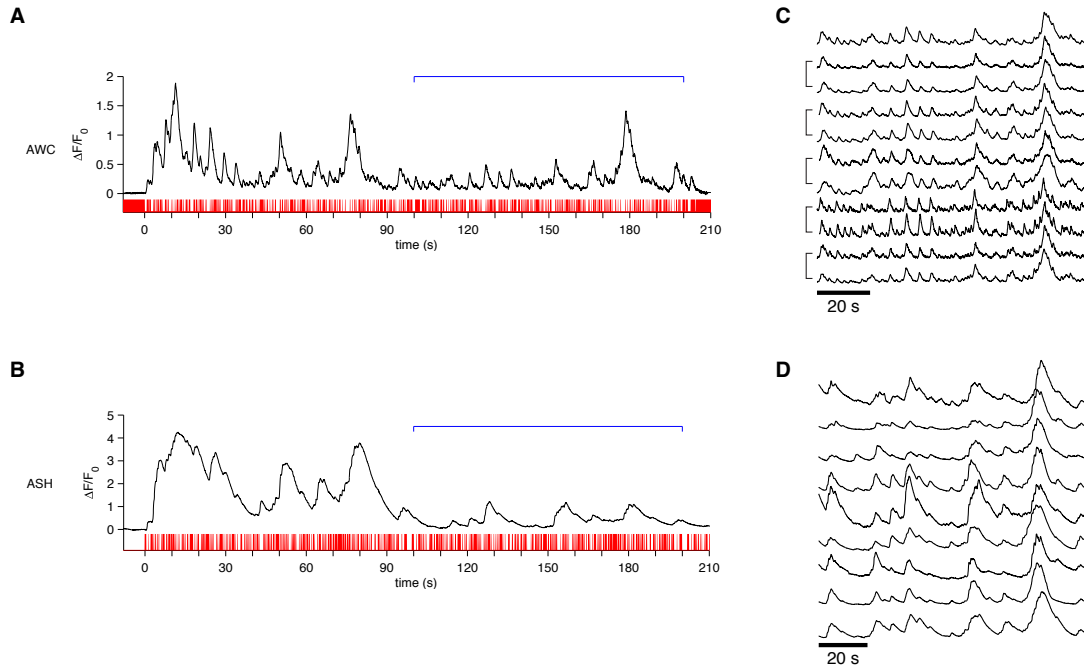


Figure 3.2: AWC and ASH respond reliably to complex odor patterns

(A) Representative AWC response to a pseudo-random on/off sequence of  $9.2 \times 10^{-4}$  M isoamyl alcohol (pulse length 200 ms, 9-bit sequence, two repetitions), following a five minute pre-exposure to  $9.2 \times 10^{-4}$  M isoamyl alcohol. Bracket marks the second repetition of the m-sequence, the region shown for additional AWC neurons in (C) and used to construct and analyze the L-N model. (B) Representative ASH response to pseudo-random off/on pseudo-random pattern of 1 M glycerol (pulse length 200 ms, 9-bit sequence, two repetitions). Bracket marks the second repetition of the m-sequence, the region shown for additional ASH neurons in (D) and used to construct and analyze the L-N model. (A) and (B) are similar m-sequence stimulus input patterns but with inverted sign; note the similar overall shape of the AWC and ASH neuronal responses but the sharper temporal resolution in AWC traces. (C) Responses of additional AWC neurons to the same m-sequence as in (A). Brackets indicate two trials of a single animal, separated by  $\sim 10$  minutes. Individual traces were normalized to the peak magnitude within each trace. (D) Responses of additional ASH neurons to the same m-sequence as in (B). Each trace represents a different animal. Individual traces were normalized to the peak magnitude within each trace.

binding and kinetics to this signal will be addressed later.

Analysis was performed on neuronal responses in the time period after they settled into a quasi-steady state (Figure 3.2A,B, brackets). We extracted linear filters for AWC and ASH from single trials (gray traces in Figure 3.3A) and from trial-averaged data (black traces in Figure 3.3A). The similarity of linear filters extracted from single neurons echoed the striking reliability observed in neuronal calcium traces (Figure 3.2C,D). The trial-averaged linear filter for AWC has an initial component that peaks rapidly at 0.9 s and decays with a  $t_{1/2}$  of 1.5 s ( $n=11$ , range  $t_{peak}= 0.6 - 1.15$  s,  $t_{1/2} = 0.8 - 2.1$  s) (Figure 3.3A). The AWC filter is indicated as negative (an inverting filter) to reflect the fact that AWC activity decreases as isoamyl alcohol concentrations increase. The linear filter for ASH is shown with the opposite sign to that of AWC, to reflect the fact that ASH activity increases when glycerol increases. The trial-averaged linear filter for ASH has an initial component that peaks at 3.4 s and decays with a  $t_{1/2}$  of 4.3 s ( $n=13$ ,  $t_{peak}= 2.9 - 3.6$  s,  $t_{1/2} = 2.8 - 6.1$  s) (Figure 3.3A). Close inspection of AWC and ASH filters after 10-12 s suggested the existence of a smaller, slower component with an inverted sign; modeling and responses to step stimuli described below support the existence of these slow components.

AWC and ASH each yielded a similar, characteristic linear filter in response to a second m-sequence with a different detailed structure (Figure 3.3B, Figure 3.9B), indicating that the filters are robust to different particular temporal patterns within this class of fluctuating stimuli. Similar filters were observed in animals whose GCaMP3 expression levels varied by  $\sim 5$  fold (data not shown), and in an AWC strain expressing a different calcium indicator, GCaMP5 (Figure 3.3B). These results suggest that the temporal filter is robust to the specific reporter protein, protein level, or strain.

Neuronal tuning can be altered by stimulus intensity: for example, avian auditory neurons can be more frequency selective or temporally selective at high sound intensities (Nagel and Doupe, 2008). The effects of stimulus intensity on temporal features of AWC and ASH were explored by varying stimulus concentrations while maintaining the temporal properties of

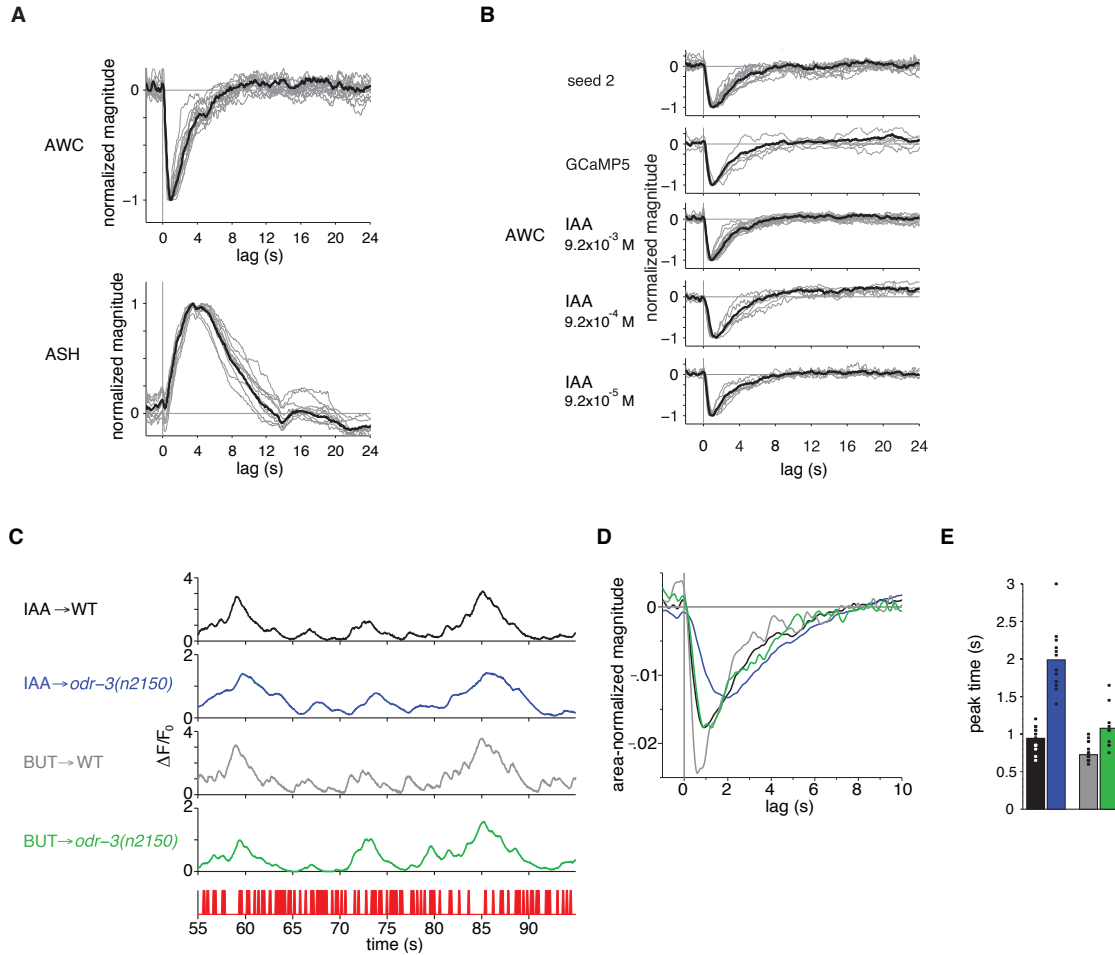


Figure 3.3: Linear filters capture the dynamics of AWC and ASH responses

(A) Linear filters inferred from individual input-output records for AWC and ASH neurons (gray) and from trial-averaged input-output records (black). (B) The AWC linear filter is robust to odor concentration, GCaMP indicator, and m-sequence design. For related analysis of ASH filters, see Figure 3.9. (C) Segment of wild-type and *odr-3(n2150)* responses to m-sequence of  $9.2 \times 10^{-4}$  M isoamyl alcohol (IAA) and  $1.11 \times 10^{-5}$  M butanone (BUT). The pseudo-random stimulus sequence is shown at bottom in red. Note the coarser temporal resolution of the *odr-3* IAA response, suggesting that this neuron does not follow stimuli as quickly. (D) Trial-averaged AWC linear filters for wild type and *odr-3(n2150)* responses to IAA and BUT, normalized to area under the first phase of the filter. Colors match traces in (C). (E) Peak times of individual trial filters for wild type and *odr-3(n2150)* responses to IAA and BUT. Colors match traces in (C). Peak times corrected for GCaMP kinetics are shown in Figure 3.9D. For C-E,  $n=14$  for IAA-wt,  $n=12$  for IAA-*odr-3(n2150)*,  $n=27$  for BUT-wt,  $n=11$  for BUT-*odr-3(n2150)*. In E, WT IAA differs from BUT ( $P < 0.001$ ), WT IAA differs from *odr-3* IAA ( $P < 0.001$ ), and WT BT differs from *odr-3* BUT ( $P = 0.0013$ ) by Welch's two-tailed t-test.

the stimulus. AWC responded reliably to the m-sequence of isoamyl alcohol over a 100-fold range of concentrations, in each case yielding the same temporal filter (Figure 3.3B). ASH responses to osmotic glycerol stimuli were observed over an 8-fold concentration range, in each case yielding similar temporal filters (Figure 3.9B). These results suggest that temporal filtering in AWC and ASH is independent of stimulus intensity across a relatively broad range.

The analysis described above implies that AWC can process isoamyl alcohol fluctuations in less than a second, much more rapidly than was expected from previous calcium imaging experiments. To determine whether AWC response properties generalize across odors, we examined the odorant butanone, which is sensed by AWC but has genetic and behavioral requirements that indicate that it is detected through different receptor(s) than isoamyl alcohol (Bargmann, 2006a; Wes and Bargmann, 2001). AWC responds strongly and reliably to an m-sequence of butanone (Figure 3.3C), yielding an average linear filter for butanone responses that was at least as fast as the average filter for isoamyl alcohol (Figure 3.3D,E). This similarity suggests that rapid linear sensory processing may be a general feature of AWC.

Insight into the rate-determining molecules for the AWC filter came from the analysis of a G protein alpha subunit mutant, *odr-3* (Roayaie et al., 1998). A heterotrimeric G protein that contains ODR-3 is localized to AWC and ASH sensory cilia, where it acts in sensory transduction downstream from chemosensory G protein-coupled receptors (Figure 3.9A). *odr-3* mutants are partially defective in their ability to chemotax to isoamyl alcohol, showing a reduced accumulation index on an agar plate, but retain the ability to chemotax to butanone (Roayaie et al., 1998). When challenged with rapid odor fluctuations, *odr-3* mutants showed reliable AWC responses to both isoamyl alcohol and butanone (Figure 3.3C). However, the *odr-3* isoamyl alcohol filter was two-fold slower than the wild type, peaking at 2 s (Figure 3.3D,E). This result suggests that an ODR-3-containing G protein is required in the rate-limiting process for rapid AWC responses to isoamyl alcohol. The *odr-3* butanone filter

was less affected, resembling the wild-type isoamyl alcohol filter (Figure 3.3D,E). The more subtle effect of *odr-3* on rapid butanone responses matches its more subtle effect on butanone chemotaxis.

### 3.5 An ODE model for sensory filters

To gain further insight into the possible mechanisms of sensory encoding, we developed a model based on ordinary differential equations (ODEs) that reproduces the phenomenological filters we observed. Both the AWC and ASH filters were best described by two components with different temporal widths, a feature that is not achievable with two first-order ODEs. Therefore, we developed a model for the AWC and ASH linear filters consisting of a system of three first-order linear ordinary differential equations, the “ODE model” (Figure 3.4B, Experimental Procedures). After parameter optimization, the sensory filters given by this model closely matched the trial-averaged filters extracted from the data (Figure 3.4C). The model consists of two parallel feedforward paths with fast and slow dynamics (F and S).

The ODE model describes the sensory filters in terms of three exponential functions, one representing the response latency and the others the durations of shorter and longer time components of opposite sign (Figure 3.4B,D). The relative timescales of these two components are primarily set by the relaxation time constants  $1/k_f$  and  $1/k_s$  of the parallel path variables, and their relative strengths are set by the interaction rate constants  $k_{af}$  and  $k_{as}$  (Figure 3.4B, Table S1).

The linear filters extracted directly from input-output records reflect the response properties of the neurons as well as the dynamics of the conversion of intracellular calcium levels into fluorescence signals by the GCaMP indicator (Figure 3.4A). To estimate the intrinsic neuronal filters, which are not directly observable, we modeled the effects of GCaMP as an L-N cascade that captures the known calcium binding and unbinding properties of GCaMP3 (Tian et al., 2009) (Experimental Procedures), and then deconvolved the observed sensory filter with the linear GCaMP element. In doing this, it was important to use the analytically

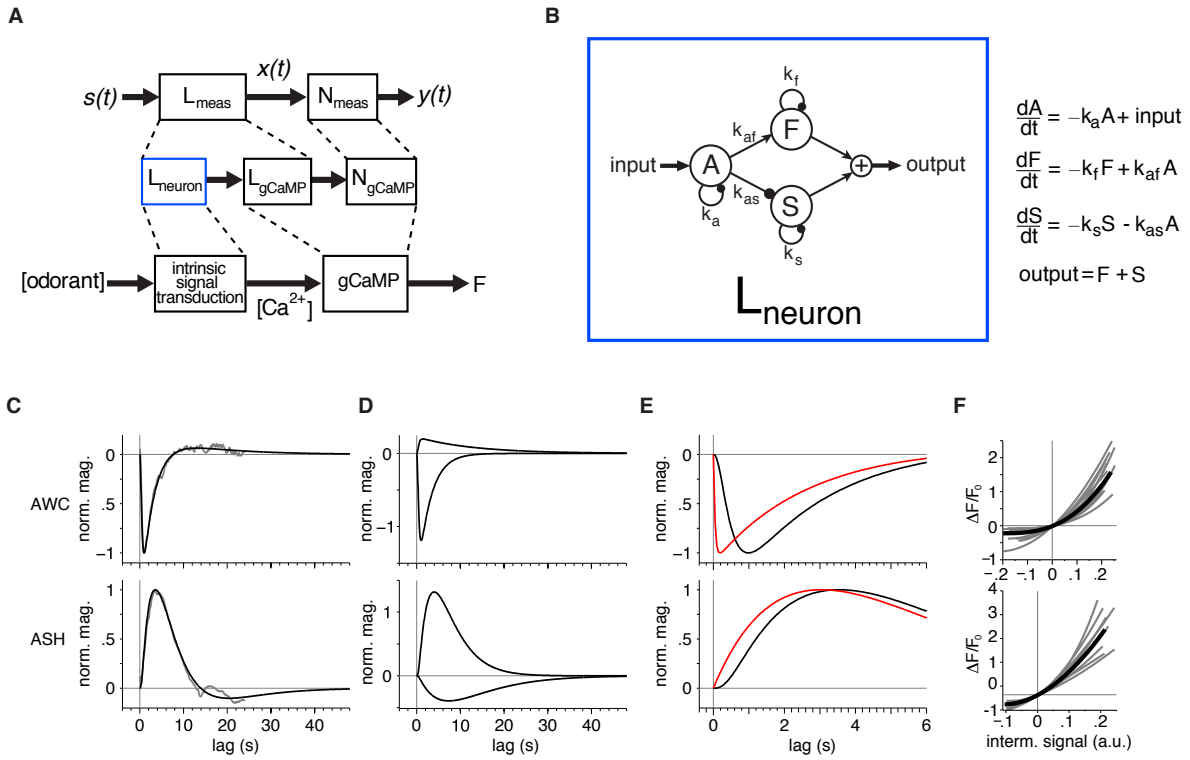


Figure 3.4: A three-variable ODE model produces a biphasic filter with two timescales

(A) Schematic of the overall linear-nonlinear model and putative mapping to elements of the signaling-to-GCaMP transformation.  $L_{meas}$  is a convolution of the intrinsic neuronal filter  $L_{neuron}$  and the GCaMP filter  $L_{GCaMP}$ , and the nonlinearity  $N_{meas}$  probably arises predominantly from the GCaMP nonlinearity  $N_{GCaMP}$ . (B) Diagram and equations of a three-variable ODE model that produces a biphasic filter with distinct timescales for each phase, corresponding to the  $L_{neuron}$  operator in (A). (C) Overall ODE model filter (in black) fit to the filter extracted from trial-averaged input-output records (in gray) for AWC and ASH. Technical issues limited the maximum lag of the estimated filters to 24 s, but the ODE model filters are extrapolated to 48 s. (D) Decomposition of ODE model filter into fast and slow components corresponding to transformations between the input and outputs of variable  $F$  and  $S$  in (B). The sum of these component filters produces the full ODE filter in (C). (E) In black, the first six seconds of overall model filters for AWC and ASH. In red, the intrinsic neuronal filter  $L_{neuron}$  analytically deconvolved from the overall filter  $L_{meas}$  to remove the dynamical effect of GCaMP3 (Tian et al., 2009). (F) Normalized power-law nonlinearities for AWC and ASH obtained from individual input-output records (gray) and from trial-averaged input-output records (black).

smooth filters described by the ODE model, because the required deconvolution amplifies high-frequency noise in sampled data, whereas the deconvolution of the ODE model filter can be done exactly (Experimental Procedures). The results of this deconvolution suggested that the intrinsic AWC filter peaks very rapidly: the first component peaks within 0.25 s of stimulus onset (Figure 3.4E). Similar calculations suggested that the intrinsic ASH filter peaks at 2.9 s (Figure 3.4E).

### 3.6 The static nonlinearity matches properties of GCaMP3

The next step in the system identification approach is determining the nonlinearity that converts the filtered signal into the observed fluorescence changes (Figure 3.4A). Both the AWC and ASH traces yielded a consistent, monotonic relationship between the signal generated by the linear filter and the observed neuronal response (Figure 3.4F, 3.8B-E, 3.9B). This nonlinear relationship did not saturate, and appeared concave throughout its range (Figure 3.4F, 3.9B). The mean exponent of a power-law function fit to this nonlinearity is 2.3 for AWC and 1.8 for ASH (Experimental Procedures, Figure 3.8B-E). These values are similar to the Hill coefficient of 2.3 describing the cooperative dependence of GCaMP3 fluorescence intensity on calcium binding (Tian et al., 2009). This match suggests that a substantial component of the observed nonlinear response function is due to the calcium-to-fluorescence transformation of GCaMP3. In turn, this implies that the intrinsic calcium responses of AWC and ASH are close to linear over the tested range.

### 3.7 L-N models accurately predict neuronal responses

The empirically derived temporal filters (Figure 3.3A) and the filters described by the ODE model (Figure 3.4C) were validated by using them to predict neuronal responses to experimental stimuli. We did this in three different ways for both types of filters: fitting individual trials, fitting to trial-averaged results, and using a cross-validation procedure in which different trials were used for extracting and testing the filters. First, for each individual recording,

we derived an individual L-N model for the neuronal output (grey traces in Figure 3.3A), and used this model to generate a simulated response. Second, for each individual recording, we used the trial-averaged L-N model for AWC or ASH (black traces in Figure 3.3A) to generate a simulated response. In all cases the simulation closely matched the true neuronal response (Figure 3.5A,B), suggesting that the neuronal input-output transformation is well characterized by the L-N model. Individual L-N models accounted for 70-98% of the response variance for each neuron, and trial-averaged L-N models accounted for 62-97% of the response variance, indicating that trial-by-trial fitting was not required for good model predictions (Figure 3.5B). Third, we cross-validated the trial-averaged L-N models on an independent set of trials that were not used for filter estimation. The trial-averaged filters accounted for 69-95% of the response variance for each neuron in the validation set, the same accuracy as for the original data (Figure 3.5B). These results compare favorably to L-N model fitting in other experimental systems.

The ODE filter model is described by seven free parameters, four describing the normalized linear temporal response and three describing the (GCaMP) power law nonlinearity. Using the same approach described above, we derived a model for each individual trace and the trial-averaged trace, and used these models to simulate responses to inputs. The average variance accounted for by the ODE filters for each neuron was 69-98% (individualized model) or 61-96% (trial-averaged model) (Figure 3.5B). The ODE model generated from trial-averaged data performed equally well at explaining variance when cross-validated with independent experimental trials (Figure 3.5B). The success of these ODE models indicates that the good performance of the empirically derived filters for the L-N models did not arise from overfitting.

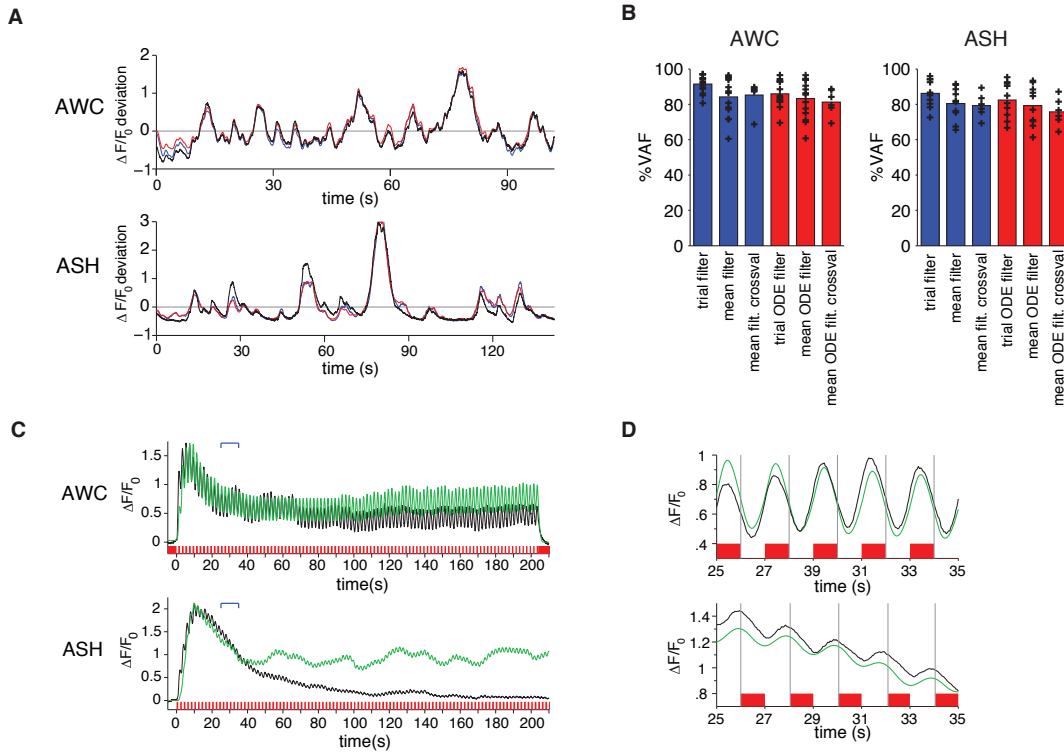


Figure 3.5: Performance and prediction of the L-N models.

(A) Actual (black) and simulated (red, blue) responses of representative AWC and ASH neurons to fluctuating stimuli. Simulations used a full-parameter L-N model with filters estimated from trial averaged input-output records (blue) or the ODE filter model (red). (B) Performance (% variance accounted for) of simulating individual trial responses using: (1) full-parameter L-N models estimated from individual trials (2) an L-N model estimated from trial-averaged input-output records, (3) a trial-averaged L-N model applied to a cross validation set, (4) an ODE filter L-N model estimated from individual trials, (5) an ODE filter L-N model estimated from trial-averaged input-output records, and (6) an ODE filter L-N model estimated from trial-averaged input-output records applied to a cross validation set. Bars indicate average performance.  $n=14$  for AWC,  $n=10$  for ASH, and  $n=7$  for both cross validation sets. (C) In green, simulated responses to trial-averaged 1 s ON/OFF square pulse input records using the mean ODE filter L-N model for AWC and ASH. Actual trial-averaged output records are in black ( $n=12$  for each neuron). Brackets indicate time period excerpted in (D). (D) Excerpt of predicted (green) and actual (black) responses in (C) from 25-35 seconds. Gray vertical lines divide the inset graphs into 2 s epochs aligned to stimulus transitions.

### 3.8 The ODE models predict many features of AWC and ASH responses

Even though our LN-ODE models were constructed from m-sequence data, they should describe responses to other types of stimuli as well. To test their generality, we returned to the 1 s flicker stimulus and used the LN-ODE model to simulate the entire time course of the calcium response in AWC and ASH neurons (Figure 3.5C,D), using the measured trial-averaged input stimulus from 1 s flicker trials as input (Figure 3.1B,D). The model accurately predicts the magnitude and phase of both AWC and ASH responses to 1 s flickers, showing a larger magnitude oscillatory response in AWC than in ASH and a distinct phase lag (Figure 3.5D).

Remarkably, the simulated traces also provide a good description of the initial OFF and ON responses in AWC and ASH (Figure 3.5C), even though the models were constructed solely from data taken during the later steady-state period of the response. The model predictions are fairly accurate for the first 40 s (ASH) to 60 s (AWC) of the response and then describe the response oscillations due to the flicker, but for both neurons they overestimate the baseline level of the steady-state response (Figure 3.5C). This discrepancy is likely due to additional adaptation mechanisms that are not accounted for by the LN-ODE model; multiple adaptation mechanisms are a common feature of sensory responses (e.g. Fairhall et al., 2001). In addition, the model underestimates the initial slope ( $<5$ s) of the OFF and ON responses for both AWC and ASH. These two discrepancies may be related, because sensory responses are larger and faster before adaptation.

The fact that the LN-ODE model can describe the large initial responses to stimulus offset or onset, the timing of the response peak, the decay of the response, and the sustained response fluctuations (Figure 3.5C) suggest that similar mechanisms drive both rapid and sustained responses in AWC and ASH. The success of the models is due to the biphasic structure of their linear filters, with components of different sign and width. The initial

OFF or ON response is mainly determined by the fast component (component F in Figure 3.4B), and the delayed decay by the slower second component of opposite sign (component S).

### 3.9 A calcium channel mutant provides mechanistic insight into the biphasic model

The relationship between the models and underlying molecules was probed by analyzing signaling mutants that affect ASH neurons. ASH detects repellents through unknown receptors that activate several heterotrimeric G proteins, which in turn regulate channels of the TRPV family, whose opening secondarily activates the voltage-gated calcium channel EGL-19 (Figure 3.9A). In general, sensory transduction genes required for ASH behavioral responses are required both for the calcium transients to long (10 s) stimuli, and for ASH tracking of flickering m-sequence stimuli. For example, the sensory G protein *odr-3* is required for avoidance of high osmolarity stimuli, and ASH neurons in an *odr-3* mutant do not respond reliably to 10 s pulses of 1 M glycerol or to the fluctuating m-sequence (Figure 3.10, data not shown, and Hilliard et al., 2005). Similarly, the TRPV channel double mutant *osm-9 ocr-2* lacks behavioral responses to glycerol, and also lacks calcium responses to 10 s pulses of glycerol or fluctuating stimuli (Figure 3.10 and data not shown). A different G protein expressed in ASH, *gpa-3*, is not required either for behavioral responses or for calcium transients to 10 s pulses or m-sequences of glycerol (Figure 3.9B, 3.10). These results suggest that a common sensory transduction cascade initiates ASH calcium responses to both sustained and flickering glycerol stimuli.

The L-type voltage-gated  $Ca^{2+}$  channel encoded by *egl-19* amplifies sensory responses in some *C. elegans* neurons, and is a potential source for calcium signals measured in the ASH cell body (Waggoner et al., 1998; Hilliard et al., 2005). However, ASH calcium responses to 1 M glycerol were only slightly decreased by an *egl-19(n582)* reduction-of-function mutation or by the *egl-19* antagonist nemadipine (Figure 3.6A, 3.10 and data not shown). Although these

results indicate that *egl-19* is not essential for ASH responses to glycerol, there were subtle differences between *egl-19* and the wild-type: calcium responses in *egl-19* rose to peak more slowly, and decayed less than wild-type during either prolonged or sequential presentations of the glycerol stimulus (Figure 3.6A, Figure 3.10). These defects suggest a change in the underlying dynamics of the ASH calcium response.

Indeed, although the ASH neurons in *egl-19* mutants were able to track fluctuating glycerol stimuli presented in the m-sequence (Figure 3.6B), analysis using the L-N method revealed a slowing of the linear filter, which corresponded to changes in a specific component of the ODE model (Figure 3.6C,D). In particular, *egl-19* reduction-of-function mutants appeared to lack the inverted, slow component that attenuates the response over time (Component S in Figure 3.4B). The absence of this component delayed the peak calcium response and extended the positive phase of the response (Figure 3.6D), accounting for the sustained responses to 10 s or 60 s pulses observed in *egl-19* mutants. Conversely, the *egl-19(ad695gf)* gain-of-function mutant had an enhanced slow component, leading to an opposite effect on the temporal filter. These results suggest that the dynamical properties of ASH neurons can be ascribed to discrete molecules, and implicate calcium entry through the EGL-19 voltage-gated  $Ca^{2+}$  channel in the attenuation of sensory responses.

### 3.10 A general model for sensory neuron dynamics

We next investigated the generality of the LN-ODE model by asking whether it could describe the responses of other sensory neurons. Unfortunately, not all neurons are amenable to analysis with rapidly fluctuating stimuli, but an approximate way to estimate a neuron's linear filter is by taking the derivative of its response to a step stimulus, corrected for any response nonlinearity such as the nonlinearity of GCaMP3. Approximating the linear filters for AWC and ASH using the derivative of the nonlinearity-corrected step responses yielded estimated filters related to, but somewhat narrower than, those obtained from the m-sequence data (Figure 3.11A). This difference may reflect additional adaptation of the

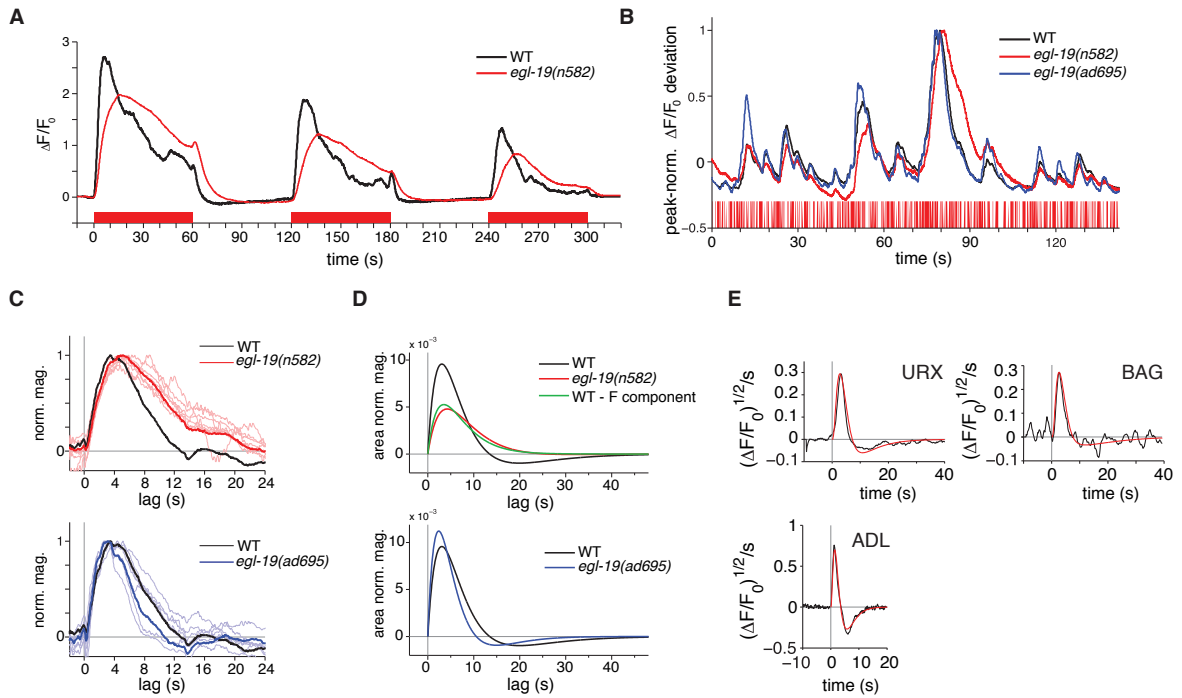


Figure 3.6: Filter analysis reveals a role for *egl-19* in ASH and generality of biphasic model

(A) Trial-averaged responses of ASH wild type ( $n=7$ ) and *egl-19(n582)* ( $n=23$ ) mutants to 60 s on/off pulses of 1 M Gly, with stimulus shown below in red. (B) Excerpt of trial-averaged responses to 200 ms glycerol m-sequences of ASH wild type ( $n=10$ ), *egl-19(n582)* reduction of function mutants ( $n=7$ ), and *egl-19(ad695gf)* gain of function mutants ( $n=7$ ), stimulus shown below in red. (C) Upper panel: linear filter measured from trial-averaged input-output records (red line) and filters from individual input-output records for ASH neurons of *egl-19(n582)* mutants (thin lines), compared to wild-type filter (black). Lower panel: linear filter measured from trial-averaged input-output records (blue line) and filters from individual input-output records for ASH neurons of *egl-19(ad695gf)* gain of function mutants (thin lines), compared to wild-type filter (black). (D) Upper panel: ODE model filter from trial-averaged input-output records for ASH *egl-19(n582)* compared to the wild type ODE filter. The *egl-19(n582)* ODE filter (red) closely matches the ASH wild type fast component filter from Figure 3.4D, shown here in green. Lower panel: ODE model filter from trial-averaged input-output records for ASH *egl-19(ad695gf)* compared to the wild type ODE filter (black). (E) Responses to step stimuli suggest underlying temporal filters for URX (using GCaMP1), BAG (using GCaMP3), and ADL (using GCaMP3) neurons. Figure shows derivatives of the square root of trial-averaged step responses, smoothed with a 10 sample (1 s) box filter (black, see Figure 3.11A for AWC and ASH). And fit to ODE models (red, Table 3.1). The square root approximately corrects for GCaMP cooperativity.

neural responses, as discussed above. Similarly, the derivative of the ASH response in *egl-19(n582)* mutants yielded a slower filter with an attenuated and delayed inverted component, approximating the result obtained by the more rigorous m-sequence analysis (Figure 3.11A).

We extended this estimation method to two classes of oxygen-sensing neurons, BAG and URX. It is not easy to deliver fluctuating oxygen stimuli to these neurons, but analysis of their step responses suggested that they have slightly faster filters than ASH, with a larger inverted component driving a faster decay in URX than in BAG (Figure 3.6E, 3.11B). Another neuron, the pheromone-sensing ADL neuron, appeared to have a rapid and large inverted component that drives a rapid calcium decay (Figure 3.6E, 3.11B).

The ODE model we have used can fit all of the filters shown in Figures 3.6E and 3.11. Because the ODE model appears to be general, we investigated the range of filters it could generate through parameter variation and examined the resulting predictions for neural responses to step stimuli, flickers, or more complex stimulus patterns (Figure 3.12). A monophasic filter produces a stable, non-adapting response to a step stimulus (Figure 3.12A). Biphasic filters with a fast component and a slow component yield the slowly decaying response typical of ASH and AWC neurons, with plateau values determined by the relative area of the second, inverted component compared to the first component (Figure 3.12D,E).

## 3.11 Discussion

The highly reliable responses of AWC and ASH sensory neurons to rapidly fluctuating stimuli suggest that *C. elegans* sensory neurons can operate in a deterministic, low-noise mode with a near-linear transformation of sensory information into calcium signals. These two neurons have distinct temporal properties, but both can encode information on at least two behaviorally relevant timescales: rapid, precise signal processing functions over less than a second (AWC) or a few seconds (ASH), and a decay to a steady-state over tens of seconds. The rapid responses and a significant component of the decay can be described by a single filter expressed in terms of three decaying exponentials through a simple kinetic scheme.

Biphasic filters of this general form are found in sensory systems ranging from bacterial chemotaxis to human psychophysics; in *C. elegans*, it is possible to relate the filters downward to the molecular signaling pathways that generate them and upward to the behaviors that they support.

### 3.11.1 Properties of individual sensory neurons are matched to behaviors

Each *C. elegans* chemosensory neuron has a temporal selectivity that suggests a relationship to the behaviors it subserves. AWC regulates chemotaxis through a biased random walk characterized in turns per minute (Gray et al., 2005; Pierce-Shimomura et al., 1999), but in addition AWC chemotaxis has a deterministic component in which animals orient themselves in a gradient by detecting small local differences in attractant concentrations as their heads move in sinusoidal patterns Albrecht and Bargmann (2011); Iino and Yoshida (2009). Modeling suggests that the optimal neuronal strategy for the head orientation behavior requires neuronal activity modulated on the timescale of individual headswings, a duration of under a second (Izquierdo and Lockery, 2010; Cronin et al., 2005). The rapid first phase of the filter observed here for AWC is well tuned to support this function. The inferred fast timescale of AWC due to the first phase of the filter, with a peak response at  $\sim 250$  ms and a decay to half-max of 1.5 s, is similar to the voltage response of vertebrate olfactory neurons, which respond to single odor-binding events with a peak at 400 ms and a total response time of 1 s (Bhandawat et al., 2005). As the conversion of depolarization into calcium signals could also delay signals, these adjusted values may still be slower than the neuronal voltage responses.

ASH initiates a nociceptive escape behavior with a latency of up to 10 s, depending on the strength of the repellent stimulus (Hilliard et al., 2002; Mellem et al., 2002; Chao et al., 2004). Its peak response at  $\sim 3$  s and  $\sim 10$  s integration time provide a potential neural correlate of the behavioral integration time for nociception. These values appear slow for an escape circuit, but it is important to note that the temporal filter does not determine how

quickly a neuron can respond (this can be much faster). Instead, it defines the temporal frequency at which the neural response to a stimulus is strongest, and the interval over which the signal is integrated.

Although our work is the first report of *C. elegans* sensory responses to rapidly fluctuating stimuli, other studies support the hypothesis that its sensory neurons can perform rapid computations. Notably, a temperature shift generates an AFD current that peaks at  $\sim 500$  ms (Ramot et al., 2008), a similar time frame as the rapid AWC calcium response inferred here. Some forms of *C. elegans* neural activity are faster than the AWC and ASH temporal filters for chemical stimuli, even in the same neurons: ASH and other mechanosensory neurons typically responds to touch within a few milliseconds (Geffeney et al., 2011). We suggest that the chemosensory neurons use relatively slower temporal filters because following signals over time is an essential element of their function, and relatively slow filtering permits chemical stimuli to be evaluated for strength, duration, and rate of change.

### **3.11.2 Monitoring fast neuronal signals with genetically-encoded indicators**

System identification is widely used in electrophysiological studies, but to our knowledge this is the first application of it to calcium imaging data. Ultimately, all neurons regulate neurotransmitter release via presynaptic calcium, so this parameter is a physiologically relevant aspect of neuronal activity. Nonetheless, there are many reasons that this approach could have failed: GCaMP signals could have been too slow to follow neural activity, for example. Many *C. elegans* neurons function using slow graded potentials (Goodman et al., 1998; Liu et al., 2009), which may make them particularly suitable for calcium imaging as an activity measurement. At this point, GCaMP5 and other calcium indicators are close to realistically following single action potential spikes, which would make this experimental and analytical approach possible for faster (mammalian) neurons as well. Clearly, the method is best suited for cells that have substantial stimulus driven, time-invariant components, like those

that were empirically defined here for AWC and ASH. In neurons whose calcium responses are poorly correlated to acute signaling, or in neurons that display significant spontaneous dynamics, this will probably not be a suitable method for analysis.

### 3.11.3 Signaling mutants affect specific features of the model

The ability to map mutations onto specific model features supports the value of these models as a way to describe sensory responses. Animals mutant for the G-alpha protein *odr-3* are defective in AWC chemotaxis to isoamyl alcohol, but less defective in chemotaxis to butanone, and our analysis showed that *odr-3* AWC neurons are selectively impaired in their fast responses to isoamyl alcohol. These odorant-selective changes suggest that the time course of rapid AWC signaling is determined by a specific receptor-G protein interaction, not by a shared downstream process or cell-wide property such as excitability. The match between behavioral and temporal defects for two AWC odors further suggests that rapid AWC temporal dynamics may be important for efficient chemotaxis in gradients. Indeed, the 1.5 s integration time for isoamyl alcohol in *odr-3* mutants would disrupt their ability to evaluate odor gradients with respect to head position during chemotaxis (Izquierdo and Lockery, 2010; Cronin et al., 2005). The G-alpha family in *C. elegans* has expanded in recent evolution, and many members of the family are specifically expressed in small numbers of chemosensory neurons (Jansen et al., 1999). These various G-alpha proteins may be functionally differentiated by the ability to interact with different receptors to generate temporal properties essential for chemosensation.

A role of the *egl-19* voltage-activated calcium channel in the slower, inverted component of the ASH glycerol response also emerged from the model. We expected *egl-19* to amplify sensory signaling or add a nonlinearity to the ASH glycerol response. Instead, the results and model indicate that the strongest effect of *egl-19* on ASH glycerol responses is on response decay. Calcium is a signal for adaptation in many sensory systems, so this conclusion is biologically plausible. To provide a potentially relevant mechanistic example, the

signal transduction pathway for glycerol sensation in ASH depends on TRPV channels, and calcium-calmodulin binding to mammalian TRPV channels strongly decreases their open probability (Lau et al., 2012). Alternatively or in addition, *egl-19* may activate a  $Ca^{2+}$ -dependent  $K^+$  current. Our results do indicate a small role of EGL-19 in the amplification of the signal, in agreement with other work, and there may be other cells and conditions in which EGL-19 is more important for the primary signal. From a more general and practical perspective, the work reported here provides a framework for interpreting the magnitude and dynamics of  $Ca^{2+}$  signals in both wild-type and mutant neurons, in *C. elegans* and in other systems in which genetically-encoded calcium indicators are increasingly used.

Olfactory neurons in various animals have predominantly been probed with step stimuli and not fluctuating stimuli because it is difficult to control odor vapor concentrations and switch them rapidly, and odorant equilibration between volatile (air) and liquid (tissue) phases is inherently slow. Despite these challenges, several groups have studied responses to fluctuating stimuli of sensory and second-order neurons in insects (Vickers et al., 2001; Geffen et al., 2009; Nagel and Wilson, 2011; Su et al., 2011; Kim et al., 2011; French et al., 2011; Riffell et al., 2008). In contrast with the results presented here for *C. elegans*, most studies in insects have suggested that sensory neurons primarily encode odor quality, not odor dynamics. A single *Drosophila* olfactory neuron responds to different odors with different temporal patterns of spikes (Nagel and Wilson, 2011), and the brain can decode these patterns, as flies can behaviorally discriminate two odors that activate the same receptor with different dynamics (DasGupta and Waddell, 2008). Similarly, optogenetic studies have shown that mice can discriminate two patterns of temporal activation of the same primary olfactory sensory neurons (Smear et al., 2011). How these animals encode temporal features of the odor stimuli remains elusive, although several studies indicate that second-order neurons in the insect olfactory system filter the sensory signal to encode odor dynamics (Geffen et al., 2009; Vickers et al., 2001).

An additional contrast between *C. elegans* neurons and other sensory systems is the

preservation of a temporal filter in AWC over a 100-fold range of odor concentrations; in other systems, filtering often becomes slower as a stimulus becomes weaker (Nagel and Doupe, 2006; Benardete and Kaplan, 1999). The compact nervous system of *C. elegans* is forced to use fewer channels of information transmission compared to other nervous systems. It may be that *C. elegans* sacrifices maximal discrimination of odor identity for the advantages provided by immediate temporal coding. Nonetheless, temporal specialization of sensory neurons is not unique to nematodes. For example, vertebrate somatosensory neurons are characterized by strikingly different temporal responses to mechanical stimuli, with classes that are slowly adapting, rapidly adapting, or non-adapting (Johnson and Hsiao, 1992). Different temporal properties also distinguish the various classes of vertebrate olfactory, vomeronasal, and taste cells that use different G protein-coupled transduction pathways (Kaupp, 2010). Exploring variations of temporal coding in these systems could provide a fruitful avenue for understanding functional diversity. A general model for sensory temporal filtering The function of a biphasic filter depends on the relative durations and integrated areas of its phases. Analysis of responses to step inputs offers an intuitive way to understand a filter's effect (Figure 3.12). A purely monophasic filter reports the strength of a stimulus, a biphasic filter with phases of equal area can generate perfect adaptation, and a partially biphasic filter provides information about both intensity and change. One way to reconcile different task requirements is to perform parallel computations over different timescales; here, one filtering mechanism effectively maps both stimulus onset or offset, and features of the internal structure of the stimulus.

The biphasic filter with disparate phase widths has been reported in many other settings, with various proposed functions. In the context of chemotactic behavioral response of bacteria, this filter shape (Segall et al., 1986) has been proposed as an optimal fitness balance between the goals of reaching locations of maximum attractant and the speed of gradient climbing (Clark and Grant, 2005). As a temporal receptive field in mammalian vision, this shape has been proposed as a balance between the decorrelation of stimulus redundancy and

filtering of noise for the purpose of efficient neural coding (Atick and Redlich, 1990). In the context of the *C. elegans* sensory network, we propose that the disparate phase width biphasic filter has a temporal multiplexing function: it allows a single neuron to carry a memory trace about a past large shift in stimulus statistics while simultaneously tracking ongoing stimulus fluctuations.

## 3.12 Experimental Procedures

### 3.12.1 Calcium Imaging

Calcium imaging lines in the AWC and ASH neurons were created expressing the genetically encoded calcium indicator GCaMP3 (Tian et al., 2009) under the *sra-6* and *str-2* promoters, respectively. One-day old adult worms were trapped in a custom-designed microfluidic device made of transparent PDMS polymer, where their noses were exposed to liquid streams under laminar flow (Chronis et al., 2007). Switching between odor streams was accomplished by controlling flow to two adjacent laminar side-streams, a protocol that minimized fluid pressure changes during odor delivery (Figure 3.7). Movement artifacts were minimized by adding a cholinergic agonist, 1mM tetramisole, to the worm-loading channel. Tetramisole had no apparent effect on chemosensory responses in AWC or ASH neurons. Wide-field microscopy was used to monitor fluorescence from the cell of interest as stimuli were presented, as well as the fluorescein dye in the stimulus channel. Measured dye fluorescence in each frame was used as a surrogate for odor concentration for modeling.

### 3.12.2 Stimulus Delivery

Stimuli were 1 M glycerol (ASH), and  $9.2 \times 10^{-4}$  M isoamyl alcohol (AWC), diluted in and alternating with S basal buffer. ASH imaging was preceded by a 90 s exposure to blue light to reduce its intrinsic light response (Hilliard et al., 2005). AWC imaging began after a 5-minute exposure to isoamyl alcohol or butanone. Stimulus presentation was automated using ValveBank (AutoMate Scientific) and LabJack interfaces to control a solenoid valve

(LFAA1201610H, The Lee Company) with a pre-generated sequence. Switch time limitations were initially evaluated using 100 ms, 200 ms, 500 ms, 1 s, and 2 s flicker presentations for 5 minutes per trial to worms expressing GCaMP3 in ASH under the *Psra-6* promoter. Protocols using S basal buffer as background and either 1M glycerol (with fluorescein) or S Basal buffer (with fluorescein) as the stimulus were used at each timescale to compare ASH calcium activity with stimulus onset. Measurement of fluorescein dye in the liquid stream near the worm’s nose showed reliable square waves of dye fluorescence at 200ms switch times. Insignificant changes in ASH calcium signals were observed when the flickering stimulus switched between S basal and S basal with 1:250,000 dilution of fluorescein, allowing the use of fluorescein dye as a surrogate for odor concentration. Subsequent control experiments indicated that AWC and ASH calcium signals were insensitive to fluorescein inclusion with odor.

The m-sequence pulse length was limited to a minimum of 200 ms because of the mechanical limit of the microfluidic switch, assessed by tracking fluorescein. ASH calcium activity in response to 1 M glycerol (with fluorescein) had a near-fusion response to 200 ms flicker, indicating that the cell or sensor was close to its limit for tracking the stimulus; AWC responses were faster. Pseudo-random sequences were 2x (AWC) or 3x (ASH) repeats of 9-bit m-sequences.

### 3.12.3 Analysis of Cell Activation

A Coolsnap HQ (Photometrics) camera controlled by Metamorph (Molecular Devices) software was used to capture stacks of TIFF images at 20 frames/sec (AWC and ASH) during the odor presentation sequence. The average fluorescence intensity for each cell body was generated for each frame by averaging the pixel intensity of the top 100 pixels within a fixed bounding box surrounding the cell throughout the movie, then subtracting the average intensity of a 25 pixel background region adjacent to the bounding box. MATLAB (The Mathworks) was used for subsequent trace processing. Change in fluorescence intensity for

the region of interest relative to  $F_0$  was plotted for each trial individually, where  $F_0$  was defined to be the average fluorescence in a 3 s window ( $t=1-4$  s).

### 3.12.4 Trace Pre-Processing and Bleach Correction

Prior to model estimation, we pre-processed the traces to account for jitter in frame acquisition times and photobleaching. Jitter was corrected for by resampling each input and output record at regular time intervals at the intended frame rate of  $0.05 \text{ s}^{-1}$  using linear interpolation. When trial averaging was required, records were first time registered by shifting each record to have the same stimulus onset.

Bleach-corrected fluorescence traces were computed by transforming the measured fluorescence  $F(t)$ :

$$F_{corr}(t) = \frac{F(t)}{[F_{min}(0)/F_{min}(T)]^{t/T}} - F_{min}(0)$$

where  $F_{min}(0)$  is the mean baseline fluorescence in the 2 s just before (set to be  $t = 0$ ) and  $F_{min}(T)$  is the mean baseline fluorescence in the 2 s just after a stimulus sequence ( $t = T$ ). To derive the bleach correction equation, we model photobleaching as a decay of sensitivity over time which affects all fluorescence levels as a multiplicative factor  $B(t) = Ae^{-t/\tau}$ . The function parameters  $A$  and  $\tau$  are determined by fitting  $B(t)$  through the points  $(F_{min}(0), 0)$  and  $(F_{min}(T), T)$ . This model of photobleaching has the net effect of reducing both the baseline fluorescence and its dynamic range over time, an effect not incorporated into purely subtractive fluorescence bleach correction procedures such as that used in the last chapter.

As a final step prior to estimation, input-output records were trimmed to begin 45 s after initiation of the m-sequence stimulus to avoid non-stationarity due to the slowly adapting response to the large mean stimulus shift at the onset of the m-sequence.

### 3.12.5 Linear-Nonlinear Model Estimation

Fully sampled linear filters  $K$  were estimated from pre-processed input-output records using least-squares regression. Filters were restricted to be 520 samples long, consisting of acausal and causal samples. Trial-averaged filters were estimated by first trial-averaging pre-processed input and output records after jitter correction and time registration. Regression was performed as described in the introduction.

Singular value decomposition was used to denoise  $K$ , using 100 components. Once an initial estimate of the linear filter  $K(\tau)$  was obtained, the associated instantaneous nonlinear function  $F(x)$  was estimated by least-squares fitting a power-law curve of the form to a scatter plot of intermediate signal values versus output values  $y(t)$ . The Nelder-Mead simplex method for nonlinear optimization was used to find the parameters  $a$ ,  $p$ , and  $c$ . An iterative scheme was used to generate improved estimates of  $K$  and  $F$  by reducing bias error (Hunter and Korenberg, 1986). Model parameters did not change significantly after the second iteration.

### 3.12.6 Dynamical Model Estimation and Correction for GCaMP Response Dynamics

We generated analytical versions of each filter with five free parameters by defining them to be the result of convolution of the putative GCaMP filter (Dombeck et al., 2010) and the impulse response of a third-order linear system (Figure 4A) given by the following equations, where  $u(t)$  is input and  $y(t)$  is output:

$$\frac{dA}{dt} = -k_A A + u(t)$$

$$\frac{dF}{dt} = -k_f F + k_{af} A$$

$$\frac{dS}{dt} = -k_s S - k_{as} A$$

$$y(t) = F + S$$

The linear filter arising from these equations is the impulse response, which is the solution for an input given by a  $\delta$ -function and the initial condition  $A(0) = B(0) = C(0) = 0$ , and is

$$h(t) = \frac{k_{af}k_a k_f}{k_a - k_f} e^{-k_f t} - \frac{k_{as}}{k_a - k_s} e^{-k_s t} + \left( \frac{k_{as}}{k_a - k_s} - \frac{k_{af}}{k_a - k_f} \right) e^{-k_a t}$$

The optimal parameters of these filters were found by replacing linear regression with least squares Nelder-Mead optimization of the dynamical model parameters.

We model the filter describing the GCaMP response as the difference of two exponentials (Dombeck et al., 2010): where  $k_1 = 1/(.2734) s^{-1}$  and  $k_2 = 1/(.1877) s^{-1}$ . The convolution of the GCaMP and neuronal impulse can be computed in a straightforward manner to obtain an expression for the full filter. To analytically deconvolve the intrinsic neural impulse response, we fit this computed full filter expression to the observed data using linear regression as described in Experimental Procedures. We then use the resulting optimized parameters in the expression for the neural filter  $K_{neuron}(t)$ .

### 3.12.7 Worm Cultivation and Strains

Strains were cultivated on agar plates seeded with *E. coli* strain OP50 at room temperature ( $\sim 22^\circ\text{C}$ ). Standard methods for molecular biology were used. Strains used in this study are:

CX10979 *kyEx2865 [Psra-6::GCaMP3.0+ Pofm-1::gfp]*

CX13131 *gpa-3(pk35) V; kyEx2865 [Psra-6::GCaMP3.0+ Pofm-1::gfp]*

CX13128 *egl-19(ad695gf) IV; kyEx2865 [Psra-6::GCaMP3.0+ Pofm-1::gfp]*

Table 3.1: Parameter values of the ODE filter model (Figure 3.4B) fit to trial averaged input-output records for various neurons and mutants.

neuron	$1/k_a(\text{s})$	$1/k_f(\text{s})$	$1/k_s(\text{s})$	$k_{as}/k_{af}$
AWC	2.99	0.04	10.88	2.40E-03
ASH	3.59	4.10	5.92	5.56E-01
ASH <i>egl-19(n582)</i>	4.79	4.21	7.51	1.89E-01
ASH <i>egl-19(ad695gf)</i>	3.23	2.93	3.67	6.86E-01
BAG	1.13	1.13	18.21	4.98E-02
URX	1.37	1.37	18.21	1.29E-01
ADL	1.79	1.17	1.80	6.56E-01

CX13129 *egl-19(n582)* IV; *kyEx2865 [Psra-6::GCaMP3.0+ Pofm-1::gfp]*

CX11935 *kyEx3252 [Pstr-2::GCaMP3.0+ Pofm-1::gfp]*

CX13838 *odr-3(n2150)* V; *kyEx3252 [Pstr-2::GCaMP3.0 + Pofm-1::gfp]*

CX13132 *gpa-3(pk35) odr-3(n1605)* V; *kyEx2865 [Psra-6::GCaMP3.0+ Pofm-1::gfp]*

CX12739 *osm-9 (ky10) ocr-2 (ak47)* IV; *kyEx2865 [Psra-6::GCaMP3.0+ Pofm-1::gfp]*

### 3.13 Supplementary Figures

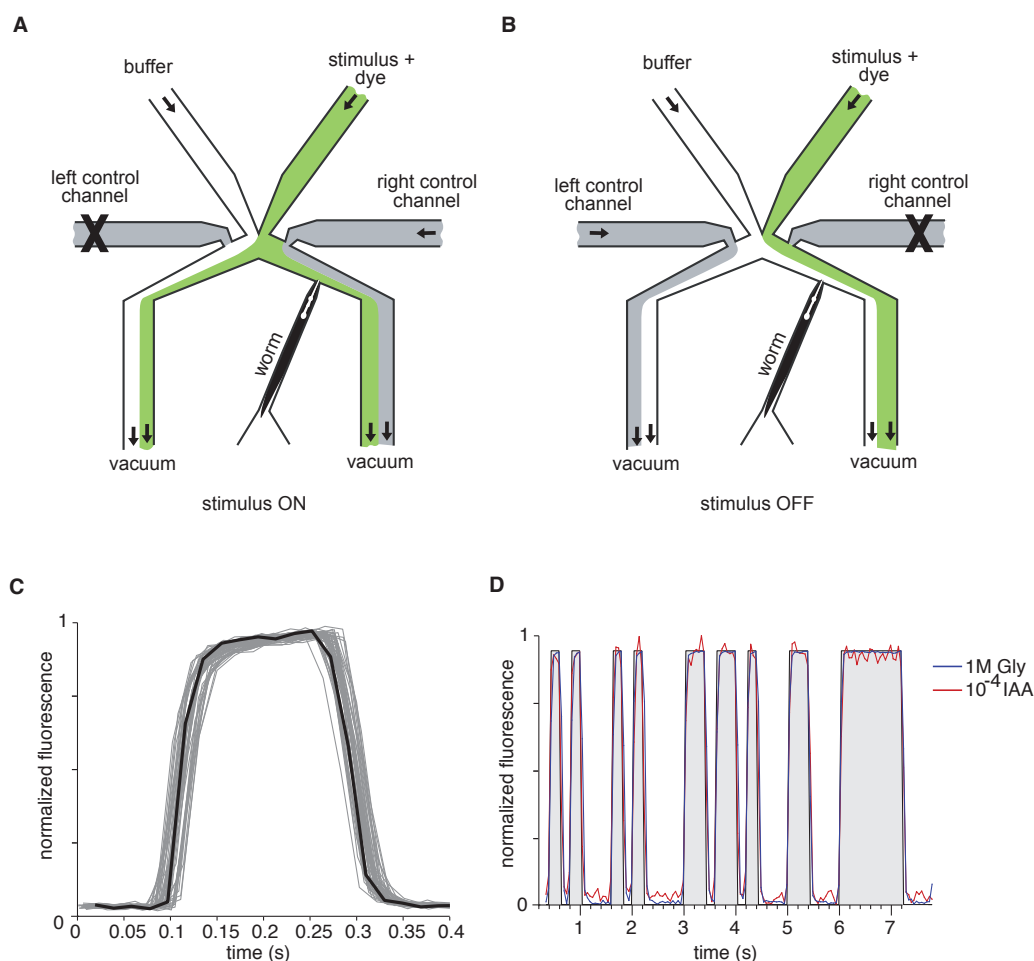


Figure 3.7: Precise control of stimulus delivery

(A, B) Schematic of laminar fluid control by switching flow between side channels in a microfluidic chip during imaging. (A) Stimulus ON state showing stream of stimulus and fluorescein dye (green) flowing across worm nose. (B) Stimulus OFF state showing stream of buffer (white) flowing across worm nose. (C) Superposition of 50 consecutive time segments of normalized dye intensity for a 200 ms on/off square wave stimulus pattern, recorded at a frame rate of 50 Hz. Individual segments shown in grey and mean intensity in black. Both off-on and on-off transitions were typically completed in  $\sim 50$  ms. (D) Representative normalized dye intensity during delivery of pseudo-random stimulus patterns of 1 M glycerol (blue) and  $9.2 \times 10^{-4}$  M isoamyl alcohol (red), superimposed over the electronic valve control signal. The reliability and transition time of the stimulus switching sequence were independent of the stimulus.

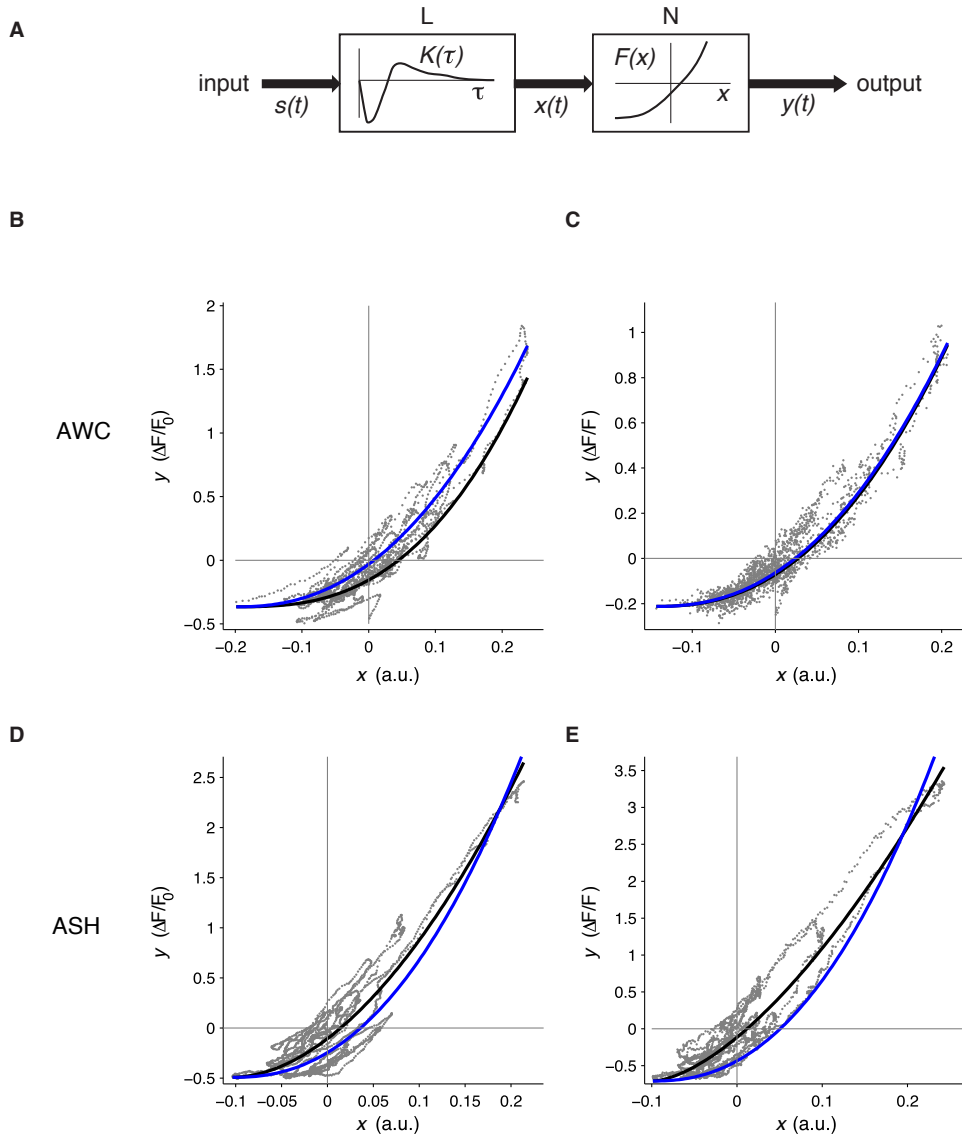


Figure 3.8: The static nonlinearity of AWC and ASH responses approximates the nonlinearity of GCaMP3

(A) Schematic of the L-N model. (B-E) Scatter plots of intermediate filtered signal  $x(t)$  versus output  $y(t)$  for L-N models composed from trial-averaged input-output records of AWC (B) and ASH (D), or representative individual m-sequence trials of AWC (C) and ASH (E), after linear filters and  $x(t)$  were estimated from input-output records. Black lines indicate the N power-law function least-squares fit to the scatter data. For comparison, blue curves indicate a power-law function fit to the scatter data with the power constrained to be 2.3, the Hill coefficient value for GCaMP3 reported in Tian et al., 2009.

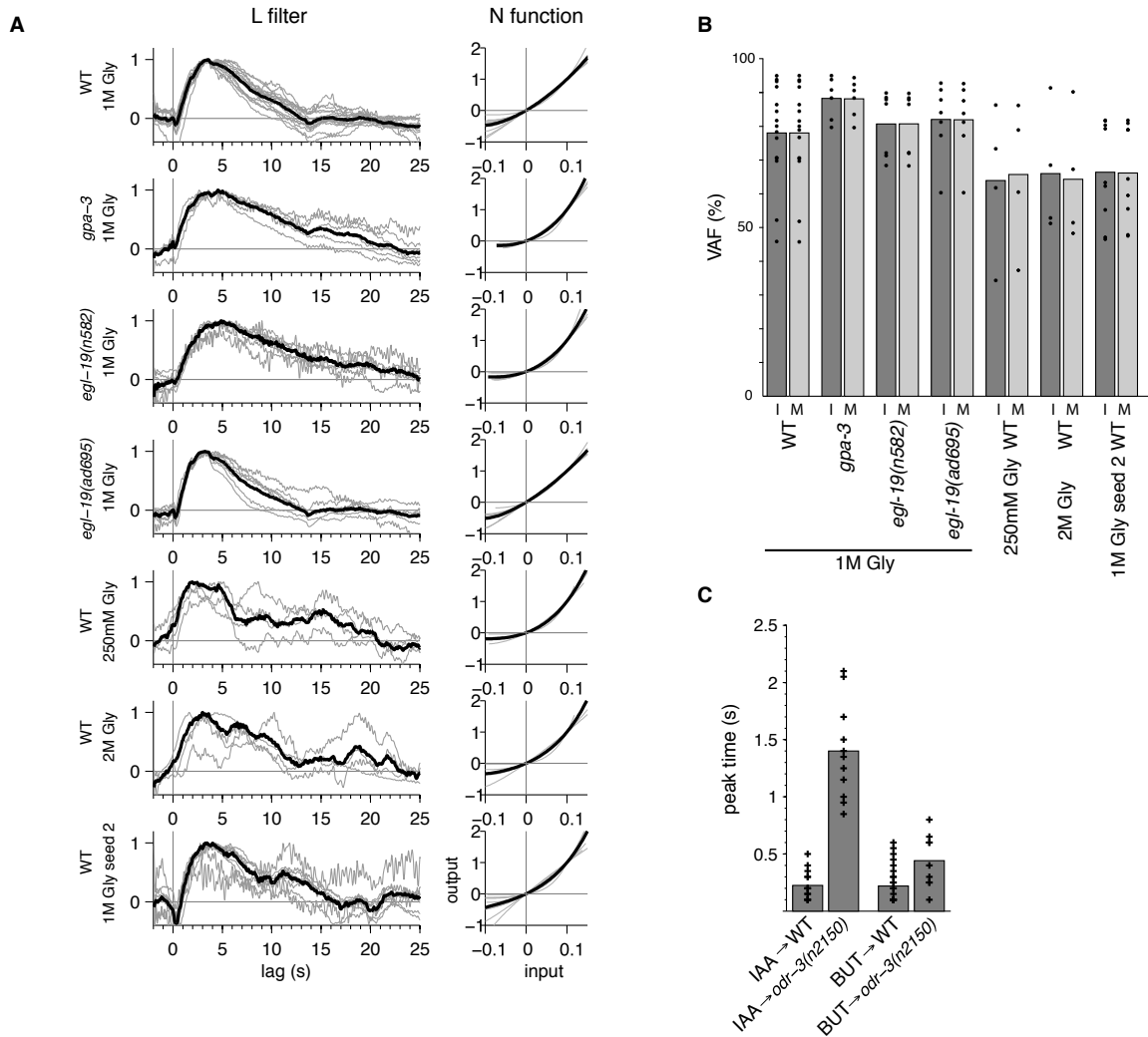


Figure 3.9: Robustness of ASH wild type filters to concentration and m-sequence structure, and effects of signal transduction mutants.

(A) Linear filters and nonlinear functions of L-N models extracted from m-sequence trials of wild type at different glycerol concentrations, and in mutants, showing individual trial filters (gray) and trial-averaged filters (black). (B) Performance (% variance of accounted for) of individual trial L-N (denoted I) and trial average L-N models (denoted M). (WT 1M Gly,  $n=10$ ; *gpa-3*,  $n=6$ ; *egl-19(n582)*,  $n=7$ ; *egl-19(ad695gf)*,  $n=7$ ; WT 250mM,  $n=3$ ; WT 2M,  $n=4$ ; WT m-sequence seed 2,  $n=9$ ). (C) Time to peak response in wild type and *odr-3* AWC neurons, as in Figure 3.3E, corrected for slowing due to GCaMP kinetics, as in Figure 3.4E.

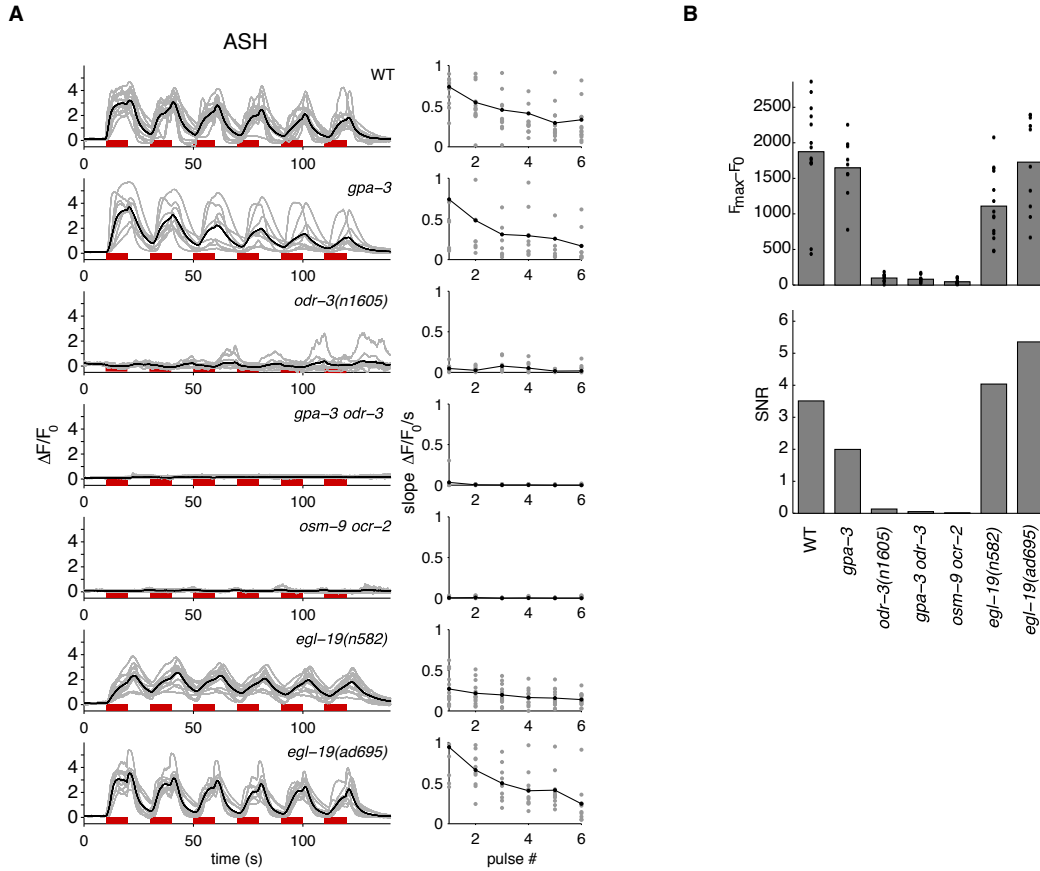


Figure 3.10: ASH signal transduction mutant responses to 10 s glycerol pulses

(A) Left column: ASH responses to six 10 s on/off pulses of 1 M glycerol in wild type and signal transduction mutants. Right column: slope of the onset of each pulse response versus pulse number (measured between  $x$  and  $x$  s after stimulus switch), solid black dots showing trial-average onset slope for each pulse. (wild type,  $n=12$ ; *gpa-3(n1605)*,  $n=10$ ; *gpa-3 odr-3*,  $n=10$ ; *osm-9 ocr-2*,  $n=14$ ; *egl-19(n582)*,  $n=14$ ; *egl-19(ad695gf)*,  $n=10$ ) (B) Dynamic range and signal-to-noise ratio of responses in (A). Dynamic range is calculated as peak fluorescence minus baseline fluorescence. Signal-to-noise ratio is calculated as in Sahani and Linden, 2003.

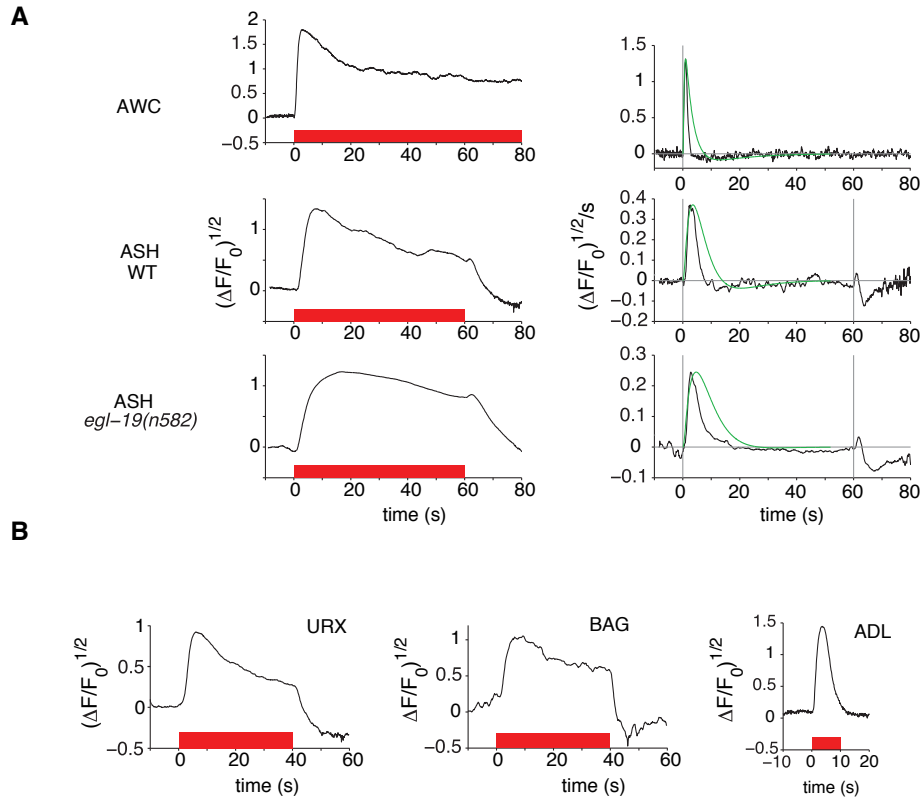


Figure 3.11: A biphasic filter with distinct phase widths underlies a general response of sensory neurons

(A) Responses to step stimuli suggest underlying temporal filters. Left column: square-root of trial-averaged responses to steps of various lengths of AWC, ASH wild type, and ASH *egl-19(n582)* mutant neurons, with stimulus at bottom in red. The square root approximately corrects for GCaMP cooperativity. Right column: derivatives of square-root trial-averaged responses. Derivatives were smoothed with a 10 sample (1 s) box filter. In a fully linear system, the derivative of a step response should correspond to the linear filter. For the first three traces, green curves show ODE filters estimated from m-sequence experiments at pseudo-steady state; these filters are related to, but slower than, the derivative of the step response. (AWC,  $n=2$ ; ASH WT,  $n=7$ ; ASH *egl-19(n582)*,  $n=23$ ; BAG,  $n=40$ ; URX  $n=42$ ). (B) Step responses of BAG, URX, and ADL filters used to generate derivatives in Figure 3.6E (presented as in panel (A), left).

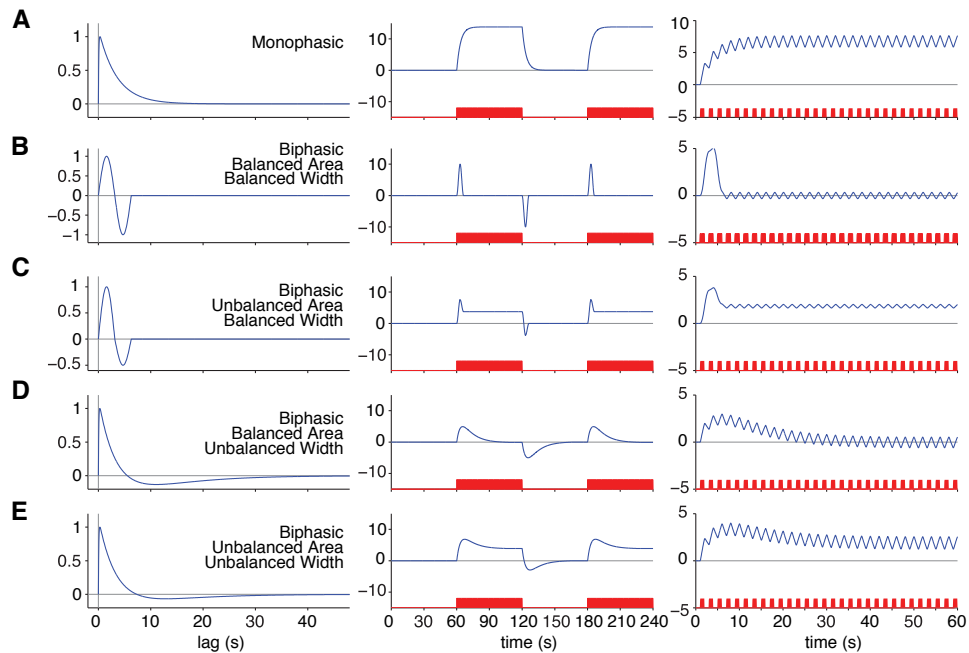


Figure 3.12: Response features of biphasic filters are determined by the balance of phase area and phase width

Left column: (A) Model monophasic filter corresponding to the AWC ODE model with the  $k_{as}$  parameter (see Figure 3.4B) set to zero. (B) Model biphasic filter with balanced phase area and balanced phase width generated by one period of a sine wave. (C) Model biphasic filter with unbalanced area and balanced width generated by halving the magnitude of the second phase of model in (B). (D) Model biphasic filter with balanced phase area and unbalanced phase width created by adjusting the AWC ODE parameters of  $k_{af}$  and  $k_{as}$  to give phases of equal area. (E) Model biphasic filter with unbalanced area and unbalanced width corresponding to the AWC ODE model. Middle column: responses of each model filter to 60 s pulse trains. Right column: responses of each model filter to 1 s pulse trains.

# Chapter 4

## Conclusion

### 4.1 Future work: locating and modeling sensory integration

We hypothesize that one function of interneurons that would have to occur after the sensation of individual sensory streams but before generation of motor commands would be the integration of sensory modalities and possibly internal state to perform some behavioral logic. We may suppose that the behavioral logic computation would be localized at or near a point where the sensory inputs converge. Since all sensory neurons have connections from other sensory neurons, some of these multi-sensory integration sites may be in the sensory neurons themselves. This may seem surprising, since if a neuron with sensory-driven activity  $A$  is synapsing onto a neuron with sensory-driven activity  $B$  and affecting it, it would seem to imply that the rest of the nervous system would only have access to the outcome of the computation  $F(A, B)$  and not the full, raw sensory information in the  $B$  signal, effectively losing some opportunity for fitness-improving flexible behavior unless the transformation  $B \rightarrow F(A, B)$  is perfectly information preserving (Cover and Thomas, 2006). However, there is growing evidence that in some *C. elegans* neurons, calcium activity is compartmentalized, effectively dividing the neuron into two or more functionally distinct, but coupled,

units (Hendricks et al., 2012). This would allow  $F(A, B)$  to be carried out in one compartment and the information of  $B$  to be preserved in another. It also cannot be ruled out that there are other activity signal carriers that operate within a neuron in parallel to calcium, potentially allowing both  $B$  and  $F(A, B)$  to be transmitted. In any case, information must be discarded at some point in order to produce discrete, holistic behavior, and ultimately, this kind of seemingly premature signal logic may simply be happening in biological systems despite our intuitions.

In any case, we can consider a potential sensory integration neuron as a MISO system that should be treatable by integral approaches, analogous to a two or few-pixel retina. White noise experiments, with multiple input streams, would be a good starting point for testing this hypothesis. Since interneurons have many inputs and tend to display activity not apparently related to the stimulus under experimental control, the capturing of an interpretable response may require partial silencing of an interneuron’s neighbor neurons not driven by known stimulus responses, for example by using a genetically encoded pharmacologically gated ion channel under intersectional control of expression.

## 4.2 Future work: inference of nonlinear differential models

We appear to have gotten lucky: we were able to proceed from a phenomenological integral model to a mechanistic differential model so easily due to the strong linear character and relatively simple behavior of our neurons. There is evidence that in other *C. elegans* neurons, intrinsically nonlinear responses occur even for input signals that stay within behaviorally relevant concentration regimes (Larsch, 2013). These nonlinearities include paired pulse inactivation and concentration-dependent changes in the shape of step responses. Therefore, it behooves us to consider a broader strategy. There is likely to be no general procedure for the inference of nonlinear differential equation models in all situations. Nevertheless, with the availability of modern computing resources, search-based strategies for model selec-

tion may be feasible (Koza, 1992). One such approach searches for invariant mathematical relationships between measured variables, which in turn can suggest simple systems of differential equations, i.e. equations of motion (Schmidt and Lipson, 2009). However, for non-conservative systems involving hidden variables, invariances may be hard to discover. A related approach attempts to search for nonlinear but algebraically simple right-hand side functions using an evolutionary algorithm in combination with active probing of the system using modifications of input data to distinguish candidate models (Bongard and Lipson, 2007). We suggest another approach: first, catalogue the repertoire of behavior for certain restricted classes of nonlinear functions and parameter regimes by producing multi-dimensional parameter landscapes similar to the well-known parameter landscape diagram of second-order linear time-invariant systems. Then match the catalogue to qualitative properties of input-output data, guiding model selection. Parameter search could then be pursued in a principled way with convergence guarantees (Girolami, 2008).

One class of right-hand side functions to investigate would be those generally available in cells, including mass-action laws, which produce functions consisting of sums of product terms of only a few state variables. If reactants are limited to two for each reaction, an example function would be:

$$\frac{dA}{dt} = k_{AA}A + k_{AAB}AB + k_{ADB}DB + \dots + k_{AAu}Au + k_{Au}u$$

Work as already been done to analyze specific low-order systems of equations built from mass-action laws (Connors, 1990), but a systematic set of portraits of dynamical behavior in this class has not been produced. It could potentially be accomplished using a combination of basic analysis and computer search. While this class is a modest departure in definitional complexity from linear ODEs, with the admission of only three state space variables it already includes systems with chaotic attractors such as the celebrated Lorenz attractor or Rössler attractor with only a single product term added to a third-order linear system (Robinson, 2004). Once built, the catalog could be used as a basis for automated model selection.

### 4.3 What might a total circuit model look like?

Do we need to describe the dynamics of each and every last neuron in extreme detail in order to build a model that will give a satisfactory explanation of how non-reflexive<sup>1</sup> behavior arises out of neural circuits? We hope not, and in fact, we suspect that without some general principles of organization and part interaction built into the dynamics, a “kitchen-sink”<sup>2</sup> simulation will fail to yield a robust functioning nervous system. Furthermore, due to the high dimensionality of inputs to even *C. elegans* neurons, it will be hard to exhaustively probe a large enough amount of the input space to consider a neuron sufficiently captured; we will, as in other systems, need to make educated and iterative decisions about the input spaces to probe and the level of detail of the models we use. We hope that after studying more neurons, we will be able induce general principles of architecture that are necessary and sufficient to produce flexible platforms for sophisticated behavior. A discovery of these principles should greatly inform the related search for the “neural rule set” encoded into the genome that drives nervous systems to robustly wire up and tune during development to produce the behavioral platform that we consistently observe from animal to animal.

Let us take a wildly uninformed stab at what a general architecture for flexible behavior might look like. We hypothesize a three-layer architecture. We suppose that the sensory layer is mostly for transducing sensory input into a usable internal signal, taking care of signal amplification, dynamic range adjustment, and histogram equalization. Its dynamics are strongly driven by input. We suppose that there is an intermediate logic layer responsible for multisensory integration and decision making by the evolution of active intrinsic dynamics under the influence of perturbations coming from the sensory layer. This layer maintains internal behavioral state variables encoded by bistable neurons, stable attractors arising from assemblies of neurons, and slowly changing neuromodulator concentrations. Finally,

---

<sup>1</sup>We suspect that the distinction between reflexive and non-reflexive action that may seem sharp for our own behavior may blur into a continuum of simple, localized to complex, distributed computation in the worm.

<sup>2</sup>As in, everything but the kitchen sink.

we suppose that there is a motor neuron layer that is responsible for converting internal state modes into initiations of sequences of motor commands executed by neuromuscular chains. The connectivity between each layer is mostly feedforward, while there is high recurrent connectivity within each layer. It should be noted that there is fairly weak evidence from the connectome for an obviously layered architecture.

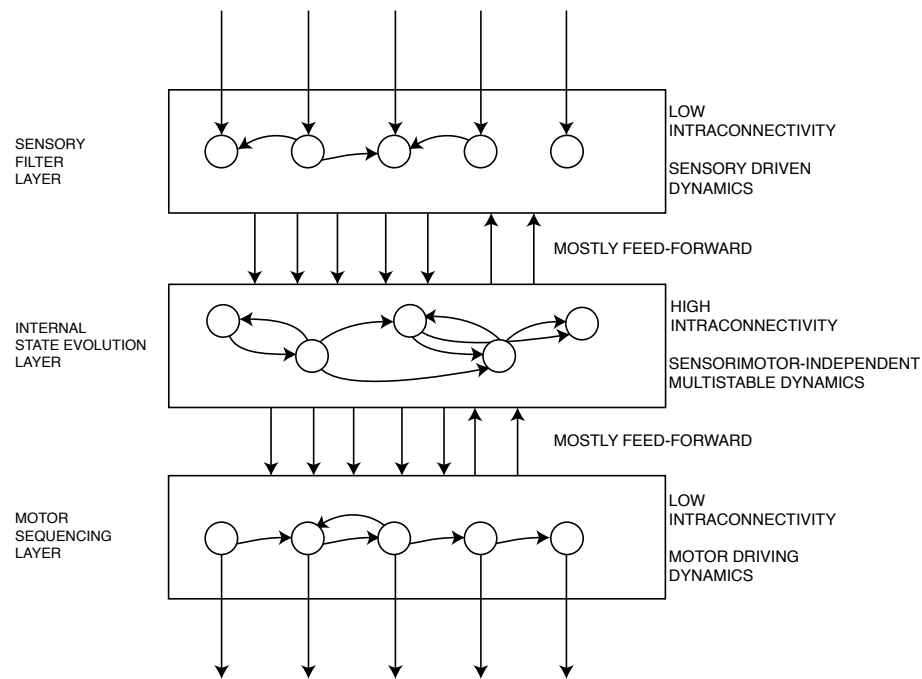


Figure 4.1: A wild guess at a general architecture for worm behavior

It is a topic of future work to sharpen this picture and whittle down a set of testable hypotheses of what such an architecture can and can't do well versus other potential general architectures.

## 4.4 Final thoughts

We have found that *C. elegans* sensory neurons can operate in a highly reliable, deterministic mode. A linear model does an excellent job of describing the temporal response of these neurons to a fluctuating, stationary stimulus, and also predicts the response to non-stationary stimuli to a good degree. Other efforts at mapping out the dynamics of the worm nervous system have begun to work their way in from the other side, the motor system. Much of the initial quantitative work has been to describe the dynamics of the worm's movements themselves (Stephens et al., 2011; Brown et al., 2013). From there, researchers are beginning to understand how these organized movements are created by muscles and motor neurons (Wen et al., 2012). Ultimately, these efforts will meet in the middle and make sense of the activities of the networks of interneurons that are, by virtue of their lack of direct connection to the outside world, computing on abstract representations embodied in the neural activity of their neighbors. Some researchers aren't waiting for this convergence and are taking a stab directly at interneurons that show correlations to both sensory input and motor state (Hendricks et al., 2012), although descriptions of dynamics have been limited thus far to broad correlations, since it has been difficult to make sense of the activity data which display large and frequent fluctuations of unknown origin. We simply don't know the dynamical rules at play inside the network and careful, controlled experiments will have to be done to yield them. Once we chase the homunculus out of all the dark shadows, perhaps we will come to an understanding of how apparently holistic, robust, and intentional behavior emerges from a collection of squishy, dynamical information processing units.

# Bibliography

- D. R. Albrecht and C. I. Bargmann. High-content behavioral analysis of *Caenorhabditis elegans* in precise spatiotemporal chemical environments. *Nat Methods*, 8(7):599–605, 2011.
- J. J. Atick and A. N. Redlich. Towards a theory of early visual processing. *Neural Computation*, 2(3):308–320, 1990.
- L. Avery and J. H. Thomas. Feeding and defecation. In *C. elegans II*, pages 679–716. 1997.
- C. I. Bargmann. Neurobiology of the *Caenorhabditis elegans* genome. *Science*, 282(5396):2028–33, 1998.
- C. I. Bargmann. Chemosensation in *C. elegans*. *WormBook*, pages 1–29, 2006a.
- C. I. Bargmann. Comparative chemosensation from receptors to ecology. *Nature*, 444(7117):295–301, 2006b.
- C. I. Bargmann and I. Mori. Chemotaxis and thermotaxis. In D. L. Riddle, T. Blumenthal, B. J. Meyer, and J. R. Priess, editors, *C. elegans II*. Cold Spring Harbor (NY), 2nd edition, 1997.
- C. I. Bargmann, E. Hartwig, and H. R. Horvitz. Odorant-selective genes and neurons mediate olfaction in *C. elegans*. *Cell*, 74(3):515–27, 1993.
- N. Barkai and S. Leibler. Robustness in simple biochemical networks. *Nature*, 387(6636):913–7, 1997.
- E. A. Benardete and E. Kaplan. The dynamics of primate m retinal ganglion cells. *Vis Neurosci*, 16(2):355–68, 1999.
- J. S. Bendat and A. G. Piersol. *Measurement and analysis of random data*. Wiley, New York, 1966.
- H. C. Berg. *E. coli in motion*. Springer-Verlag, New York, 2004.
- V. Bhandawat, J. Reiser, and K. W. Yau. Elementary response of olfactory receptor neurons to odorants. *Science*, 308(5730):1931–4, 2005.
- J. Bongard and H. Lipson. Automated reverse engineering of nonlinear dynamical systems. *Proc Natl Acad Sci U S A*, 104(24):9943–8, 2007.

- N. Brenner, W. Bialek, and R. de Ruyter van Steveninck. Adaptive rescaling maximizes information transmission. *NEURON-CAMBRIDGE MA-*, 26(3):695–702, 2000.
- A. E. X. Brown, E. I. Yemini, L. J. Grundy, T. Jucikas, and W. R. Schafer. A dictionary of behavioral motifs reveals clusters of genes affecting *Caenorhabditis elegans* locomotion. *Proceedings of the National Academy of Sciences*, 110(2):791–796, 2013.
- G. Burnstock. Cotransmission. *Curr. Opin. Pharmacol.*, 4:47–52, 2004.
- K. E. Busch, P. Laurent, Z. Soltesz, R. J. Murphy, O. Faivre, B. Hedwig, M. Thomas, H. L. Smith, and M. de Bono. Tonic signaling from o(2) sensors sets neural circuit activity and behavioral state. *Nat Neurosci*, 15(4):581–91, 2012.
- J. J. Bussgang. Crosscorrelation functions of amplitude-distorted gaussian signals. *MIT Research Laboratory of Electronics Technical Report*, (216), 1952.
- A. Calabrese, J. W. Schumacher, D. M. Schneider, L. Paninski, and S. M. Woolley. A generalized linear model for estimating spectrotemporal receptive fields from responses to natural sounds. *PLoS One*, 6(1):e16104, 2011.
- A. Celani and M. Vergassola. Bacterial strategies for chemotaxis response. *Proc Natl Acad Sci U S A*, 107(4):1391–6, 2010.
- S. H. Chalasani, N. Chronis, M. Tsunozaki, J. M. Gray, D. Ramot, M. B. Goodman, and C. I. Bargmann. Dissecting a circuit for olfactory behaviour in *Caenorhabditis elegans*. *Nature*, 450(7166):63–70, 2007.
- M. Chalfie, J. E. Sulston, J. G. White, E. Southgate, J. N. Thomson, and S. Brenner. The neural circuit for touch sensitivity in *Caenorhabditis elegans*. *J Neurosci*, 5(4):956–64, 1985.
- M. Y. Chao, H. Komatsu, H. S. Fukuto, H. M. Dionne, and A. C. Hart. Feeding status and serotonin rapidly and reversibly modulate a *Caenorhabditis elegans* chemosensory circuit. *Proc Natl Acad Sci U S A*, 101(43):15512–7, 2004.
- N. Chronis, M. Zimmer, and C. I. Bargmann. Microfluidics for in vivo imaging of neuronal and behavioral activity in *Caenorhabditis elegans*. *Nat Methods*, 4(9):727–31, 2007.
- D. A. Clark and L. C. Grant. The bacterial chemotactic response reflects a compromise between transient and steady-state behavior. *Proc Natl Acad Sci U S A*, 102(26):9150–5, 2005.
- D. A. Clark, D. Biron, P. Sengupta, and A. D. Samuel. The afd sensory neurons encode multiple functions underlying thermotactic behavior in *caenorhabditis elegans*. *J. Neurosci.*, 26:7444–7451, 2006.
- H. A. Colbert and C. I. Bargmann. Odorant-specific adaptation pathways generate olfactory plasticity in *C. elegans*. *Neuron*, 14:803–812, 1995.

- H. A. Colbert, T. L. Smith, and C. I. Bargmann. Osm-9, a novel protein with structural similarity to channels, is required for olfaction, mechanosensation, and olfactory adaptation in *Caenorhabditis elegans*. *J. Neurosci.*, 17:8259–8269, 1997.
- K. A. Connors. *Chemical kinetics : the study of reaction rates in solution*. VCH, New York, N.Y., 1990.
- The *C. elegans* Sequencing Consortium. Genome sequence of the nematode *C. elegans*: A platform for investigating biology. *Science*, 282(5396):2012–2018, 1998.
- T. M. Cover and J. A. Thomas. *Elements of information theory*. Wiley-Interscience, Hoboken, N.J., 2nd edition, 2006.
- C. J. Cronin, J. E. Mendel, S. Mukhtar, Y. M. Kim, R. C. Stirbl, J. Bruck, and P. W. Sternberg. An automated system for measuring parameters of nematode sinusoidal movement. *BMC Genet*, 6:5, 2005.
- S. DasGupta and S. Waddell. Learned odor discrimination in drosophila without combinatorial odor maps in the antennal lobe. *Curr Biol*, 18(21):1668–74, 2008.
- R. E. Davis and A. O. Stretton. Signaling properties of ascaris motoneurons: graded active responses, graded synaptic transmission, and tonic transmitter release. *J Neurosci*, 9(2):415–25, 1989.
- P. Dayan and L. F. Abbott. *Theoretical Neuroscience: Computational and Mathematical Modeling of Neural Systems*. The MIT Press, 2001.
- R. de Boer and P. Kuyper. Triggered correlation. *IEEE Trans Biomed Eng*, 15(3):169–79, 1968.
- G. C. DeAngelis, I. Ohzawa, and R. D. Freeman. Receptive-field dynamics in the central visual pathways. *Trends Neurosci*, 18(10):451–8, 1995.
- J. B. Demb. Functional circuitry of visual adaptation in the retina. *J. Physiol. (Lond.)*, 586:4377–4384, 2008.
- D. A. Dombeck, C. D. Harvey, L. Tian, L. L. Looger, and D. W. Tank. Functional imaging of hippocampal place cells at cellular resolution during virtual navigation. *Nat Neurosci*, 13(11):1433–40, 2010.
- J. F. Etchberger, A. Lorch, M. C. Sleumer, R. Zapf, S. J. Jones, M.A. Marra, R.A. Holt, D. G. Moerman, and O. Hobert. The molecular signature and cis-regulatory architecture of a *C. elegans* gustatory neuron. *Genes Dev.*, 21:1653–1674, 2007.
- S. Faumont, T. H. Lindsay, and S. R. Lockery. Neuronal microcircuits for decision making in *C. elegans*. *Curr Opin Neurobiol*, 22(4):580–91, 2012.
- A. S. French, P. H. Torkkeli, and J. Schuckel. Dynamic characterization of drosophila antennal olfactory neurons indicates multiple opponent signaling pathways in odor discrimination. *J Neurosci*, 31(3):861–9, 2011.

- M. N. Geffen, B. M. Broome, G. Laurent, and M. Meister. Neural encoding of rapidly fluctuating odors. *Neuron*, 61(4):570–86, 2009.
- S. L. Geffeney, J. G. Cueva, D. A. Glauser, J. C. Doll, T. H.-C. Lee, M. Montoya, S. Karania, A. M. Garakani, B. L. Pruitt, and M. B. Goodman. Deg/enac but not trp channels are the major mechanoelectrical transduction channels in a *C. elegans* nociceptor. *Neuron*, 71(5):845–857, 2011.
- Z. Ghahramani and G. E. Hinton. Parameter estimation for linear dynamical systems. Technical Report CRG-TR-96-2, University of Toronto, February 22, 1996 1996.
- Z. Ghahramani and S. T. Roweis. Learning nonlinear dynamical systems using an em algorithm. *Advances in neural information processing systems*, pages 431–437, 1999.
- M. Girolami. Bayesian inference for differential equations. *Theoretical Computer Science*, 408(1):4–16, 2008.
- J. W. Golden and D. L. Riddle. A pheromone influences larval development in the nematode *Caenorhabditis elegans*. *Science*, 218(4572):578–80, 1982.
- G. H. Golub and C. F. Van Loan. *Matrix computations*. Johns Hopkins studies in the mathematical sciences. Johns Hopkins University Press, Baltimore, 3rd edition, 1996.
- C. Gomez, J. G. Brinon, M. V. Barbado, E. Weruaga, J. Valero, and J. R. Alonso. Heterogeneous targeting of centrifugal inputs to the glomerular layer of the main olfactory bulb. *Journal of Chemical Neuroanatomy*, 29(4):238–254, 2005.
- M. B. Goodman, D. H. Hall, L. Avery, and S. R. Lockery. Active currents regulate sensitivity and dynamic range in *C. elegans* neurons. *Neuron*, 20(4):763–72, 1998.
- J. M. Gray, J. J. Hill, and C. I. Bargmann. A circuit for navigation in *Caenorhabditis elegans*. *Proc Natl Acad Sci U S A*, 102(9):3184–91, 2005.
- E. M. Hedgecock and R. L. Russell. Normal and mutant thermotaxis in the nematode *Caenorhabditis elegans*. *Proc Natl Acad Sci U S A*, 72(10):4061–5, 1975.
- M. Hendricks, H. Ha, N. Maffey, and Y. Zhang. Compartmentalized calcium dynamics in a *C. elegans* interneuron encode head movement. *Nature*, 487(7405):99–103, 2012.
- M. A. Hilliard, C. I. Bargmann, and P. Bazzicalupo. *C. elegans* responds to chemical repellents by integrating sensory inputs from the head and the tail. *Curr Biol*, 12(9):730–4, 2002.
- M. A. Hilliard, A. J. Apicella, R. Kerr, H. Suzuki, P. Bazzicalupo, and W. R. Schafer. In vivo imaging of *C. elegans* ash neurons: cellular response and adaptation to chemical repellents. *EMBO J*, 24(1):63–72, 2005.
- J. Hodgkin and T. Doniach. Natural variation and copulatory plug formation in *Caenorhabditis elegans*. *Genetics*, 146(1):149–164, 1997.

- L. Horoszok, V. Raymond, D. B. Sattelle, and A. J. Wolstenholme. Glc-3: a novel fipronil and bidn-sensitive, but picrotoxinin-insensitive, l-glutamate-gated chloride channel subunit from *Caenorhabditis elegans*. *Br. J. Pharmacol.*, 132:1247–1254, 2001.
- I. W. Hunter and M. J. Korenberg. The identification of nonlinear biological systems: Wiener and hammerstein cascade models. *Biol Cybern*, 55(2-3):135–44, 1986.
- R. Ignell, C. M. Root, R. T. Birse, J. W. Wang, D. R. Nassel, and O. M. E. Winther. Presynaptic peptidergic modulation of olfactory receptor neurons in drosophila. *Proceedings of the National Academy of Sciences*, 106(31):13070–13075, 2009.
- Y. Iino and K. Yoshida. Parallel use of two behavioral mechanisms for chemotaxis in *Caenorhabditis elegans*. *J Neurosci*, 29(17):5370–80, 2009.
- R. Ivell and A. Einspanier. Relaxin peptides are new global players. *Trends Endocrinol. Metab.*, 13:343–348, 2002.
- E. J. Izquierdo and S. R. Lockery. Evolution and analysis of minimal neural circuits for klinotaxis in *Caenorhabditis elegans*. *J Neurosci*, 30(39):12908–17, 2010.
- G. Jansen, K. L. Thijssen, P. Werner, M. van der Horst, E. Hazendonk, and R. H. Plasterk. The complete family of genes encoding g proteins of *Caenorhabditis elegans*. *Nat Genet*, 21(4):414–9, 1999.
- K. O. Johnson and S. S. Hsiao. Neural mechanisms of tactual form and texture perception. *Annu Rev Neurosci*, 15:227–50, 1992.
- U. B. Kaupp. Olfactory signalling in vertebrates and insects: differences and commonalities. *Nat Rev Neurosci*, 11(3):188–200, 2010.
- J. A. Kaye, N. C. Rose, B. Goldsworthy, A. Goga, and N. D. L'Etoile. A 3' utr pumilio-binding element directs translational activation in olfactory sensory neurons. *Neuron*, 61:57–70, 2009.
- A. J. Kim, A. A. Lazar, and Y. B. Slutskiy. System identification of drosophila olfactory sensory neurons. *J Comput Neurosci*, 30(1):143–61, 2011.
- K. S. Kindt, K. B. Quast, A. C. Giles, S. De, D. Hendrey, I. Nicastro, C. H. Rankin, and W. R. Schafer. Dopamine mediates context-dependent modulation of sensory plasticity in *C. elegans*. *Neuron*, 55(4):662–676, 2007.
- E. Kodama, A. Kuhara, A. Mohri-Shiomi, K. D. Kimura, M. Okumura, M. Tomioka, Y. Iino, and I. Mori. Insulin-like signaling and the neural circuit for integrative behavior in *C. elegans*. *Genes and Development*, 20(21):2955–2960, 2006.
- M. J. Korenberg. Parallel cascade identification and kernel estimation for nonlinear systems. *Ann Biomed Eng*, 19(4):429–55, 1991.
- J. R. Koza. *Genetic Programming: On the Programming of Computers by Means of Natural Selection*. MIT Press, Cambridge, MA, 1992.

- J. Larsch. personal communication, 2013.
- S. Y. Lau, E. Procko, and R. Gaudet. Distinct properties of  $\text{Ca}^{2+}$ -calmodulin binding to n- and c-terminal regulatory regions of the trpv1 channel. *J Gen Physiol*, 140(5):541–55, 2012.
- S. Laughlin. A simple coding procedure enhances a neuron’s information capacity. *Z Naturforsch C*, 36(9-10):910–2, 1981.
- R. Y. Lee, E. R. Sawin, M. Chalfie, H. R. Horvitz, and L. Avery. Eat-4, a homolog of a mammalian sodium-dependent inorganic phosphate cotransporter, is necessary for glutamatergic neurotransmission in *Caenorhabditis elegans*. *J Neurosci*, 19(1):159–67, 1999.
- Y. W. Lee and M. Schetzen. Measurement of the wiener kernels of a non-linear system by cross-correlation. *Int J Control*, 2(3):237–254, 1965.
- N. D. L’Etoile and C. I. Bargmann. Olfaction and odor discrimination are mediated by the *C. elegans* guanylyl cyclase odr-1. *Neuron*, 25(3):575–86, 2000.
- N. D. L’Etoile, C. M. Coburn, J. Eastham, A. Kistler, G. Gallegos, and C. I. Bargmann. The cyclic gmp-dependent protein kinase egl-4 regulates olfactory adaptation in *C. elegans*. *Neuron*, 36(6):1079–1089, 2002.
- B. J. Liebeskind, D. M. Hillis, and H. H. Zakon. Evolution of sodium channels predates the origin of nervous systems in animals. *Proc Natl Acad Sci U S A*, 108(22):9154–9, 2011.
- Q. Liu, G. Hollopeter, and E. M. Jorgensen. Graded synaptic transmission at the *Caenorhabditis elegans* neuromuscular junction. *Proc Natl Acad Sci U S A*, 106(26):10823–8, 2009.
- S. R. Lockery and M. B. Goodman. The quest for action potentials in *C. elegans* neurons hits a plateau. *Nat. Neurosci.*, 12:377–378, 2009.
- L. Luo, C. V. Gabel, H. I. Ha, Y. Zhang, and A. D. Samuel. Olfactory behavior of swimming *C. elegans* analyzed by measuring motile responses to temporal variations of odorants. *J Neurophysiol*, 99(5):2617–25, 2008.
- E. Marder and D. Bucher. Understanding circuit dynamics using the stomatogastric nervous system of lobsters and crabs. *Annu. Rev. Physiol.*, 69:291–316, 2007.
- V. Z. Marmarelis. *Nonlinear Dynamic Modeling of Physiological Systems*. John Wiley and Sons, Inc., 2004.
- M. Matsuki, H. Kunitomo, and Y. Iino. Gqalpha regulates olfactory adaptation by antagonizing gqalpha -dag signaling in *Caenorhabditis elegans*. *Proc. Natl. Acad. Sci. USA*, 103:1112–1117, 2006.
- J. E. Mellem, P. J. Brockie, Y. Zheng, D. M. Madsen, and A. V. Maricq. Decoding of polymodal sensory stimuli by postsynaptic glutamate receptors in *C. elegans*. *Neuron*, 36(5):933–44, 2002.

- S. M. Mody, M. K. Ho, S. A. Joshi, and Y. H. Wong. Incorporation of galpha (z)-specific sequence at the carboxyl terminus increases the promiscuity of galpha (16) toward g(i)-coupled receptors. *Mol. Pharmacol.*, 57:13–23, 2000.
- K. I. Nagel and A. J. Doupe. Temporal processing and adaptation in the songbird auditory forebrain. *Neuron*, 51(6):845–59, 2006.
- K. I. Nagel and A. J. Doupe. Organizing principles of spectro-temporal encoding in the avian primary auditory area field l. *Neuron*, 58(6):938–55, 2008.
- K. I. Nagel and R. I. Wilson. Biophysical mechanisms underlying olfactory receptor neuron dynamics. *Nat Neurosci*, 14(2):208–16, 2011.
- D. R. Nassel and U. Homberg. Neuropeptides in interneurons of the insect brain. *Cell Tissue Res.*, 326:1–24, 2006.
- A. N. Nathoo, R. A. Moeller, B. A. Westlund, and A. C. Hart. Identification of neuropeptide-like protein gene families in *Caenorhabditis elegans* and other species. *Proc. Natl. Acad. Sci. USA*, 98:14000–14005, 2001.
- A. Palmitessa, H. A. Hess, I. A. Bany, Y.-M. Kim, M. R. Koelle, and J. L. Benovic. *Caenorhabditis elegans* arrestin regulates neural g protein signaling and olfactory adaptation and recovery. *Journal of Biological Chemistry*, 280(26):24649–24662, 2005.
- S. B. Pierce, M. Costa, R. Wisotzkey, S. Devadhar, S. A. Homburger, A. R. Buchman, K. C. Ferguson, J. Heller, D. M. Platt, A. A. Pasquinelli, L. X. Liu, S. K. Doberstein, and G. Ruvkun. Regulation of daf-2 receptor signaling by human insulin and ins-1, a member of the unusually large and diverse *C. elegans* insulin gene family. *Genes and Development*, 15(6):672–686, 2001.
- J. T. Pierce-Shimomura, T. M. Morse, and S. R. Lockery. The fundamental role of pirouettes in *Caenorhabditis elegans* chemotaxis. *J Neurosci*, 19(21):9557–69, 1999.
- D. Ramot, B. L. MacInnis, and M. B. Goodman. Bidirectional temperature-sensing by a single thermosensory neuron in *C. elegans*. *Nat Neurosci*, 11(8):908–15, 2008.
- J. A. Riffell, L. Abrell, and J. G. Hildebrand. Physical processes and real-time chemical measurement of the insect olfactory environment. *J Chem Ecol*, 34(7):837–53, 2008.
- K. Roayaie, J. G. Crump, A. Sagasti, and C. I. Bargmann. The g alpha protein odr-3 mediates olfactory and nociceptive function and controls cilium morphogenesis in *C. elegans* olfactory neurons. *Neuron*, 20(1):55–67, 1998.
- R. C. Robinson. *An introduction to dynamical systems : continuous and discrete*. Pearson Prentice Hall, Upper Saddle River, N.J., 2004.
- M. Schmidt and H. Lipson. Distilling free-form natural laws from experimental data. *Science*, 324(5923):81–5, 2009.

- J. E. Segall, S. M. Block, and H. C. Berg. Temporal comparisons in bacterial chemotaxis. *Proc Natl Acad Sci U S A*, 83(23):8987–91, 1986.
- D. Sieburth, J. M. Madison, and J. M. Kaplan. Pkc-1 regulates secretion of neuropeptides. *Nat. Neurosci.*, 10:49–57, 2007.
- M. Smear, R. Shusterman, R. O’Connor, T. Bozza, and D. Rinberg. Perception of sniff phase in mouse olfaction. *Nature*, 479(7373):397–400, 2011.
- R. Sperry. Neurology and the mind-brain problem. *American Scientist*, 40:291–312, 1962.
- J. Srinivasan, S. H. von Reuss, N. Bose, A. Zaslaver, P. Mahanti, M. C. Ho, O. G. O’Doherty, A. S. Edison, P. W. Sternberg, and F. C. Schroeder. A modular library of small molecule signals regulates social behaviors in *Caenorhabditis elegans*. *PLoS Biol*, 10(1):e1001237, 2012.
- C. Stein, J. D. Clark, U. Oh, M. R. Vasko, G. L. Wilcox, A. C. Overland, T. W. Vanderah, and R. H. Spencer. Peripheral mechanisms of pain and analgesia. *Brain Research Reviews*, 60(1):90–113, 2009.
- W. Stein, N. D. DeLong, D. E. Wood, and M. P. Nusbaum. Divergent co-transmitter actions underlie motor pattern activation by a modulatory projection neuron. *Eur. J. Neurosci.*, 26:1148–1165, 2007.
- G. J. Stephens, M. Bueno de Mesquita, W. S. Ryu, and W. Bialek. Emergence of long timescales and stereotyped behaviors in *Caenorhabditis elegans*. *Proc Natl Acad Sci U S A*, 108(18):7286–9, 2011.
- T. Stiernagle. Maintenance of *C. elegans*. *WormBook*, pages 1–11, 2006.
- C. Y. Su, C. Martelli, T. Emonet, and J. R. Carlson. Temporal coding of odor mixtures in an olfactory receptor neuron. *Proc Natl Acad Sci U S A*, 108(12):5075–80, 2011.
- J. E. Sulston, E. Schierenberg, J. G. White, and J. N. Thomson. The embryonic cell lineage of the nematode *Caenorhabditis elegans*. *Developmental Biology*, 100(1):64–119, 1983.
- H. Suzuki, R. Kerr, L. Bianchi, C. Fr̃žkj̃r-Jensen, D. Slone, J. Xue, B. Gerstbrein, M. Driscoll, and W. R. Schafer. In vivo imaging of *C. elegans* mechanosensory neurons demonstrates a specific role for the mec-4 channel in the process of gentle touch sensation. *Neuron*, 39(6):1005–1017, 2003.
- H. Suzuki, T. R. Thiele, S. Faumont, M. Ezcurra, S. R. Lockery, and W. R. Schafer. Functional asymmetry in *Caenorhabditis elegans* taste neurons and its computational role in chemotaxis. *Nature*, 454(7200):114–7, 2008.
- Y. N. Tallini, M. Ohkura, B.-R. Choi, G. Ji, K. Imoto, R. Doran, J. Lee, P. Plan, J. R. Wilson, H.-B. Xin, A. Sanbe, J. Gulick, J. Mathai, J. Robbins, G. Salama, J. Nakai, and M. I. Kotlikoff. Imaging cellular signals in the heart in vivo: Cardiac expression of the high-signal ca<sup>2+</sup> indicator gcamp2. *Proceedings of the National Academy of Sciences of the United States of America*, 103(12):4753–4758, 2006.

- L. Tian, S. A. Hires, T. Mao, D. Huber, M. E. Chiappe, S. H. Chalasani, L. Petreanu, J. Akerboom, S. A. McKinney, E. R. Schreiter, C. I. Bargmann, V. Jayaraman, K. Svoboda, and L. L. Looger. Imaging neural activity in worms, flies and mice with improved gcamp calcium indicators. *Nat Methods*, 2009.
- M. Tomioka, T. Adachi, H. Suzuki, H. Kunitomo, W. R. Schafer, and Yu. Iino. The insulin/pi 3-kinase pathway regulates salt chemotaxis learning in *Caenorhabditis elegans*. *Neuron*, 51(5):613–625, 2006.
- M. Tsunozaki, S. H. Chalasani, and C. I. Bargmann. A behavioral switch: cgmp and pkc signaling in olfactory neurons reverses odor preference in *C. elegans*. *Neuron*, 59:959–971, 2008.
- P. Van Overshee and B. De Moor. *Subspace Identification for Linear Systems*. Kluwer Academic Publishers, Boston, 1996.
- L. R. Varshney, B. L. Chen, E. Paniagua, D. H. Hall, and D. B. Chklovskii. Structural properties of the *Caenorhabditis elegans* neuronal network. *PLoS Comput Biol*, 7(2):e1001066, 2011.
- N. J. Vickers, T. A. Christensen, T. C. Baker, and J. G. Hildebrand. Odour-plume dynamics influence the brain’s olfactory code. *Nature*, 410(6827):466–70, 2001.
- M. Wachowiak, D. W. Wesson, N. Pirez, J. V. Verhagen, and R. M. Carey. Low-level mechanisms for processing odor information in the behaving animal. *Ann. NY Acad. Sci.*, 1170:286–292, 2009.
- L. E. Waggoner, G. T. Zhou, R. W. Schafer, and W. R. Schafer. Control of alternative behavioral states by serotonin in *Caenorhabditis elegans*. *Neuron*, 21(1):203–14, 1998.
- S. Ward, N. Thomson, J. G. White, and S. Brenner. Electron microscopical reconstruction of the anterior sensory anatomy of the nematode *Caenorhabditis elegans*. *J Comp Neurol*, 160(3):313–37, 1975.
- Q. Wen, M. D. Po, E. Hulme, S. Chen, X. Liu, S. W. Kwok, M. Gershow, A. M. Leifer, V. Butler, C. Fang-Yen, T. Kawano, W. R. Schafer, G. Whitesides, M. Wyart, D. B. Chklovskii, M. Zhen, and A. D. Samuel. Proprioceptive coupling within motor neurons drives *C. elegans* forward locomotion. *Neuron*, 76(4):750–61, 2012.
- A. S. Wenick and O. Hobert. Genomic cis-regulatory architecture and trans-acting regulators of a single interneuron-specific gene battery in *C. elegans*. *Dev. Cell*, 6:757–770, 2004.
- P. D. Wes and C. I. Bargmann. *C. elegans* odour discrimination requires asymmetric diversity in olfactory neurons. *Nature*, 410(6829):698–701, 2001.
- D. T. Westwick and R. E. Kearney. *Identification of nonlinear physiological systems*. IEEE Press [u.a.], Piscataway, NJ [u.a.], 2003.

- J. G. White, E. Southgate, J. N. Thomson, and S. Brenner. The structure of the nervous system of the nematode *Caenorhabditis elegans*. *Philos Trans R Soc Lond B Biol Sci*, 314 (1165):1–340, 1986.
- K. Yamada, T. Hirotsu, M. Matsuki, H. Kunitomo, and Y. Iino. Gpc-1, a g protein gamma-subunit, regulates olfactory adaptation in *Caenorhabditis elegans*. *Genetics*, 181:1347–1357, 2009.
- T.-M. Yi, Y. Huang, M. I. Simon, and J. Doyle. Robust perfect adaptation in bacterial chemotaxis through integral feedback control. *Proceedings of the National Academy of Sciences*, 97(9):4649–4653, 2000.
- M. Zimmer, J. M. Gray, N. Pokala, A. J. Chang, D. S. Karow, M. A. Marletta, M. L. Hudson, D. B. Morton, N. Chronis, and C. I. Bargmann. Neurons detect increases and decreases in oxygen levels using distinct guanylate cyclases. *Neuron*, 61(6):865–79, 2009.

# Appendix: L-N Estimation Flowchart

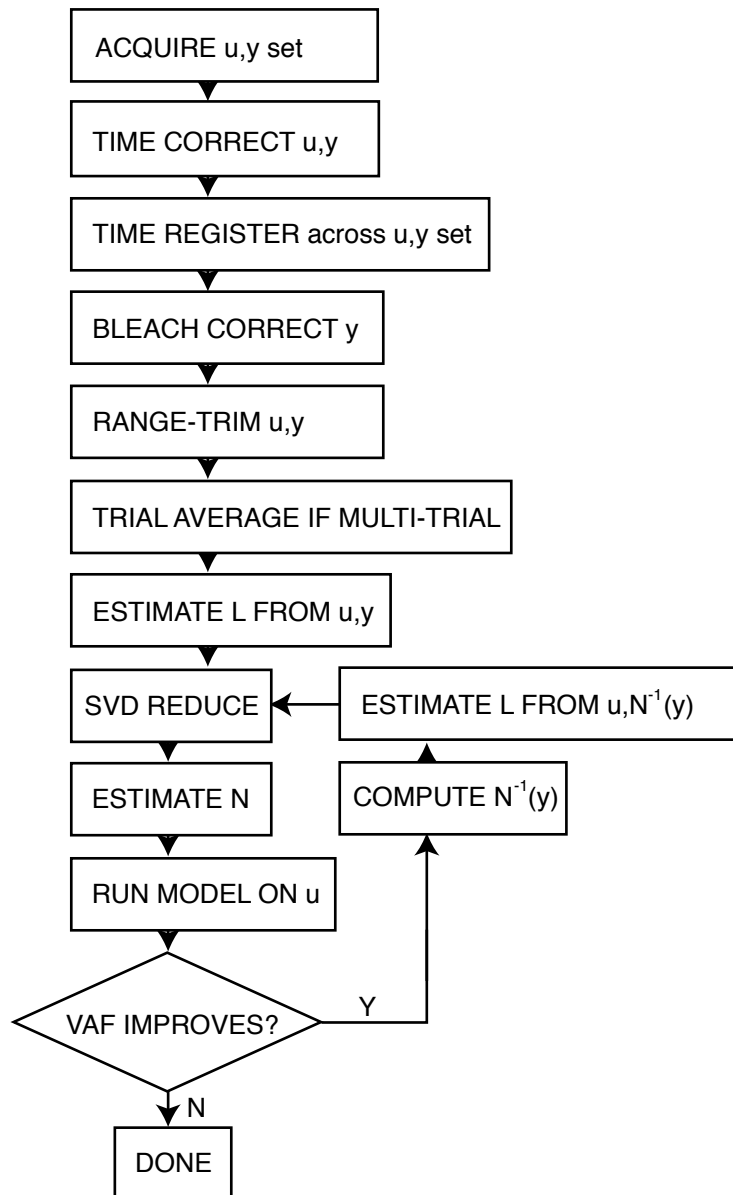


Figure 4.2: Flowchart for iterative L-N estimation